NASA Technical Memorandum 81912

Low-Speed Aerodynamic Characteristics of a 14-Percent-Thick NASA Phase 2 Supercritical Airfoil Designed for a Lift Coefficient of 0.7

Charles D. Harris, Robert J. McGhee,
and Dennis O. Allison
Langley Research Center
Hampton, Virginia

NASA
National Aeronautics
and Space Administration

Scientific and Technical
Information Branch

1980

SUMMARY

Airfoil characteristics varied systematically over the range of test conditions and behaved in a conventionally accepted manner. The maximum measured lift coefficient was about 2.2 and occurred near $M = 0.15$ at a Reynolds number of 12.0×10^6. The variation of lift with angle of attack at the lower Mach numbers and at all Reynolds numbers exhibited behavior generally associated with gradual trailing-edge separation in the prestall angle-of-attack range, but the stall itself was more abrupt than would be expected of classical trailing-edge stall. The stall became more gradual at the higher Mach numbers. Drag remained essentially constant over a lift range which extended from near zero to beyond the design lift coefficient of 0.7 for a constant Reynolds number with fixed transition.

INTRODUCTION

Continued development of supercritical airfoil technology has resulted in the design of family-related phase 2 supercritical airfoils. Two such airfoils, 10- and 14-percent-thick, designed for a lift coefficient of 0.7 have been tested at transonic speeds in the Langley 8-Foot Transonic Pressure Tunnel, and the results were reported in references 1 and 2.

The 14-percent-thick airfoil has also been tested at low speeds in the Langley Low-Turbulence Pressure Tunnel, and the results are presented herein. Included are the effects of varying Reynolds number from 2.0×10^6 to 18.0×10^6 at a Mach number of 0.15 and the effects of varying Mach number from 0.10 to 0.32 at a Reynolds number of 6.0×10^6.

SYMBOLS

Values are given in the International System of Units (SI) and in U.S. Customary Units. Measurements and calculations were made in U.S. Customary Units.

C_p	pressure coefficient, $\frac{p - p_\infty}{q_\infty}$
$C_{p,sonic}$	pressure coefficient corresponding to local Mach number of 1.0
c	chord of airfoil, cm (in.)
c_c	section chord-force coefficient, $\oint C_p \, d\left(\frac{z}{c}\right)$
c_d	section drag coefficient determined from wake measurements, $\int_{\text{wake}} c_d' \, d\left(\frac{h}{c}\right)$

c_d'	point drag coefficient (ref. 3)
c_l	section lift coefficient, $c_n(\cos\alpha) - c_c(\sin\alpha)$
c_m	section pitching-moment coefficient about quarter-chord point, $-\oint C_p\left(\frac{x}{c} - 0.25\right) d\left(\frac{x}{c}\right) + \oint C_p \frac{z}{c} d\left(\frac{z}{c}\right)$
c_n	section normal-force coefficient, $-\oint C_p\, d\left(\frac{x}{c}\right)$
h	vertical distance in wake profile, cm (in.)
$\frac{l}{d}$	section lift-drag ratio, $\frac{c_l}{c_d}$
M	free-stream Mach number
p	static pressure, Pa (lbf/ft^2)
q	dynamic pressure, Pa (lbf/ft^2)
R	Reynolds number based on free-stream conditions and airfoil chord
t	airfoil thickness, cm (in.)
x	abscissa measured along airfoil reference line from airfoil leading edge, cm (in.)
y	spanwise distance from centerline of tunnel, cm (in.)
z	ordinate measured normal to airfoil reference line, cm (in.)
z_c	ordinate of airfoil mean line, cm (in.)
α	angle of attack, deg

Subscripts:

l	lower surface
max	maximum
min	minimum
u	upper surface
∞	free-stream conditions

Airfoil designations:

SC(1)-0714	supercritical (phase 1) -0.7 design lift coefficient. 14-percent-thick
SC(2)-0714	supercritical (phase 2) -0.7 design lift coefficient, 14-percent-thick

AIRFOIL DEVELOPMENT

A concerted effort within the National Aeronautics and Space Administration (NASA) over the past several years has been directed toward developing practical two-dimensional airfoils with good transonic behavior while retaining acceptable low-speed characteristics and has focused on a concept referred to as the supercritical airfoil.

An early phase of this effort was successful in significantly extending drag-rise characteristics beyond those of conventional airfoils. (See ref. 4.) These early supercritical airfoils (denoted by supercritical (phase 1) prefix), however, experienced a gradual increase of drag (drag creep) at Mach numbers just preceding the final drag rise. This gradual buildup of drag was largely associated with an intermediate off-design second velocity peak (an acceleration of the flow over the rear portion of the airfoil just before the final recompression at the trailing edge) and relatively weak shock waves above the upper surface at these speeds. (See, for example, ref. 5.)

Improvements to these early, phase 1 airfoils resulted in airfoils with significantly reduced drag creep characteristics. (See, for example, refs. 6 and 7.) These early phase 1 airfoils and the improved phase 1 airfoils of references 6 and 7 were developed before adequate theoretical analysis codes were available and resulted from iterative contour modifications during wind-tunnel experiments. The process consisted of evaluating experimental pressure distributions at design and off-design conditions and physically altering the airfoil profiles to yield the best drag characteristics over a range of test conditions.

During the experimental development of these phase 1 airfoils, design criteria were recognized which provided guidelines for the design of supercritical airfoils and are briefly discussed in references 1 and 2. Based on these criteria, two phase 2 (denoted by supercritical (phase 2) prefix) supercritical airfoils were designed: the 10-percent-thick airfoil reported in reference 1 and the 14-percent-thick airfoil reported in reference 2. The design lift coefficient was 0.7 for both airfoils. An iterative design process was used which consisted of altering the airfoil coordinates until the recently developed, viscous, airfoil analysis program of reference 8 indicated that the design criteria had been satisfied.

APPARATUS AND PROCEDURES

Model

Geometric characteristics of the SC(2)-0714 model are presented in figure 1, and section coordinates are presented in table I.

The model was constructed with a metal core around which plastic fill and two thin layers of fiberglass were used to form the contour of the airfoil. Orifice holes of 0.10-cm (0.040-in.) diameter were drilled perpendicular to the model surface into embedded pressure tubes. The model had a chord of 61 cm (24 in.) and a span of 91 cm (36 in.). The airfoil surface was sanded in the chordwise direction with number 400, dry silicon-carbide paper to provide an aerodynamically smooth finish. The model contour accuracy was generally within ±0.10 mm (±0.004 in.).

Wind Tunnel

The Langley Low-Turbulence Pressure Tunnel (ref. 9) is a closed-throat, single-return tunnel which can be operated at stagnation pressures from 10.1 to 1010 kPa (0.1 to 10 atm) with tunnel-empty test-section Mach numbers up to 0.42 and 0.22, respectively. The maximum unit Reynolds number is about 49.0×10^6 per meter (15.0×10^6 per foot) at a Mach number of about 0.22. The tunnel test section is 91 cm (3 ft) wide by 229 cm (7.5 ft) high.

Hydraulically actuated circular plates provide positioning and attachment for two-dimensional models. The plates are 102 cm (40 in.) in diameter, rotate with the airfoil, and are flush with the tunnel wall. Rectangular model attachment plates in the circular plates hold the model in such a way that the center of rotation for angle-of-attack adjustment was at 0.25c on the model reference line.

A sketch showing the relationship between the ends of the model, the tunnel walls, the model attachment plates, and the rotating circular plates is shown in figure 2. With this mounting system, the model completely spans the tunnel with each end confined in a recess in the tunnel sidewall. At the sidewalls, inside joint seams between mating pieces were sealed and faired smooth with model plastic and silastic rubber to minimize the effect of air leakage.

Measurements

Surface-pressure measurements.- Static pressures were measured on the surface of the model and used to determine local surface-pressure coefficients. The surface-pressure measurements were obtained from a chordwise row of orifices located approximately 5 cm (2 in.) from the tunnel centerline. Orifices were concentrated near the leading and trailing edges of the airfoil to define the pressure gradients in these regions, and a rearward-facing orifice was included in the trailing edge. In addition, three spanwise rows of orifices, located at 1-, 10-, and 75-percent chordwise stations, were included to establish the two dimensionality of the flow over the model.

Wake measurement.- Drag forces acting on the airfoil, as determined by the momentum deficiency within the wake, were derived from vertical variations of the total and static pressures measured across the wake with the wake survey rake shown in figure 3. The fixed rake, mounted from the tunnel sidewall, was positioned in the vertical centerline plane of the tunnel, one chord-length behind the trailing edge of the model. The total-pressure tubes were 0.15 cm (0.060 in.) in diameter and the static-pressure tubes were 0.32 cm (0.125 in.) in diameter.

The total-pressure tubes were flattened to 0.10 cm (0.040 in.) for 0.61 cm (0.24 in.) from the tip of the tube. The static-pressure tubes each had four flush orifices, drilled 90° apart, located eight tube diameters from the tip of the tube in the measurement plane of the total-pressure tubes.

Instrumentation

Measurements of the static pressures on the airfoil surfaces and the wake pressures were made by an automatic pressure-scanning system utilizing variable-capacitance-type precision transducers. Basic tunnel pressures were measured with precision quartz manometers. Angle of attack was measured with a calibrated digital shaft encoder operated by a pinion gear and rack attached to the circular model attachment plates. Data were obtained by a high-speed acquisition system and recorded on magnetic tape.

Reduction of Data and Corrections

Calculation of c_c, c_n, and c_m.- Section chord-force, normal-force, and pitching-moment coefficients were obtained by numerical integration (based on the trapezoidal method) of the local surface-pressure coefficient measured at each orifice multiplied by an appropriate weighting factor (incremental area).

Calculation of c_d.- To obtain section drag coefficients, point drag coefficients were computed for each total-pressure measurement in the wake by using the procedure of reference 3. These point drag coefficients were then summed by numerical integration across the wake, again based on the trapezoidal method.

Corrections for wind-tunnel-wall effects.- In the linear portion of the lift curve, corrections for lift effects and solid and wake blockage based on references 10 and 11 are small, on the order of 2-percent or less, and are usually neglected. As the model approaches maximum lift conditions where the lift characteristics become nonlinear and the viscous effects become significant, the assumptions underlying the corrections based on references 10 and 11 begin to break down and become inadequate. For these reasons, the data presented herein is uncorrected for tunnel-wall effects. Figure 4 is presented, however, to indicate the effect corrections would have on the aerodynamic characteristics if they were applied.

TEST CONDITIONS

Tests were conducted over a range of Reynolds numbers based on the model chord from about 2.0×10^6 to 18.0×10^6 at a Mach number of 0.15. Mach number was also varied from about 0.10 to 0.32 at a Reynolds number of 6.0×10^6. The airfoil was tested smooth (natural transition) and with transition trips fixed along the 5-percent chordline on the upper and lower surfaces. The transition trips consisted of sparsely distributed 0.13-cm-wide (0.05-in.) bands of carborundum grains, sized according to the technique in reference 12 and attached to the surface with clear lacquer.

PRESENTATION OF RESULTS

The results of this investigation are arranged in the following figures:

DISCUSSION

Two Dimensionality of Flow

The spanwise pressure distributions shown in figure 5 indicate that the flow over the model remained two dimensional to angles of attack at which maximum lift coefficients occurred. For example, the flow at $R = 2.0 \times 10^6$ and $\alpha = 16^\circ$ (shown in fig. 11 to be near maximum lift conditions) is indicated in figure 5(a) to be two dimensional in character even though a considerable region of separation over the rear upper surface is shown in the tuft photographs of figure 6. Correlation of the angles of attack for maximum lift for the other test Reynolds numbers (fig. 11) with the corresponding spanwise pressure distributions in figure 5 indicate similar results.

In addition to the flow over the airfoil remaining two dimensional to angles of attack beyond maximum lift, the tuft photographs for $R = 2.0 \times 10^6$ (fig. 6) show that the flow on the tunnel sidewall above the model remains attached until an angle of attack of 17°, which is also beyond maximum lift.

Experimental Results

In brief, airfoil characteristics varied systematically over the range of test conditions and behaved in a conventionally accepted manner. The largest measured value of $c_{l,max}$ was about 2.2 and occurred near $M = 0.15$ at a Reynolds number of 12.0×10^6. (See figs. 15 and 18.) The variation of lift with angle of attack, at the lower Mach numbers and all Reynolds numbers, exhibited behavior generally associated with gradual trailing-edge separation in the prestall angle-of-attack range, but the stall itself was more abrupt than would be expected of classical trailing-edge stall. (See figs. 11 and 18.) The stall became more gradual at the higher Mach numbers. Drag remained essentially constant over a lift range which extended from near zero to beyond the design lift coefficient of 0.7 (figs. 11(c), 17, and 18) for a constant Reynolds number with fixed transition.

Effects of fixing transition (fig. 7).- Because of the viscous decambering effect of the thicker boundary layer, fixing transition near the leading edge generally resulted in decreased lift, increased drag, and less negative pitching moments. The effects were more pronounced at the lower lift coefficients and Reynolds numbers where the greatest extent of laminar flow would exist for the smooth model. Shown in figure 8(a) are the pressure distributions for $\alpha = -2^\circ$ and $R = 2.0 \times 10^6$, where the greatest effect of fixing transition was observed. The low Reynolds number and the near zero pressure gradients would encourage a long run of laminar flow before natural transition would occur for the smooth model.

These effects generally decreased with increases in either angle of attack or Reynolds number. The reduced effects with increased angle of attack are associated with the steep adverse pressure gradient of the leading-edge suction peak at high angles which causes natural transition to occur near the leading edge on the upper surface. The reduced effects with increased Reynolds number are due to the thinner boundary layers, the tendency for natural transition to occur nearer the leading edge, and the higher wind-tunnel turbulence level which would also induce earlier transition.

The small differences at the higher angles of attack may not be completely explained because of the inability to determine the relative positions of boundary-layer transition between free and fixed transition on the lower surface. This inability to determine lower-surface boundary-layer transition at high angles of attack is due to the favorable pressure gradient over a large portion of the lower surface and to the fact that the lower-surface transition strip was ahead of the stagnation point at high angles and, therefore, may not have properly tripped the lower-surface boundary layer.

The general effect of fixing transition and its trend with increasing Reynolds number reverses at high angles of attack for $R = 18.0 \times 10^6$. Shown in figure 7(f) are increased lift, increased pitching moments, and reduced drag with fixed transition. These results are believed to be associated with the elimination, or reduction in size, of a small laminar-separation bubble on the airfoil upper surface by the introduction of roughness near the stagnation point on the lower surface. Tabulated pressure distributions (not presented) indicate that at $\alpha = 12^\circ$, where the lift curves of figure 7(f) first diverge, the stagnation point has moved to a lower-surface location corresponding to the trip location (0.05c). The presence of a laminar-separation bubble can only be assumed since there are no discernible discontinuities or plateaus in the pressure coefficients plotted against angle of attack for given chordwise stations shown in figures 9 and 10. Such discontinuities are usually indicative of the presence of a bubble of separated flow.

Since natural transition usually occurs near the leading edge of airfoils in actual flight conditions because of the roughness of construction or of insect remains gathered in flight, the remainder of the data discussed in this report (except for the comparison with other airfoils shown in fig. 23) will be with transition fixed at 0.05c on both upper and lower surfaces.

Stall characteristics.- The shape of the lift curve (fig. 11(a)) in the prestall region is associated with a progressive separation or thickening of the turbulent boundary layer in the region of the trailing edge where the lift curve slope begins to decrease at the onset of trailing-edge separation. The appearance of trailing-edge separation is also manifested by a flattening of the pressure distribution at the rear of the airfoil (fig. 12) and by divergence of the pressure coefficients over and near the trailing edge. (See fig. 13)

Although the shape of the lift curve in the prestall region is characteristic of thick airfoils (thickness ratios of approximately 0.12 or greater) which stall as a result of trailing-edge boundary-layer separation, the actual stall is shown in figure 11 as a sudden, sharp loss of lift usually associated with leading-edge separation on airfoils of more moderate thickness.

Generally, airfoils which stall as a result of trailing-edge separation have relatively flat pressure distributions over a large region toward the rear of the airfoil at maximum lift, but the peak suction pressures near the leading edge continue to increase after the stall resulting in a lift curve with rounded maximum. Airfoils which stall as a result of leading-edge stall, however, show a continual increase of the peak pressures near the leading edge up to the angles of attack for maximum lift, followed by an abrupt collapse of the leading-edge pressures.

The pressure distributions of figure 12 show that, at angles of attack for maximum lift conditions, trailing-edge separation extends over about 20-percent of the chord. After stall, however, the upper-surface separation has spread to almost 90-percent of the chord. Except for the lowest Reynolds number of 2.0×10^6 (fig. 12(a)), there is only a partial collapse of the leading-edge peak which indicates that stall was caused by a precipitous forward movement of the trailing-edge separation.

Effects of Reynolds number (fig. 11).- As the Reynolds number increased from the lowest value of 2.0×10^6 to 12.0×10^6 at $M = 0.15$, lift increased, pitching moments became more negative, and drag decreased (minimum drag summarized in fig. 14) due to the thinning of the boundary layer. Because the thinner boundary layer is more resistant to separation, the maximum lift coefficient (fig. 15) increased from 1.84 to 2.23 over this range of Reynolds numbers. As Reynolds number was further increased to 18.0×10^6 the maximum lift coefficient decreased to 2.15. In addition, higher values of drag and less negative pitching moments at high lift coefficients for $R = 18.0 \times 10^6$ compared with $R = 12.0 \times 10^6$ are indicated in figure 11. These reversals in the trend of the variation of the aerodynamic characteristics with Reynolds number are due to a greater amount of trailing-edge separation for $R = 18.0 \times 10^6$ compared to $R = 12.0 \times 10^6$. (See fig. 12.)

Although the experimental data is not detailed enough to explain this phenomenon, it is possible that increasing Reynolds number from 12.0×10^6 to 18.0×10^6 moved the reattachment location of the laminar separation bubble which altered the initial thickness of the reattached turbulent boundary layer in such a manner as to promote increased trailing-edge separation.

Effects of Mach number (fig. 18).- The effects of Mach number on the maximum lift coefficient at a Reynolds number of 6.0×10^6, shown in figure 18, are summarized in figure 19. There is a decrease in the maximum lift coefficient and in the angle of attack for maximum lift with increasing Mach number, which becomes appreciable above $M \approx 0.20$.

In reference 13, the decrease in maximum lift with Mach number is related to the appearance of local supersonic flow near the leading edge. In figure 20, it is shown that supersonic flow was encounted near stall for Mach numbers of 0.28 and 0.32. Although the zone of supersonic flow may be small, the resulting recompression of the flow thickens the boundary layer and increases the tendency for turbulent separation at the rear of the airfoil.

The stall characteristics are much less abrupt at the higher Mach numbers (fig. 18) due to a more gradual forward progression of the trailing-edge separation. (Compare fig. 21 with fig. 12(c).)

Comparison of Maximum Lift Characteristics With Other Airfoils

Maximum lift characteristics of the SC(2)-0714 are compared with those of the NASA low- and medium-speed airfoils (refs. 14 and 15) and NACA airfoils (ref. 16) in figure 23.

This comparison shows the maximum lift coefficients for the SC(2)-0714 airfoil to be about 0.1 greater than for the NASA low-speed airfoils, almost 0.2 greater than for the NASA medium-speed airfoils, and from 0.5 to 0.6 greater than for the NACA airfoils. Because of the greater aft camber, the pitching-moment coefficient of the supercritical airfoil is about -0.13 at zero lift, compared to about -0.10 for the low-speed airfoils, about -0.07 for the medium-speed airfoils, and near zero for the NACA 23015.

Higher maximum lift could, of course, be achieved with conventional airfoils through increased camber. Maximum lift coefficients approaching that of the supercritical airfoil are reported for a NACA 6716 four-digit airfoil in reference 17, for example, but those higher maximum lift coefficients are accompanied by pitching-moment coefficients of approximately -0.20 and separation over the trailing edge at low angles of attack.

CONCLUDING REMARKS

Wind-tunnel tests have been conducted to determine the low-speed two-dimensional aerodynamic characteristics of a 14-percent-thick NASA supercritical airfoil with a design lift coefficient of 0.7. This report documents the experimental results of these tests. Free-stream Mach number ranged from 0.10 to 0.32, and the chord Reynolds number varied from 2.0×10^6 to 18.0×10^6. Analysis of the results indicate the following general conclusions:

1. Maximum lift coefficient increased with Reynolds number from 2.0×10^6 to 12.0×10^6 ($M = 0.15$) and attained a value of about 2.2. A small decrease in maximum lift was observed with further increase in Reynolds number to 18.0×10^6.

2. Maximum lift coefficient decreased with increased Mach number ($R = 6.0 \times 10^6$), the decrease became significant above $M \approx 0.20$.

3. The application of a transition strip near the leading edge resulted in only small effects in maximum lift since natural transition occurred near the upper-surface leading edge due to the adverse pressure gradient associated with the suction peak at high angles of attack.

4. The shape of the prestall lift curve was characteristic of a gradual trailing-edge stall, but the stall itself was abrupt and attributed to a precipitous forward movement of the trailing-edge separation point.

5. Drag remained essentially constant over a lift range which extended from near zero to beyond the design lift coefficient for a constant Reynolds number with transition fixed.

Langley Research Center
National Aeronautics and Space Administration
Hampton, VA 23665
November 26, 1980

REFERENCES

1. Harris, Charles D.: Aerodynamic Characteristics of the 10-Percent-Thick NASA Supercritical Airfoil 33 Designed for a Normal-Force Coefficient of 0.7. NASA TM X-72711, 1975.

2. Harris, Charles D.: Aerodynamic Characteristics of a 14-Percent-Thick NASA Supercritical Airfoil Designed for a Normal-Force Coefficient of 0.7. NASA TM X-72712, 1975.

3. Baals, Donald D.; and Mourhess, Mary J.: Numerical Evaluation of the Wake-Survey Equations for Subsonic Flow Including the Effect of Energy Addition. NACA WR L-5, 1945. (Formerly NACA ARR L5H27.)

4. Whitcomb, Richard T.: Review of NASA Supercritical Airfoils. ICAS Paper No. 74-10, Aug. 1974.

5. Harris, Charles D.: Wind-Tunnel Investigation of Effects of Trailing-Edge Geometry on a NASA Supercritical Airfoil Section. NASA TM X-2336, 1971.

6. Harris, Charles D.: Aerodynamic Characteristics of an Improved 10-Percent-Thick NASA Supercritical Airfoil. NASA TM X-2978, 1974.

7. Harris, Charles D.: Transonic Aerodynamic Characteristics of the 10-Percent-Thick NASA Supercritical Airfoil 31. NASA TM X-3203, 1975.

8. Bauer, Frances; Garabedian, Paul; Korn, David; and Jameson, Antony: Supercritical Wing Sections II. Volume 108 of Lecture Notes in Economics and Mathematical Systems, Springer-Verlag, 1975.

9. Von Doenhoff, Albert E.; and Abbott, Frank T., Jr.: The Langley Two-Dimensional Low-Turbulence Pressure Tunnel. NACA TN 1283, 1947.

10. Pope, Alan; and Harper, John J.: Low-Speed Wind Tunnel Testing. John Wiley & Sons, Inc., 1966.

11. Pankhurst, R. C.; and Holder, D. W.: Wind-Tunnel Technique. Sir Isaac Pitman & Sons, Ltd. (London), 1965.

12. Braslow, Albert L.; and Knox, Eugene C.: Simplified Method for Determination of Critical Height of Distributed Roughness Particles for Boundary-Layer Transition at Mach Numbers From 0 to 5. NACA TN 4363, 1958.

13. Wootton, L. R.: The Effect of Compressibility on the Maximum Lift Coefficient of Aerofoils at Subsonic Airspeeds. J. Roy. Aeronaut. Soc., vol. 71, July 1967, pp. 476-486.

14. McGhee, Robert J.; and Beasley, William D.: Low-Speed Aerodynamic Characteristics of a 17-Percent-Thick Airfoil Section Designed for General Aviation Applications. NASA TN D-7428, 1973.

15. McGhee, Robert J.; Beasley, William D.; and Whitcomb, Richard T.: NASA Low- and Medium-Speed Airfoil Development. NASA TM-78709, 1979.

16. Abbott, Ira H.; and Von Doenhoff, Albert E.: Theory of Wing Sections. Dover Publ., Inc., c.1959.

17. Bingham, Gene J.; and Noonan, Kevin W.: Low-Speed Aerodynamic Characteristics of NACA 6716 and NACA 4416 Airfoils With 35-Percent-Chord Single-Slotted Flaps. NASA TM X-2623, 1974.

TABLE I.- SECTION COORDINATES FOR SC(2)-0714

[c = 61.0 cm (24 in.); leading-edge radius = 0.030c]

x/c	$(z/c)_u$	$(z/c)_l$	x/c	$(z/c)_u$	$(z/c)_l$
0.0000	0.0000	0.0000	0.240	0.0659	-0.0661
.002	.0108	-.0108	.250	.0665	-.0667
.005	.0167	-.0165	.260	.0670	-.0672
.010	.0225	-.0223	.270	.0675	-.0677
.020	.0297	-.0295	.280	.0679	-.0681
.030	.0346	-.0343	.290	.0683	-.0685
.040	.0383	-.0381	.300	.0686	-.0688
.050	.0414	-.0411	.310	.0689	-.0691
.060	.0440	-.0438	.320	.0692	-.0693
.070	.0463	-.0461	.330	.0694	-.0695
.080	.0484	-.0481	.340	.0696	-.0696
.090	.0502	-.0500	.350	.0698	-.0697
.100	.0519	-.0517	.360	.0699	-.0697
.110	.0535	-.0533	.370	.0700	-.0697
.120	.0549	-.0547	.380	.0700	-.0696
.130	.0562	-.0561	.390	.0700	-.0695
.140	.0574	-.0574	.400	.0700	-.0693
.150	.0585	-.0585	.410	.0699	-.0691
.160	.0596	-.0596	.420	.0698	-.0689
.170	.0606	-.0606	.430	.0697	-.0686
.180	.0615	-.0616	.440	.0696	-.0682
.190	.0624	-.0625	.450	.0694	-.0678
.200	.0632	-.0633	.460	.0692	-.0673
.210	.0640	-.0641	.470	.0689	-.0667
.220	.0647	-.0648	.480	.0686	-.0661
.230	.0653	-.0655	.490	.0683	-.0654

ORIGINAL PAGE IS
OF POOR QUALITY

TABLE I.- Concluded

x/c	$(z/c)_u$	$(z/c)_l$	x/c	$(z/c)_u$	$(z/c)_l$
0.500	0.0680	-0.0646	0.760	0.0457	-0.0173
.510	.0676	-.0637	.770	.0442	-.0152
.520	.0672	-.0627	.780	.0426	-.0132
.530	.0668	-.0616	.790	.0409	-.0113
.540	.0663	-.0604	.800	.0392	-.0095
.550	.0658	-.0591	.810	.0374	-.0079
.560	.0652	-.0577	.820	.0356	-.0064
.570	.0646	-.0562	.830	.0337	-.0050
.580	.0640	-.0546	.840	.0317	-.0038
.590	.0634	-.0529	.850	.0297	-.0028
.600	.0627	-.0511	.860	.0276	.0020
.610	.0620	-.0493	.870	.0255	-.0014
.620	.0613	-.0474	.880	.023[illegible]	-.0010
.630	.0605	-.0454	.890	.02[illegible]	-.0008
.640	.0596	-.0434	.900	.0186	-.0008
.650	.0587	-.0413	.910	.0162	-.0011
.660	.0578	-.0392	.920	.0137	-.0016
.670	.0568	-.0371	.930	.0111	-.0024
.680	.0558	-.0349	.940	.0084	-.0035
.690	.0547	-.0327	.950	.0057	-.0049
.700	.0536	-.0305	.960	.0029	-.0066
.710	.0524	-.0283	.970	.0000	-.0086
.720	.0512	-.0261	.980	-.0030	-.0109
.730	.0499	-.0239	.990	-.0062	-.0136
.740	.0486	-.0217	1.000	-.0095	-.0165
.750	.0472	-.0195			

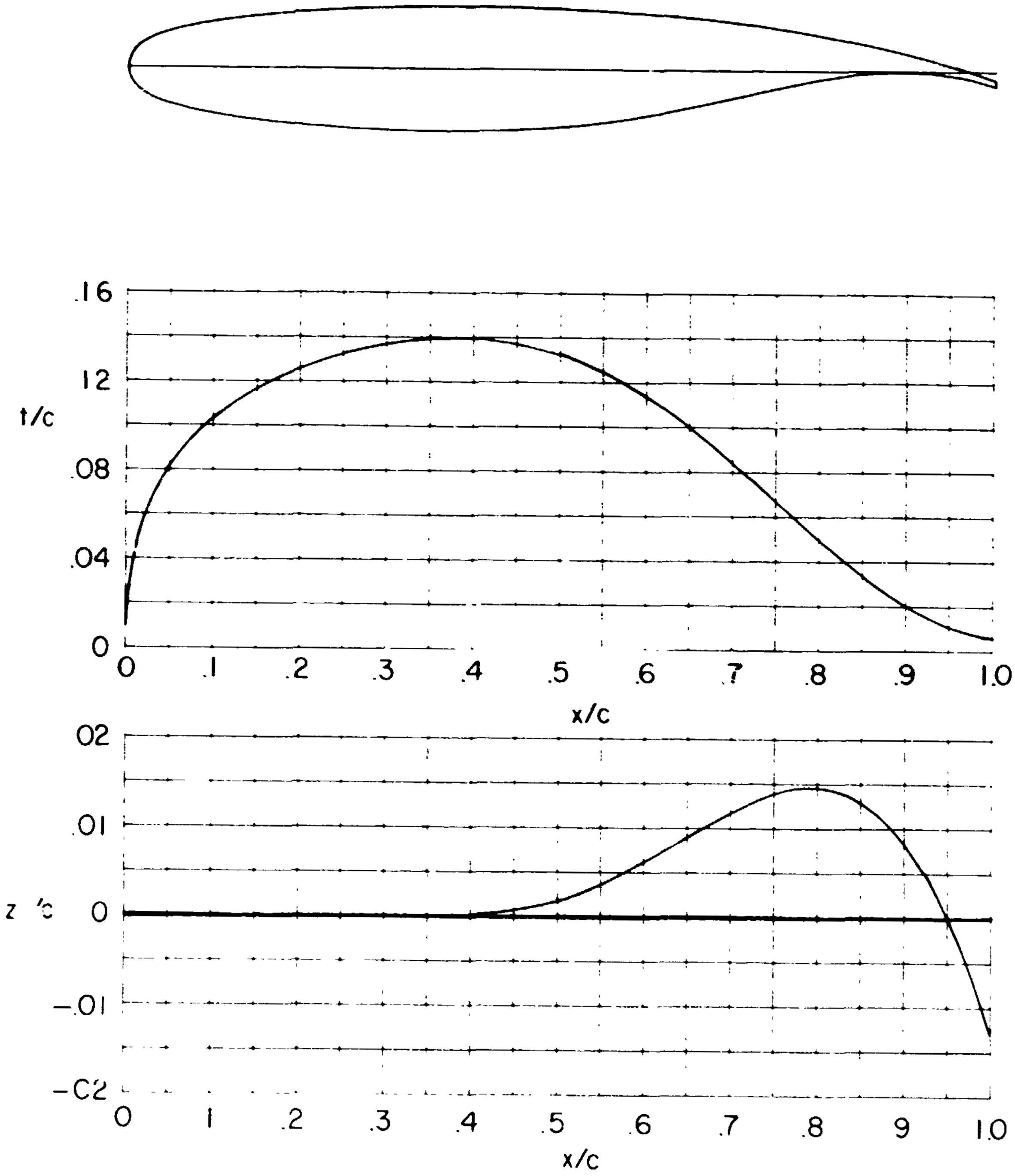

Figure 1.- Profile, thickness distribution, and camber line of 14-percent-thick supercritical airfoil (SC(2)-0714).

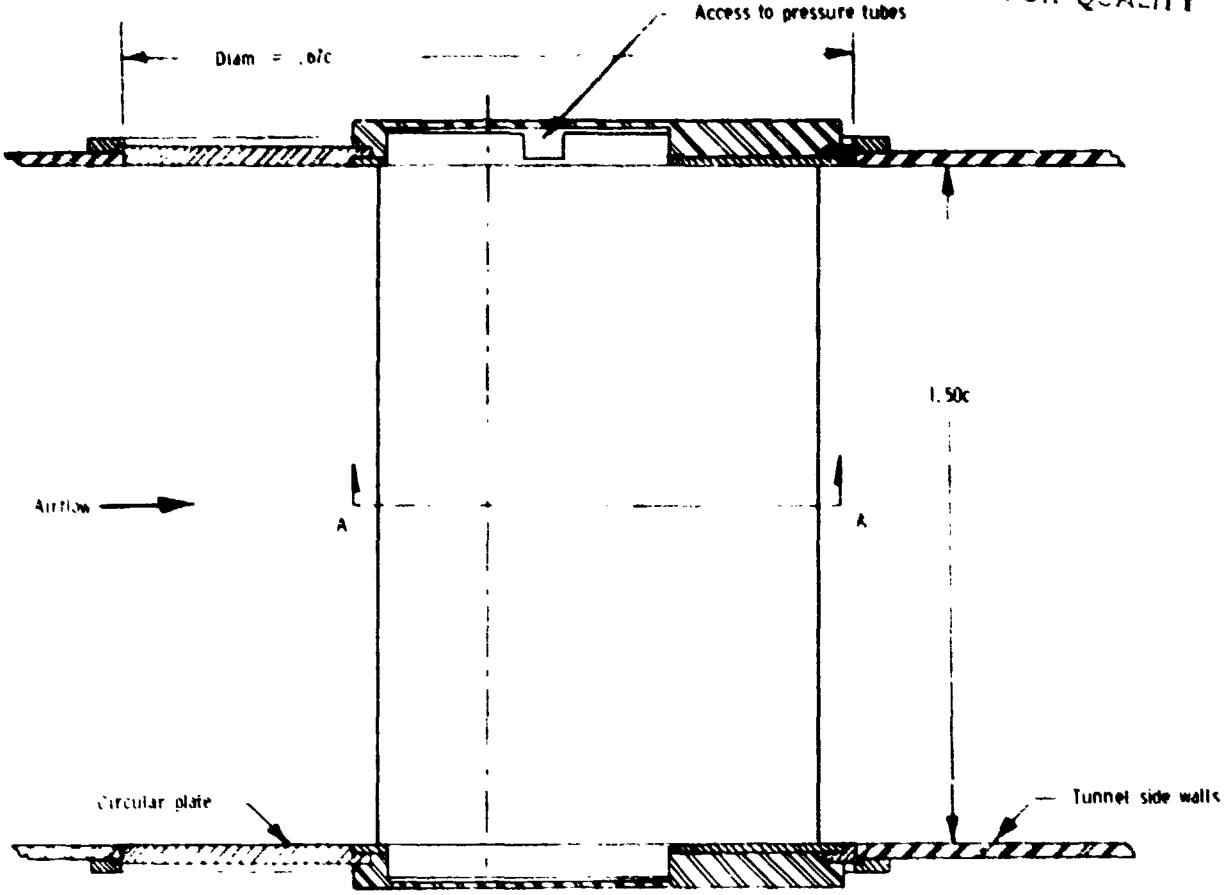

Top view

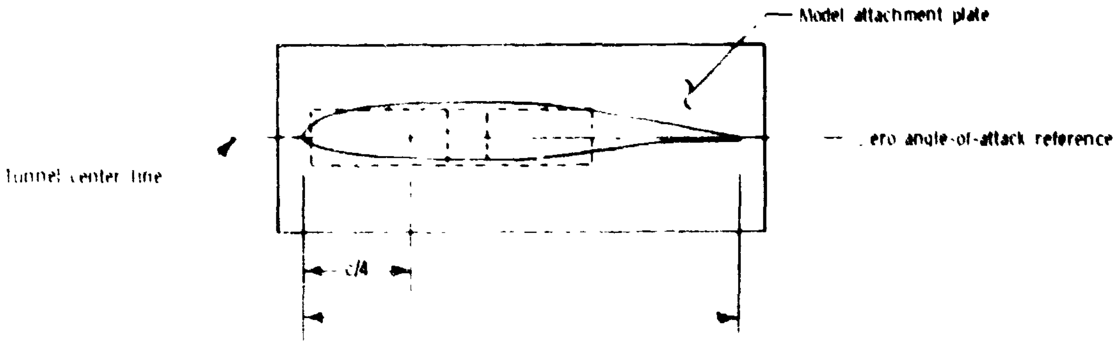

End view section A A

Figure 2.- Typical airfoil mounted in wind tunnel. All dimensions are in terms of airfoil chord; c = 61.0 cm (24.0 in.).

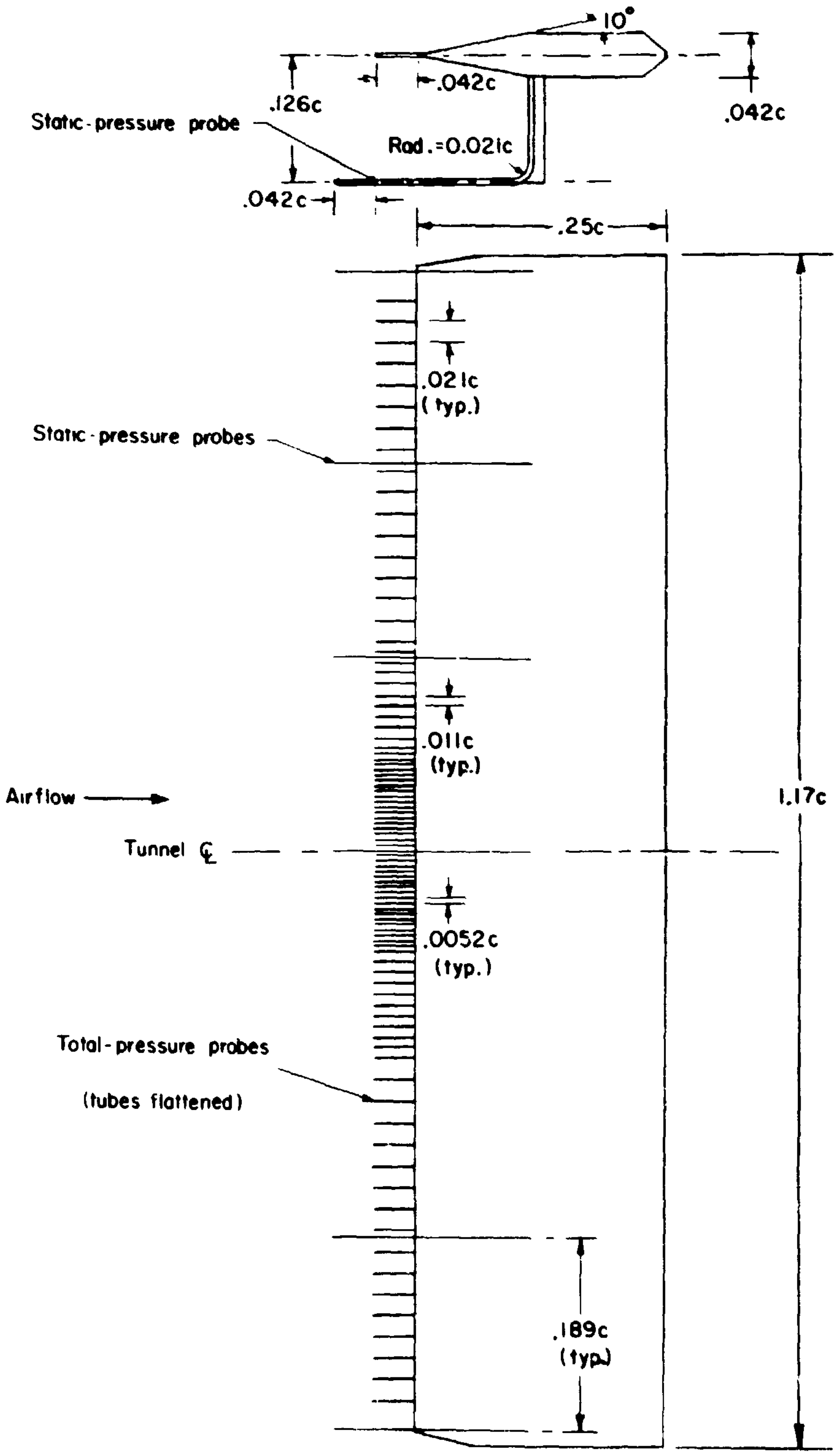

Figure 3.- Wake survey rake. All dimensions in terms of airfoil chord. c = 61.01 cm (24.02 in.).

ORIGINAL PAGE IS
OF POOR QUALITY

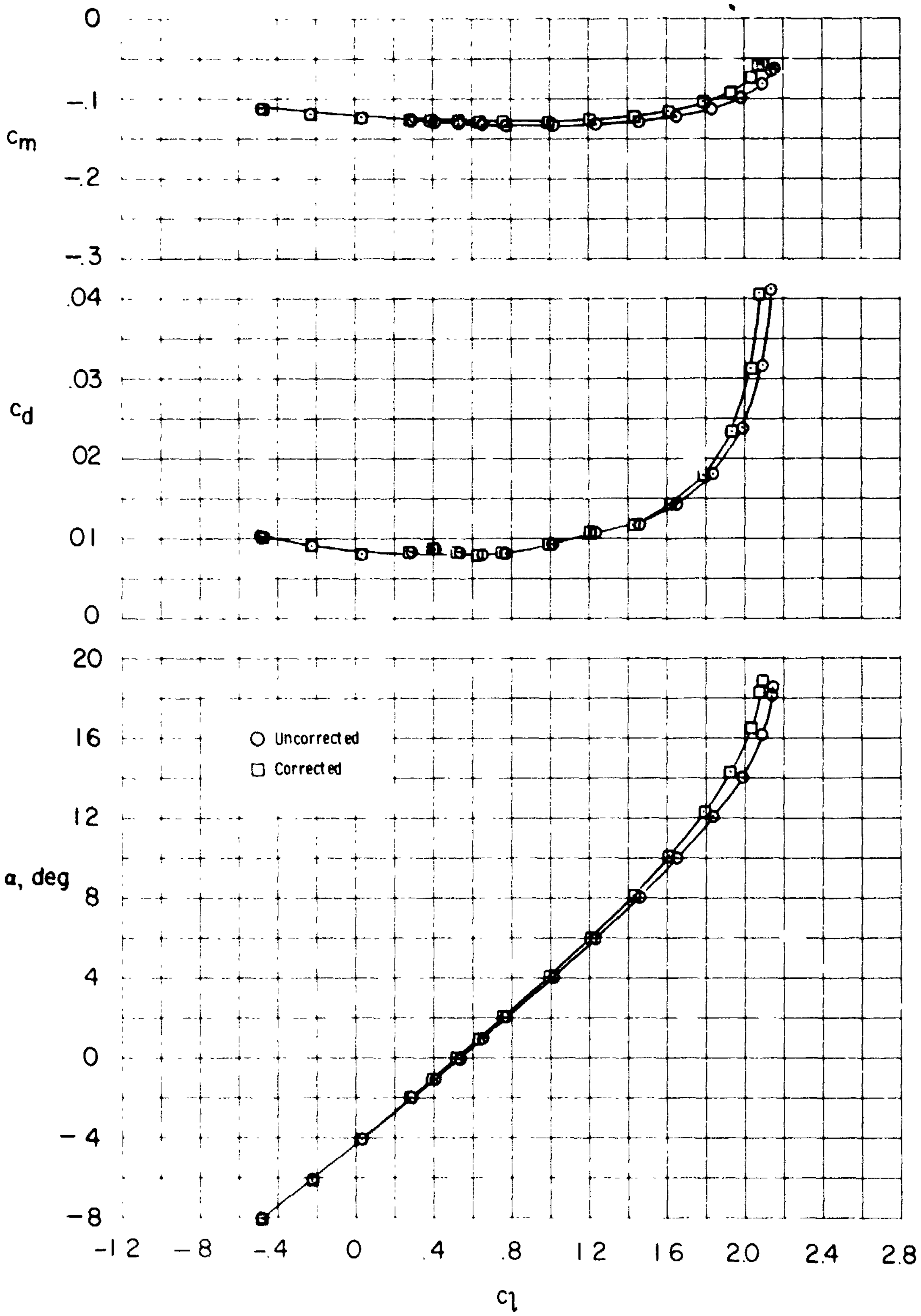

Figure 4.- Comparison of corrected and uncorrected aerodynamic characteristics; $M = 0.15$, $R = 18.0 \times 10^6$, transition fixed.

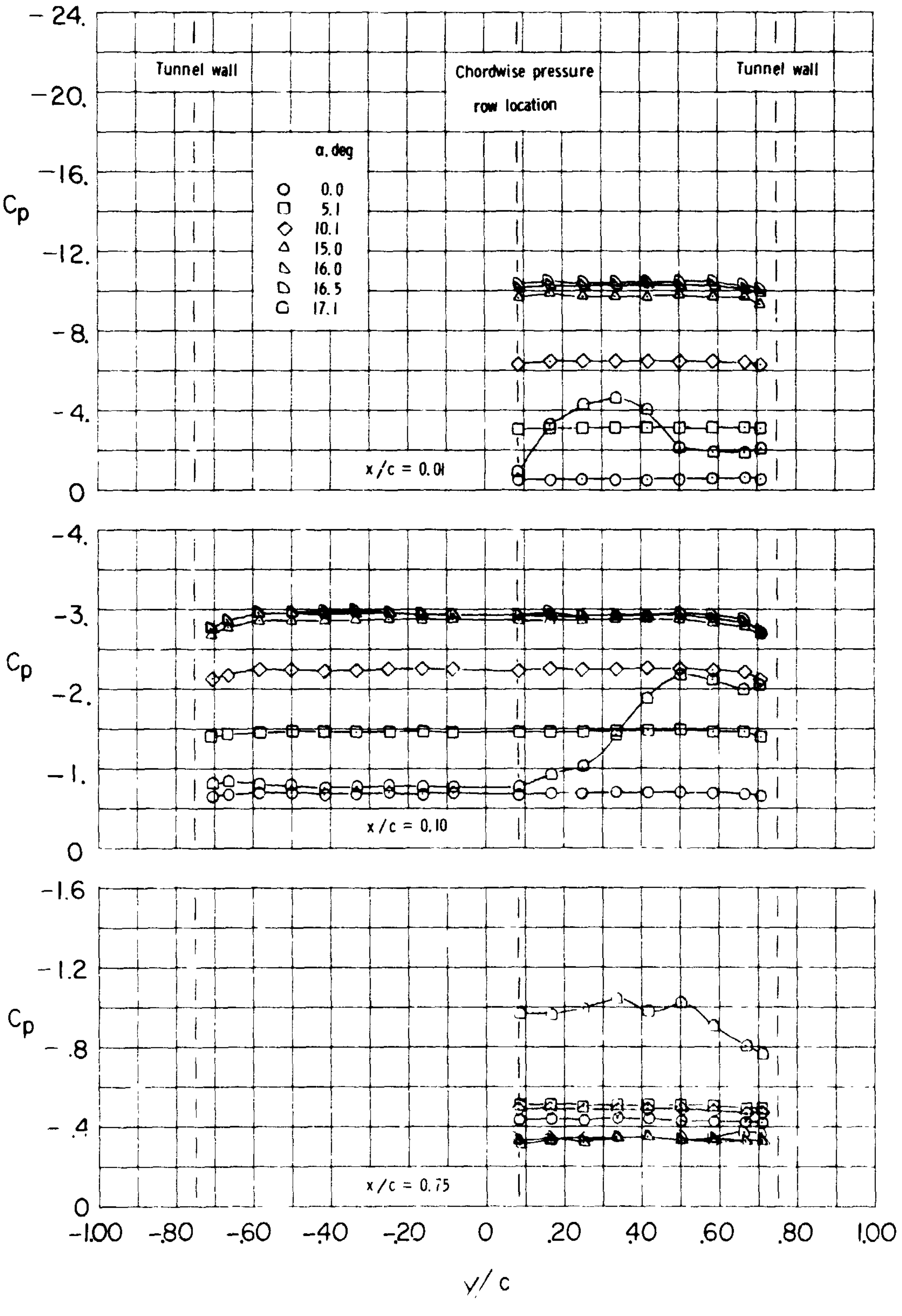

(a) $R = 2.0 \times 10^6$.

Figure 5.- Spanwise pressure distribution on upper surface; M = 0.15, transition fixed.

ORIGINAL PAGE IS
OF POOR QUALITY

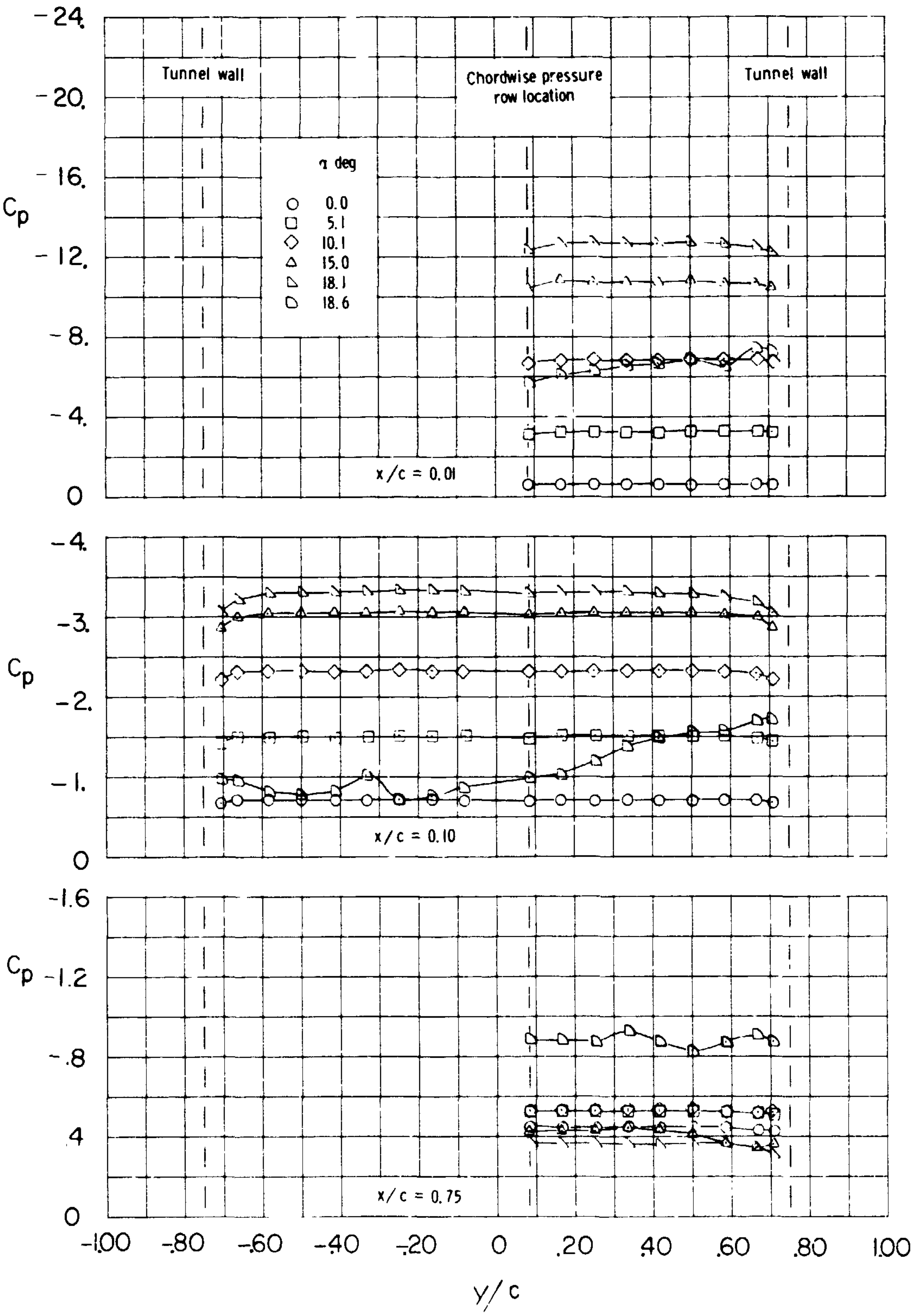

(b) $R = 4.0 \times 10^6$.

Figure 5.- Continued.

ORIGINAL PAGE IS
OF POOR QUALITY

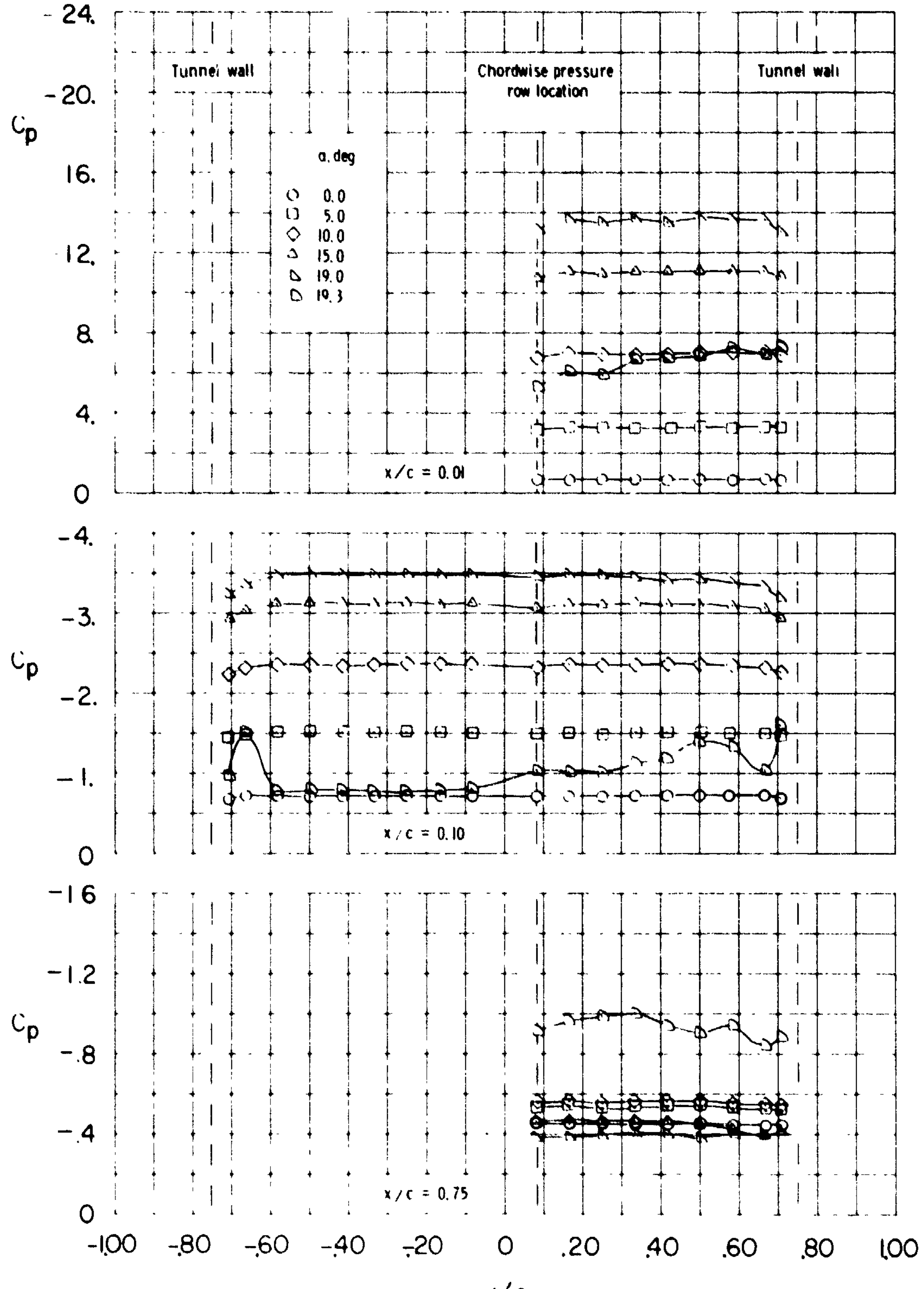

(c) R = 6.0 × 10^6.

Figure 5.- Continued.

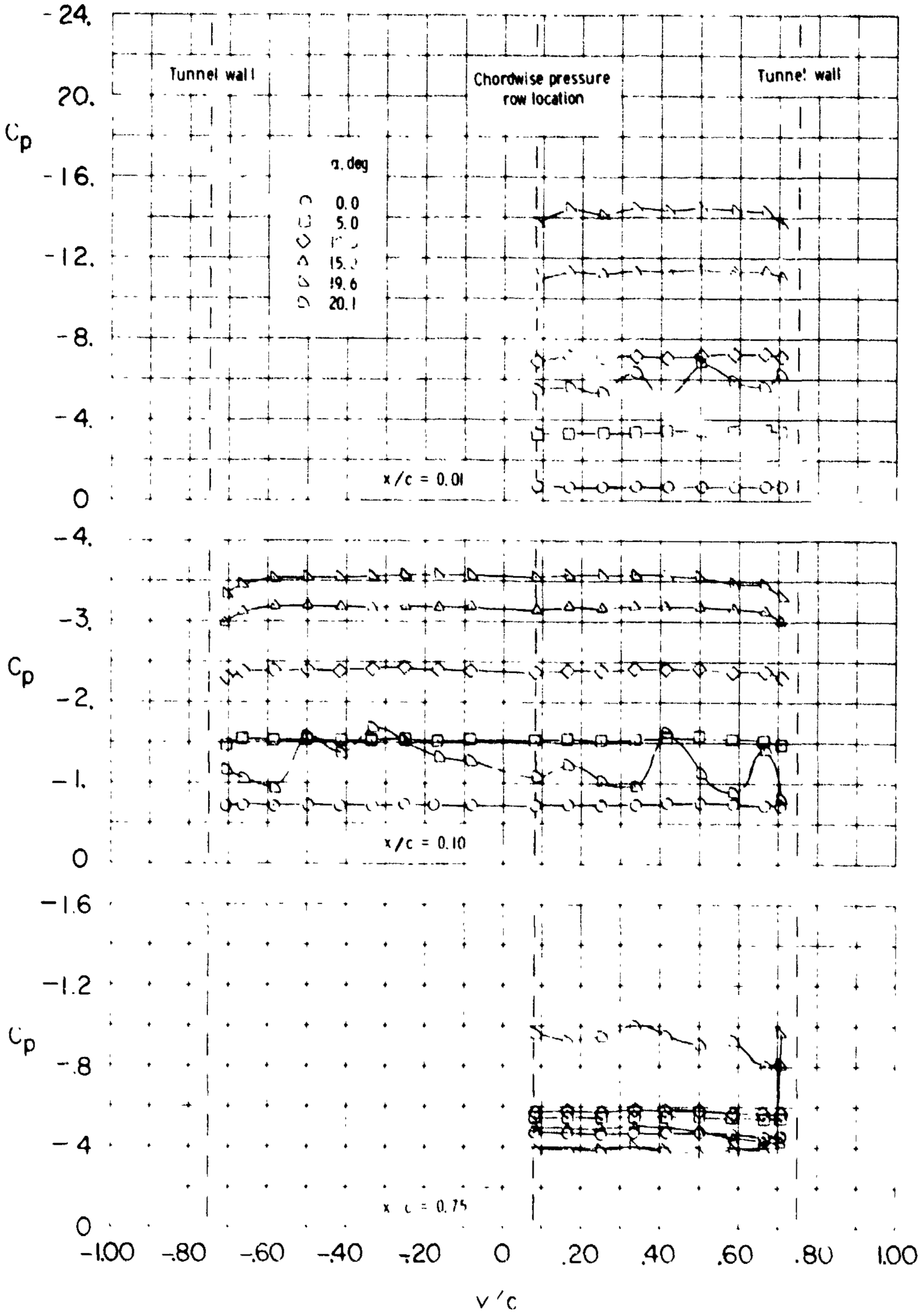

(d) $R = 9.0 \times 10^6$.

Figure 5.- Continued

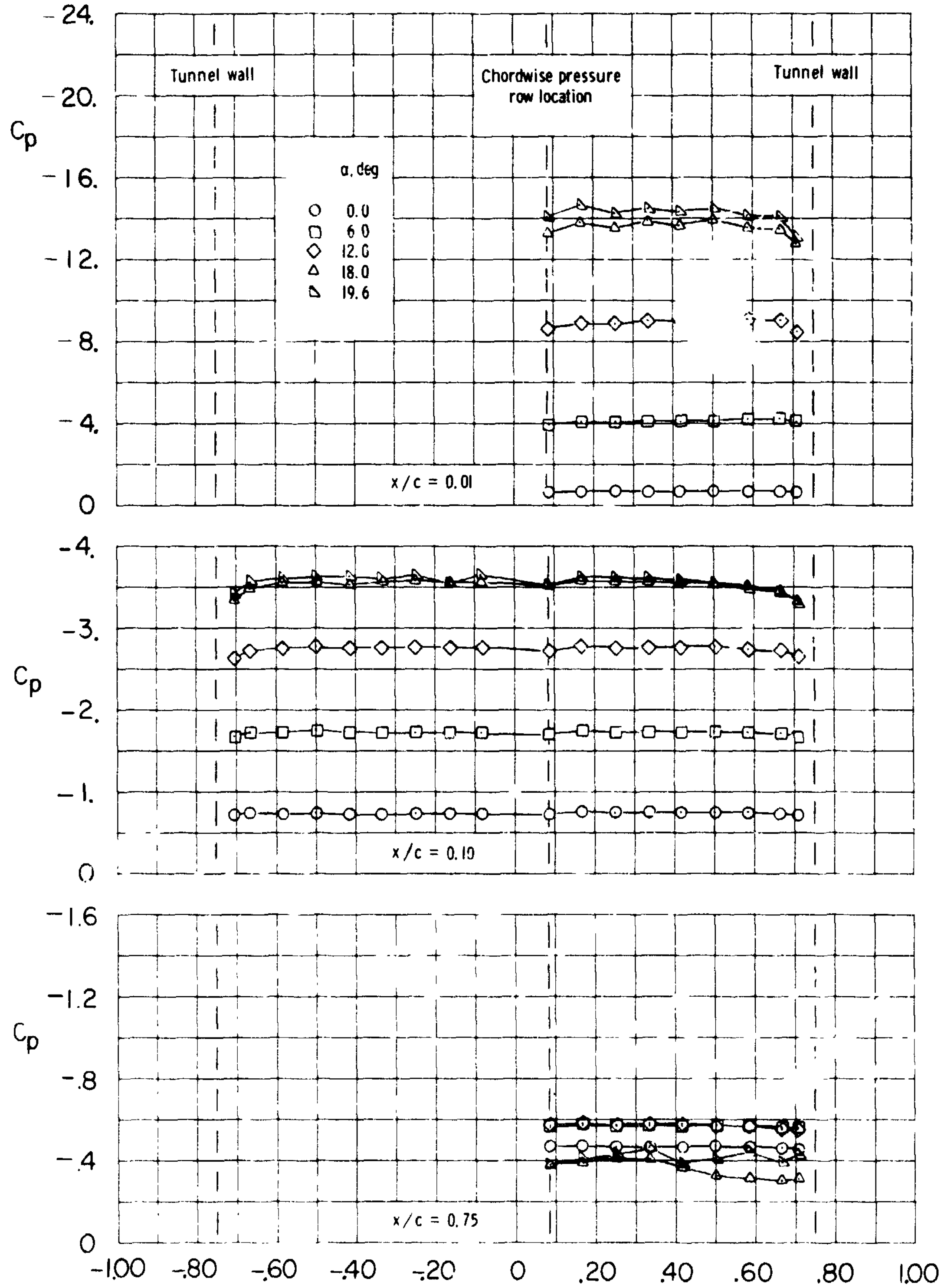

(e) R = 12.0 × 10^6.

Figure 5.- Continued.

ORIGINAL PAGE IS
OF POOR QUALITY

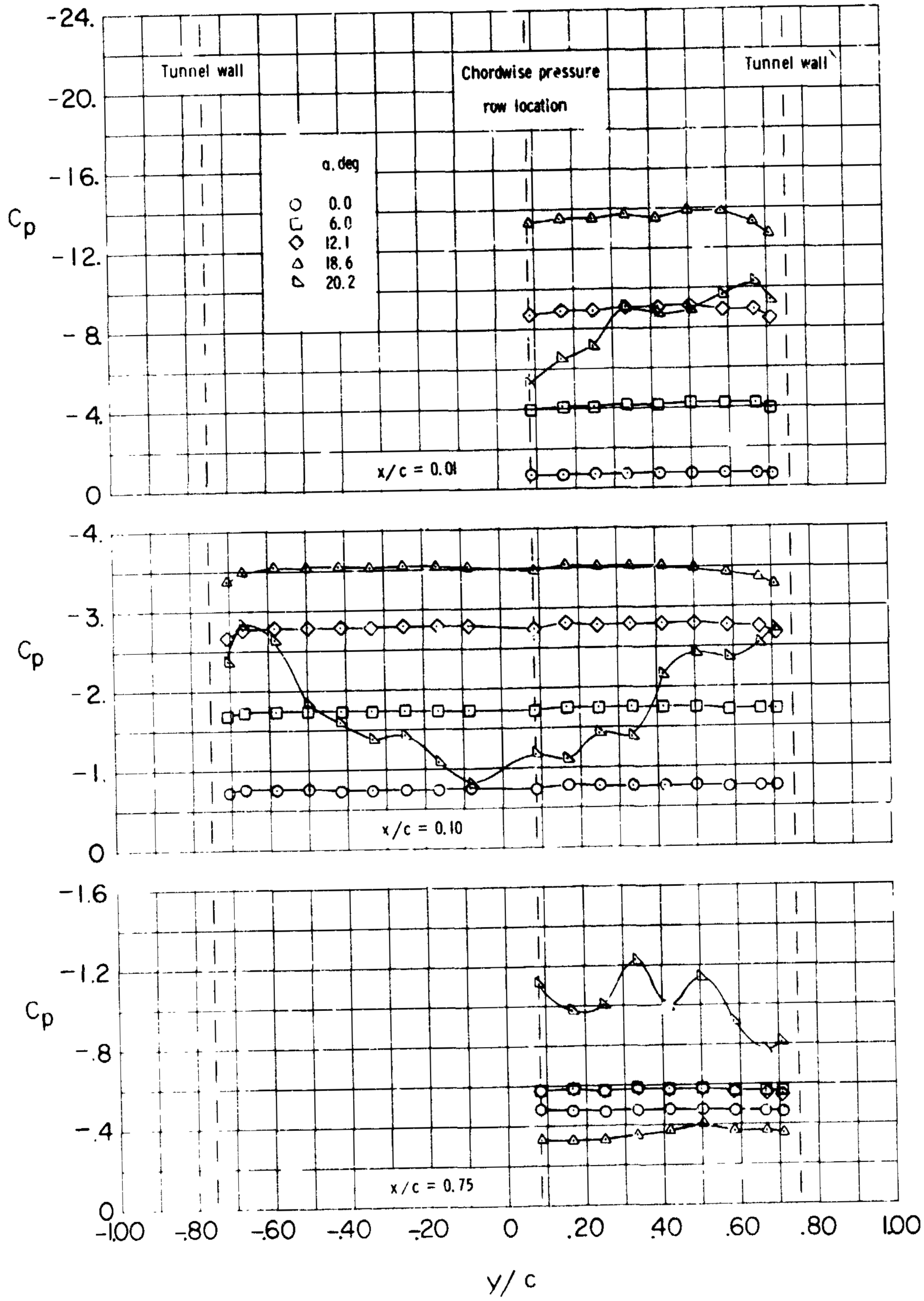

(f) R = 18.0 × 10^6.

Figure 5.- Concluded.

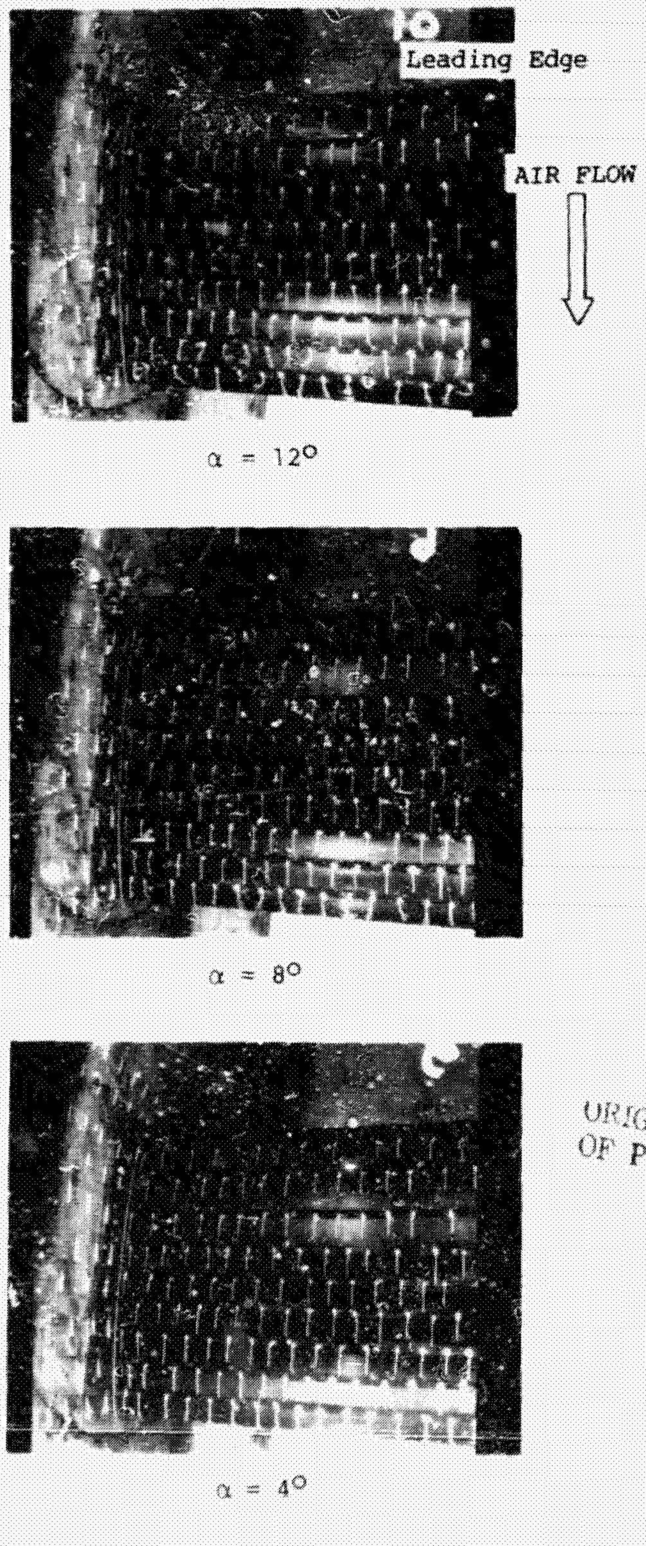

α = 12°

α = 8°

α = 4°

L-80-217

Figure 6.- Tuft photograp angle of attack on upper-surface flow pattern; M = .0 × 10^6, transition fixed.

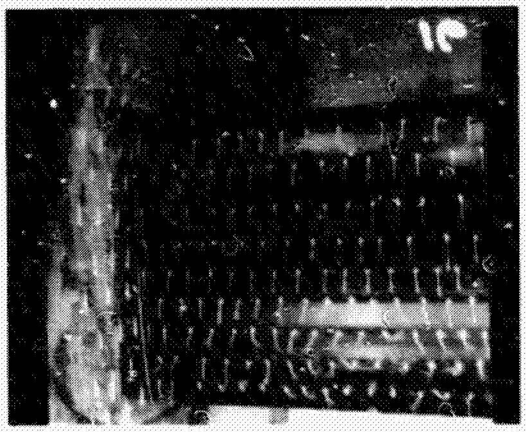

$\alpha = 15^{\circ}$

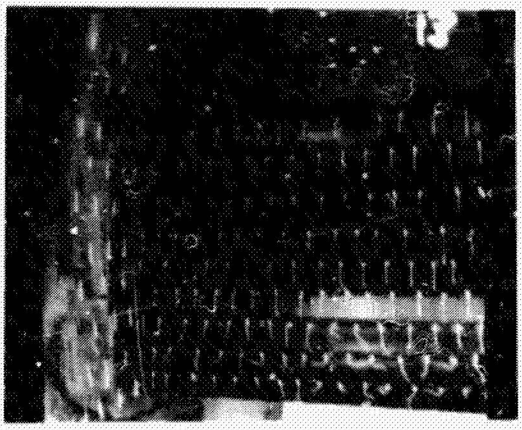

$\alpha = 14^{\circ}$

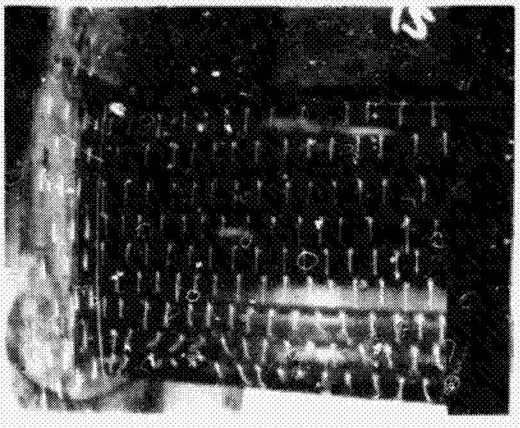

$\alpha = 13^{\circ}$

L-80-218

Figure 6.- Continued.

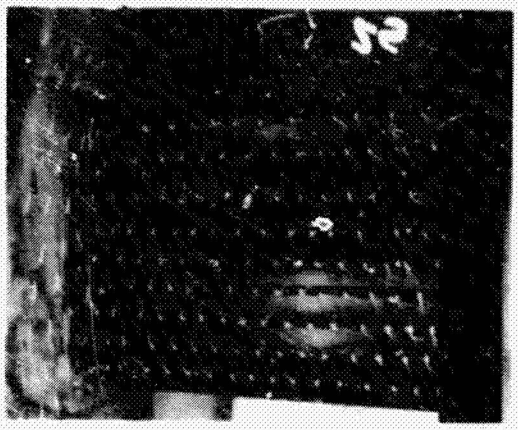

α = 17°

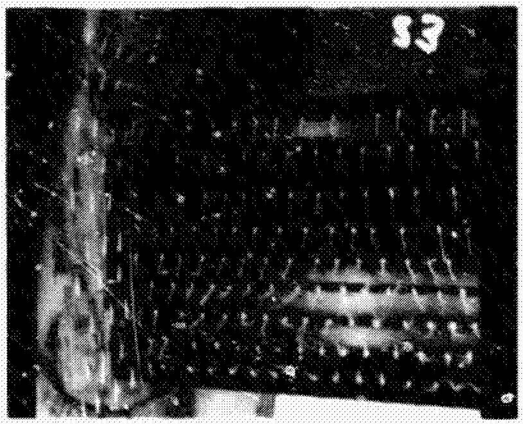

α = 16 1/2°

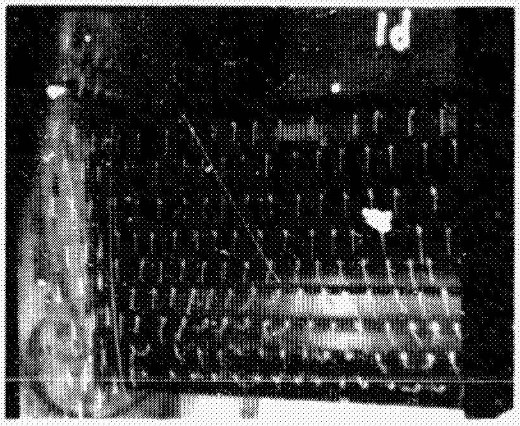

α = 16°

L-80-219

Figure 6.- Concluded.

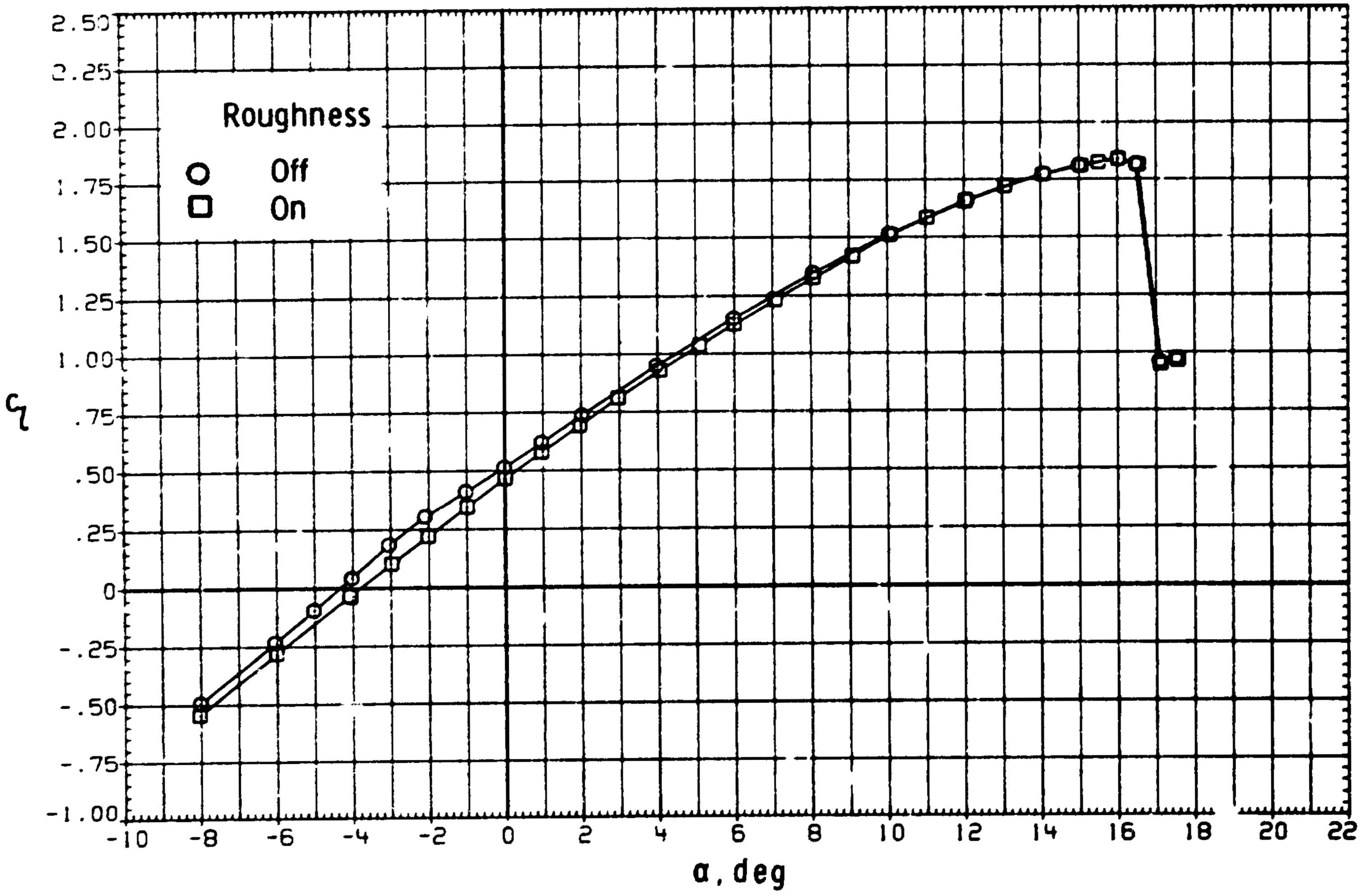

(a) R = 2.0 × 10^6.

Figure 7.- Effect of fixing transition at 5-percent chord; M = 0.15.

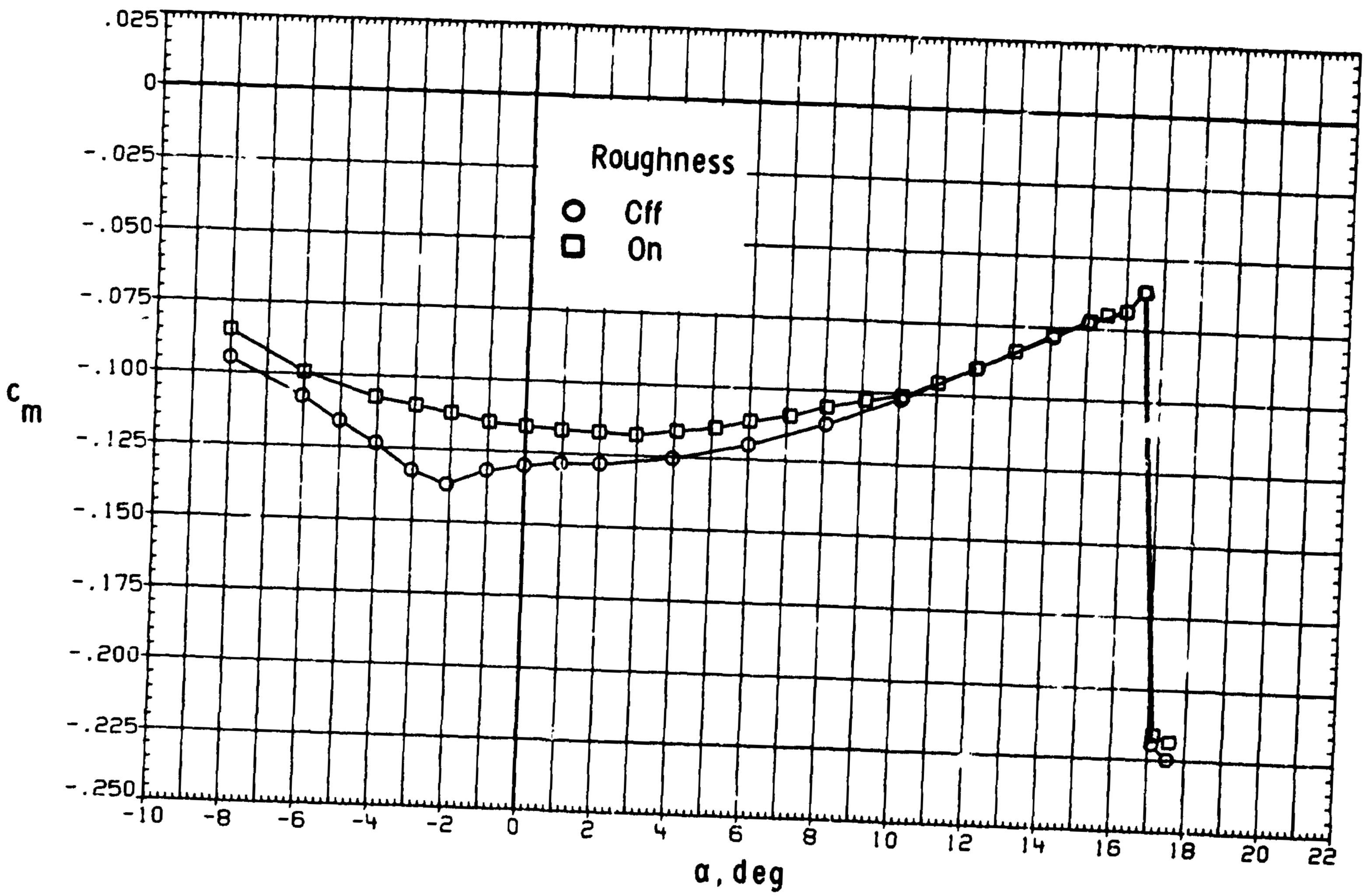

(a) Continued.

Figure 7.- Continued.

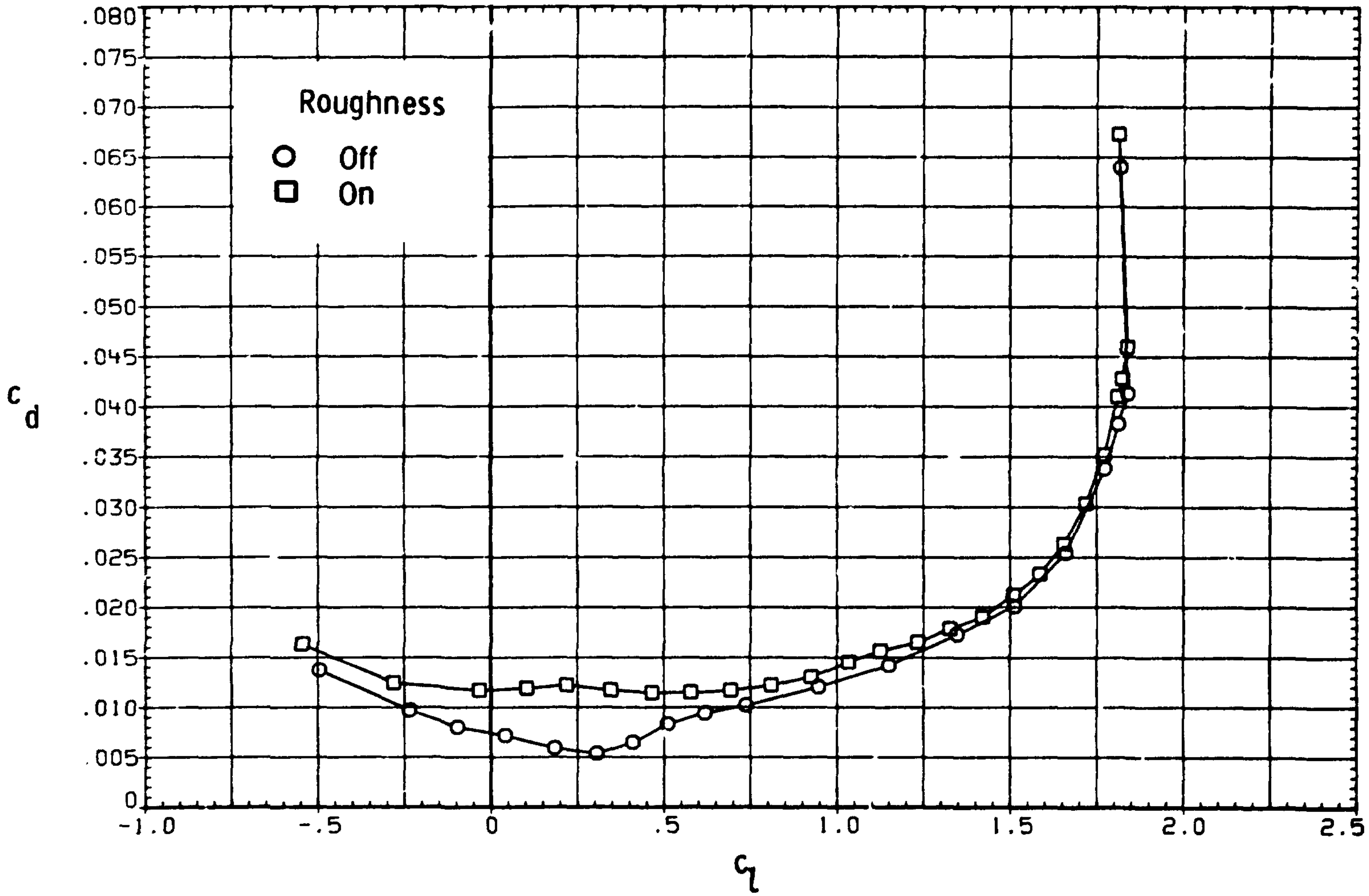

(a) Concluded.

Figure 7.- Continued.

ORIGINAL PAGE IS OF POOR QUALITY

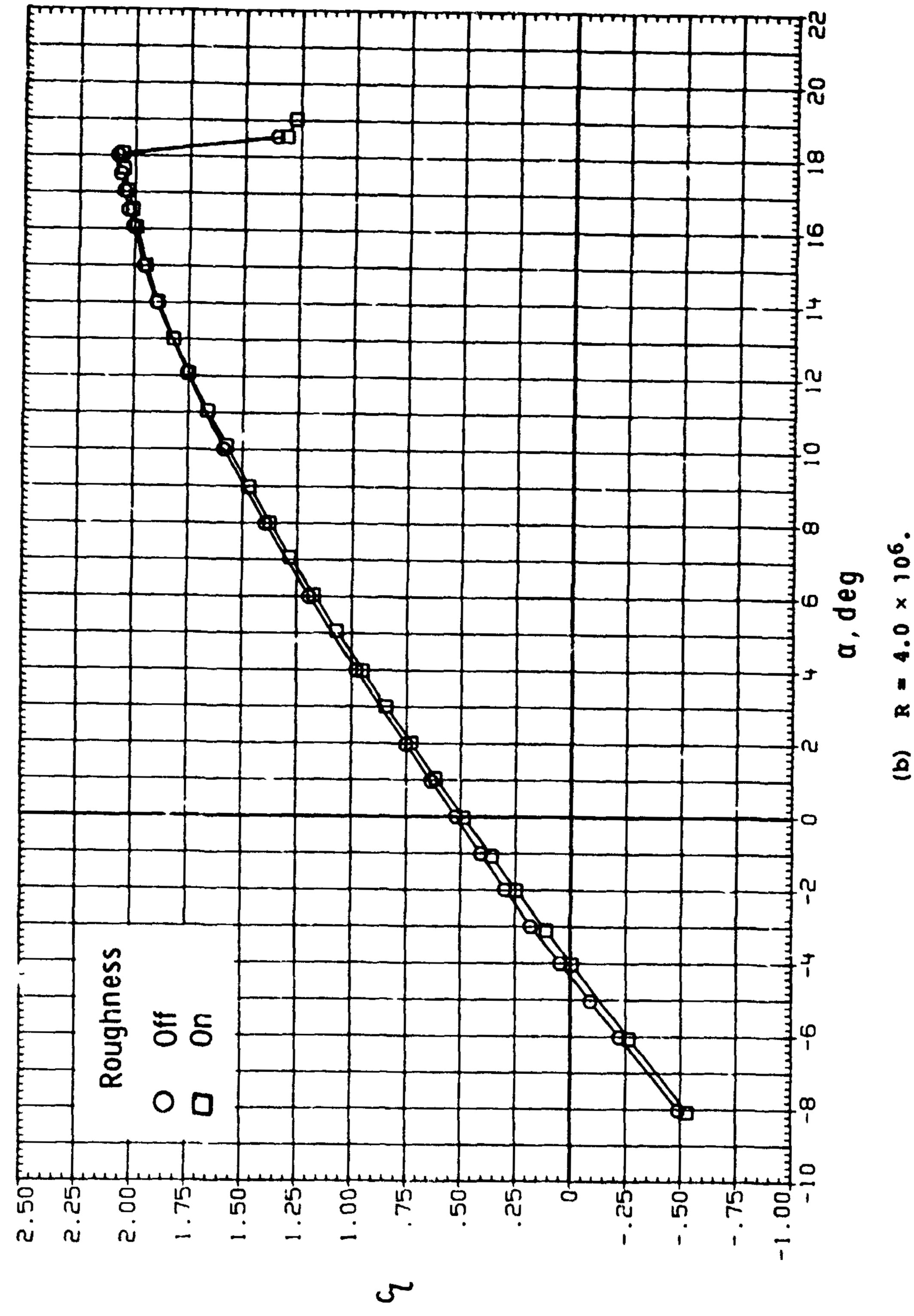

(b) R = 4.0 × 10^6.

Figure 7.- Continued.

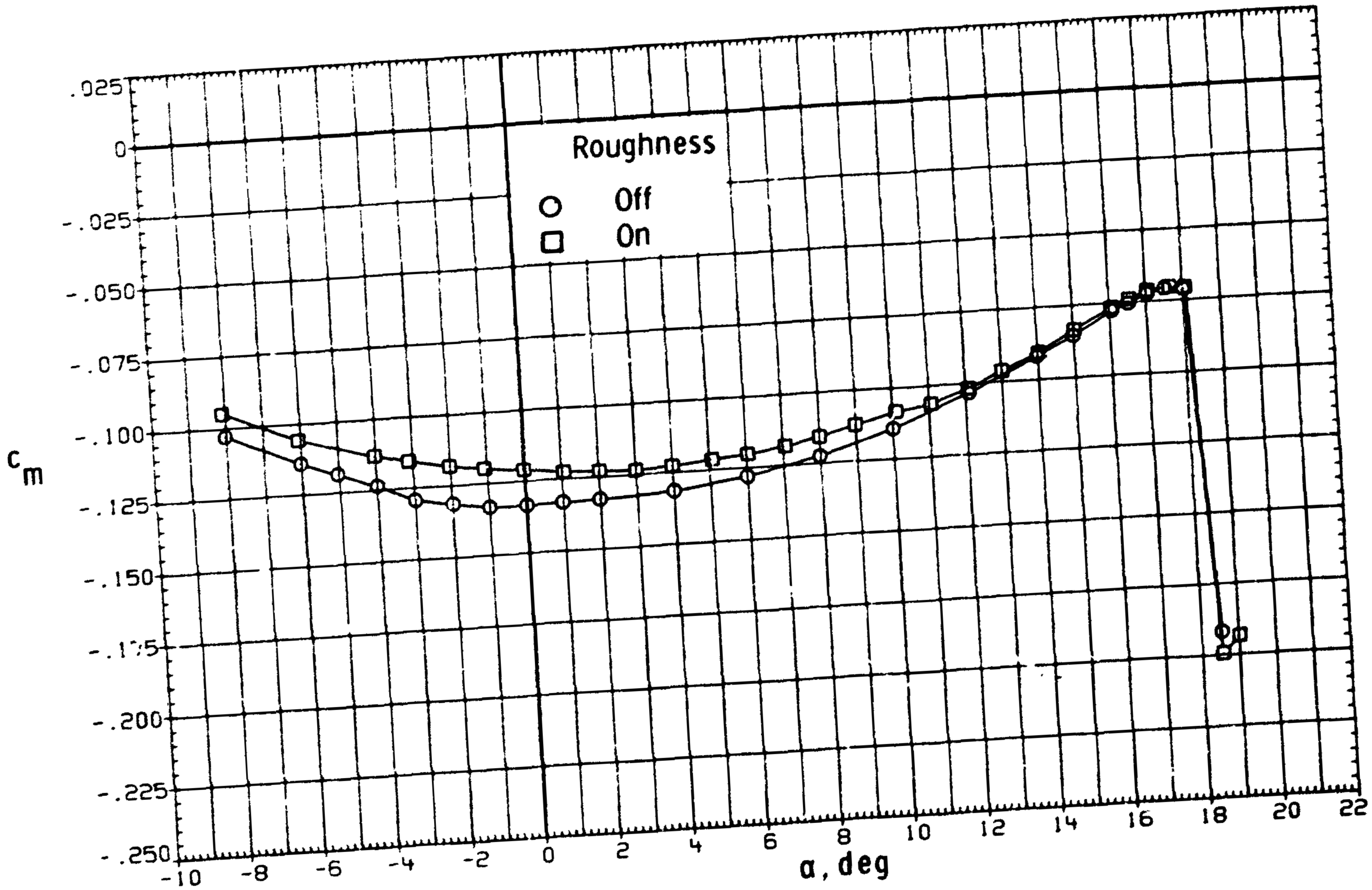

(b) Continued.

Figure 7.- Continued.

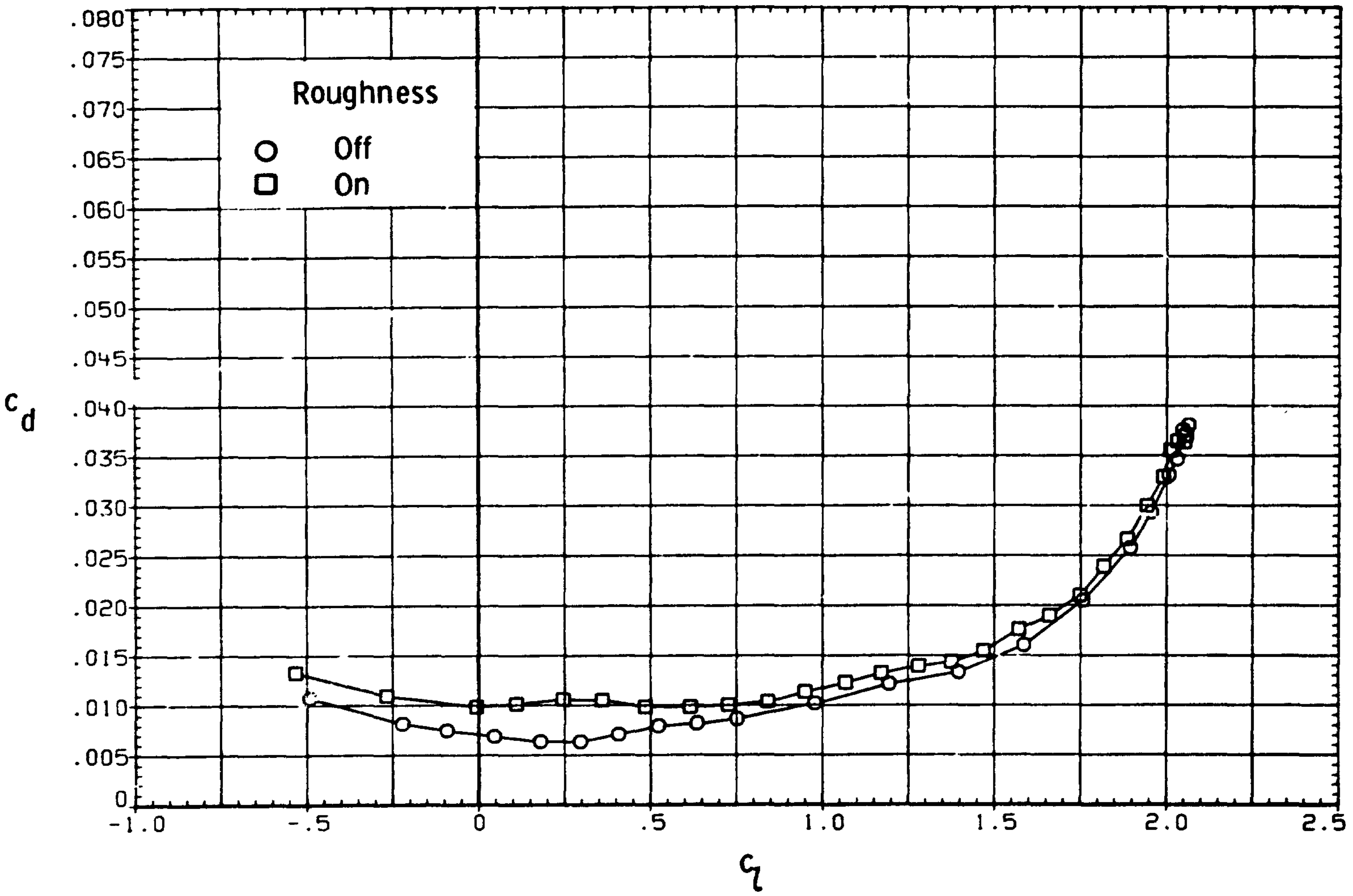

(b) Concluded.

Figure 7.- Continued.

ORIGINAL PAGE IS
OF POOR QUALITY

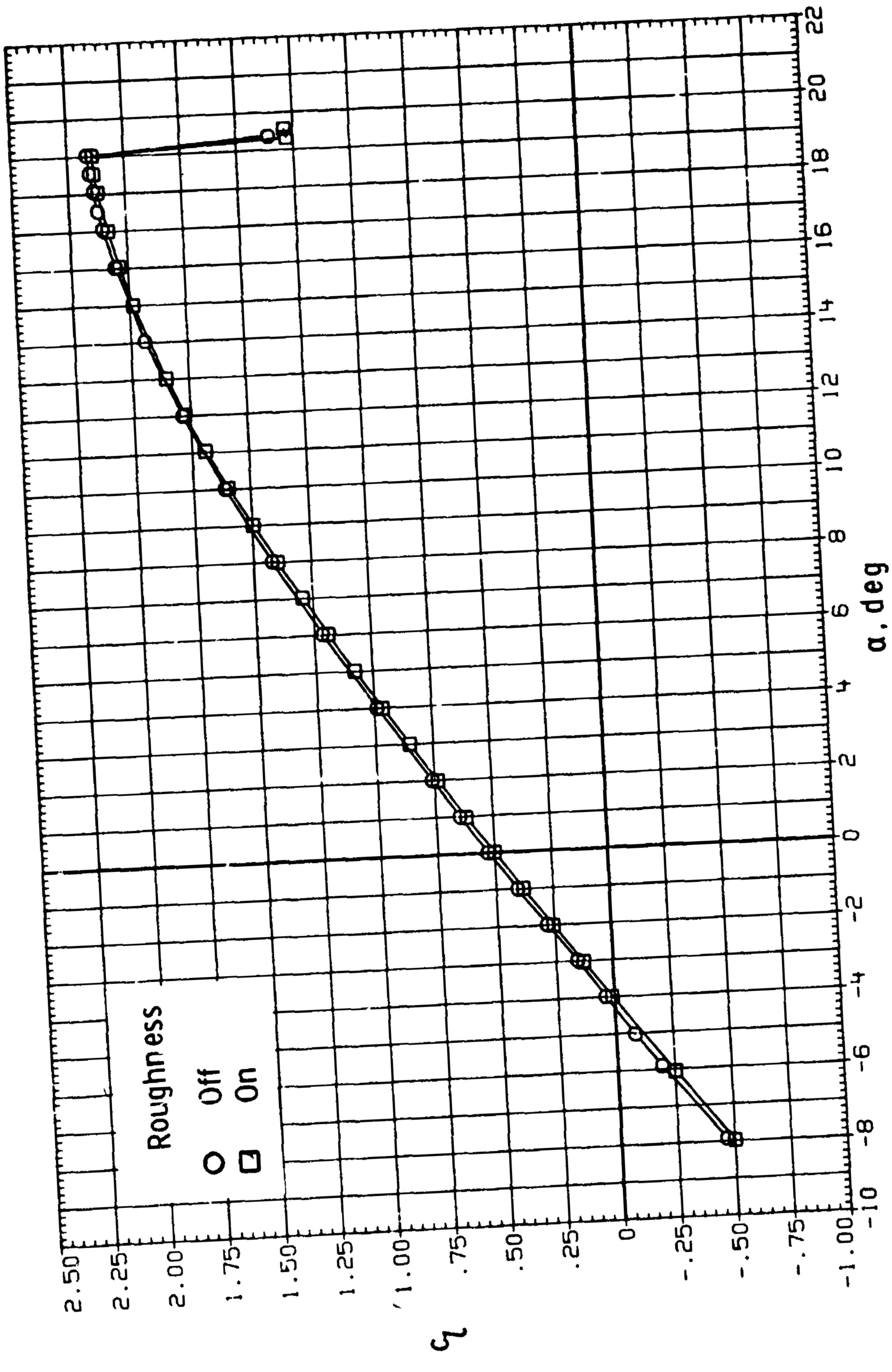

(c) R = 6.0 × 10^6.

Figure 7.- Continued.

ORIGINAL PAGE IS
OF POOR QUALITY

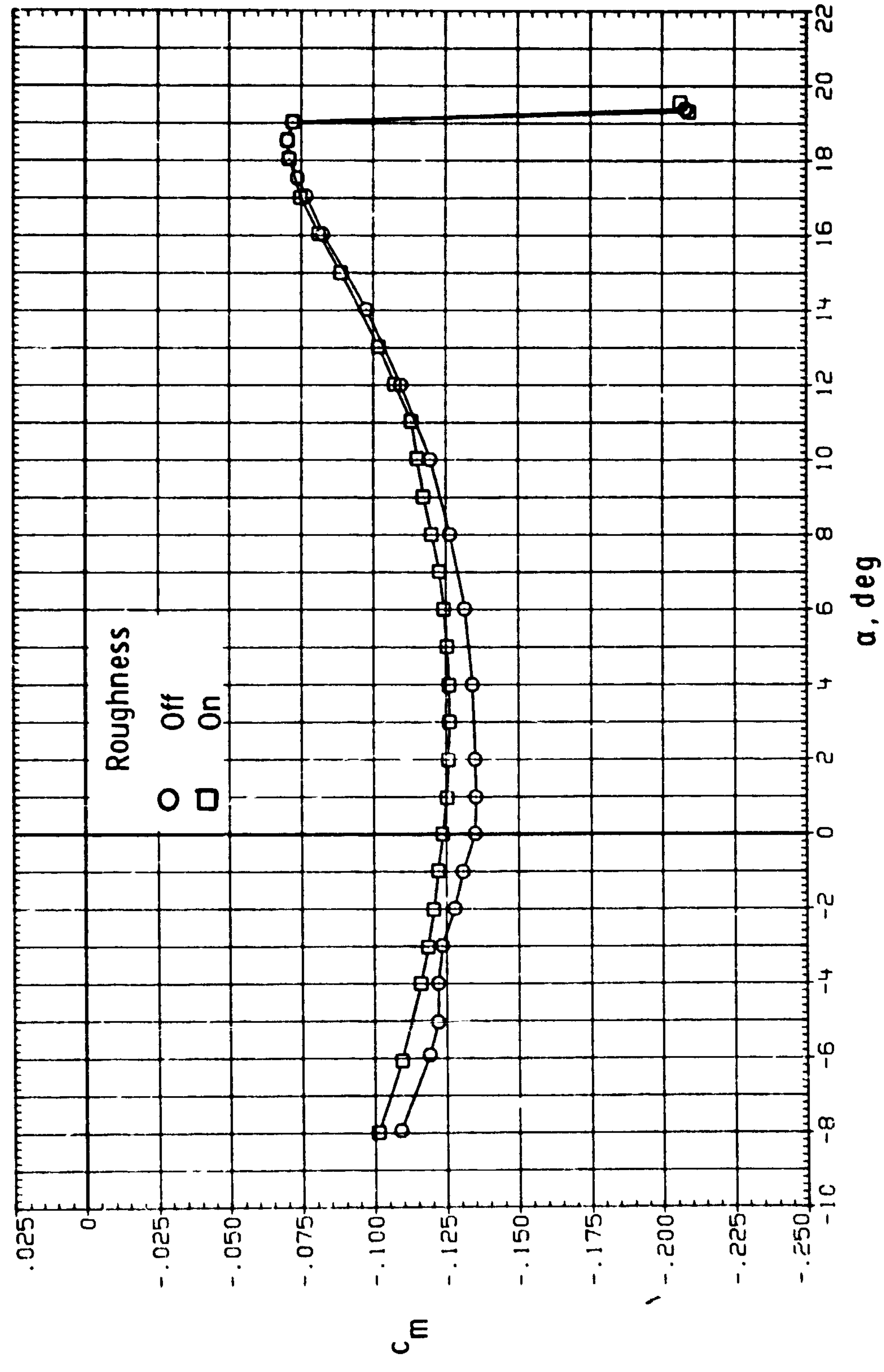

(c) Continued.

Figure 7.- Continued.

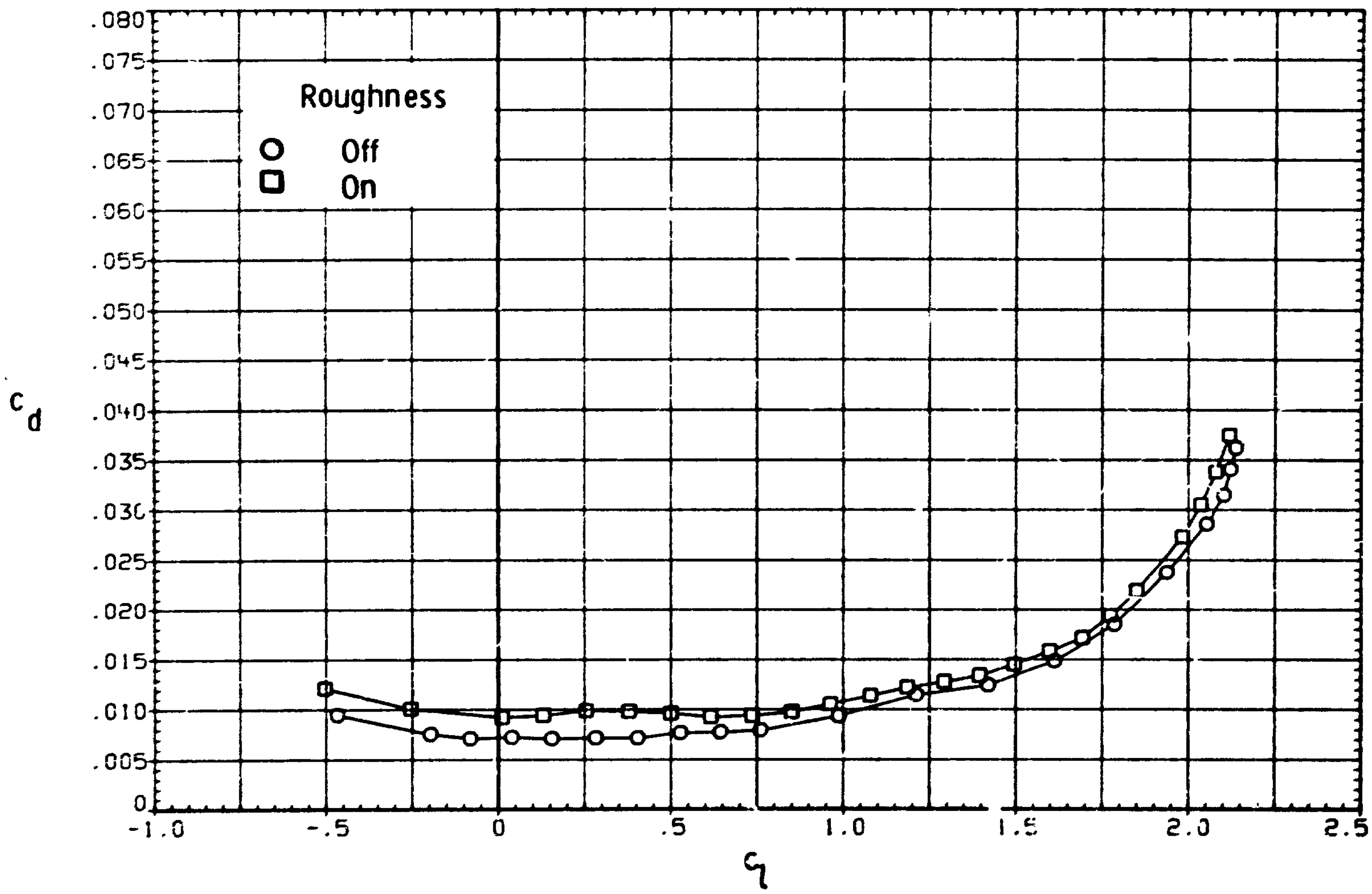

(c) Concluded.

Figure 7.- Continued.

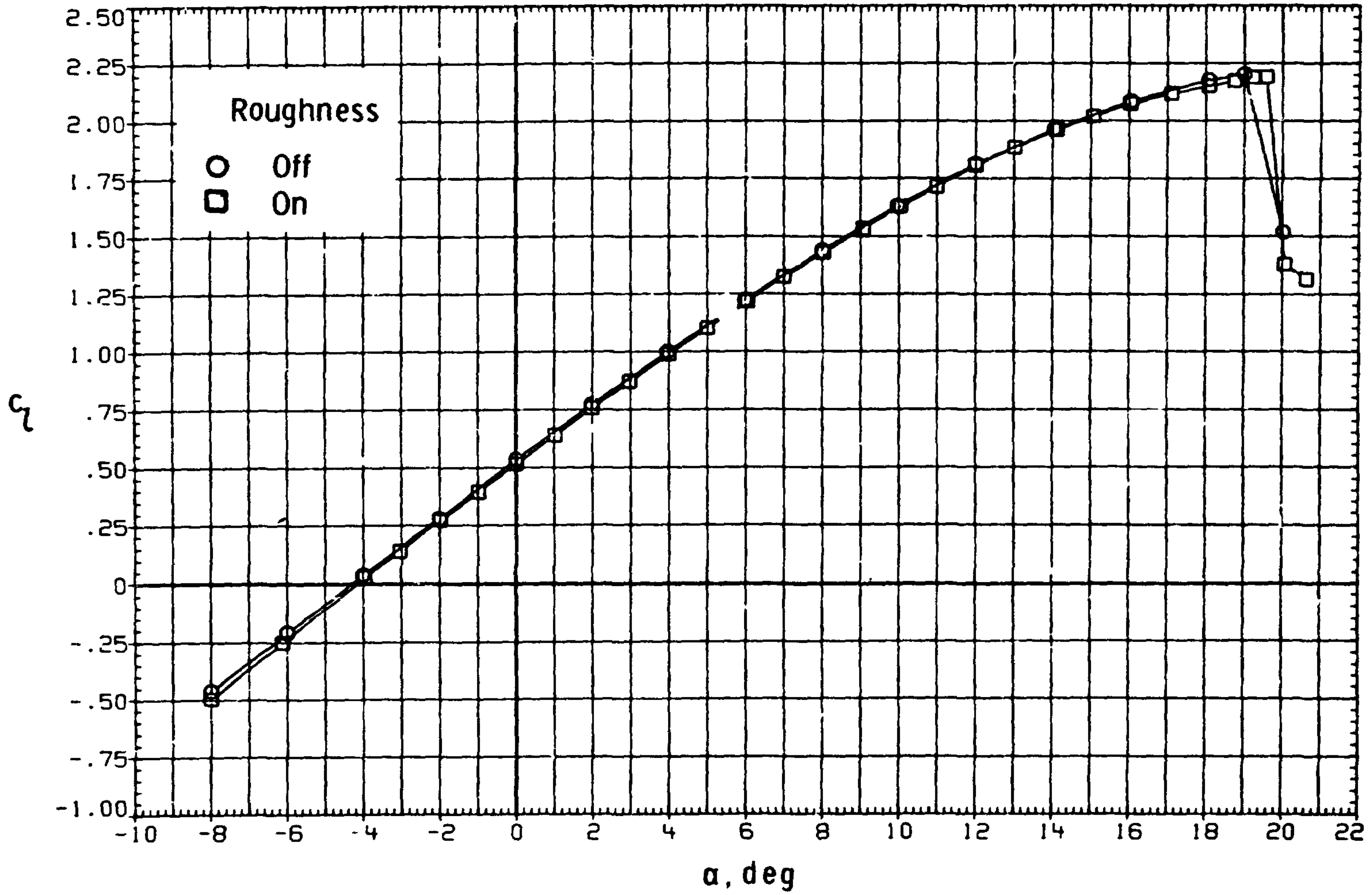

(d) $R = 9.0 \times 10^6$.

Figure 7.- Continued.

ORIGINAL PAGE IS
OF POOR QUALITY

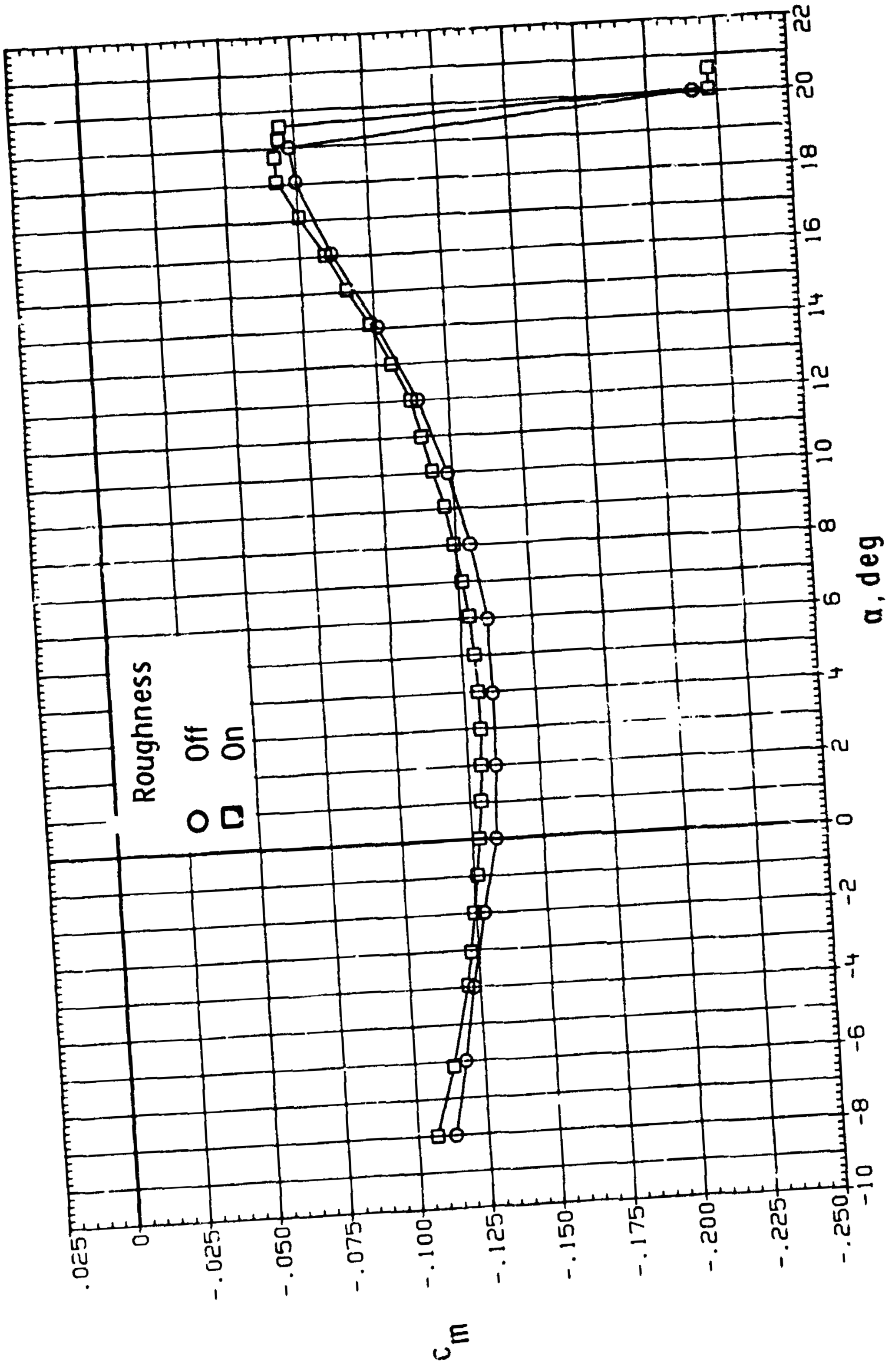

(d) Continued.

Figure 7.- Continued.

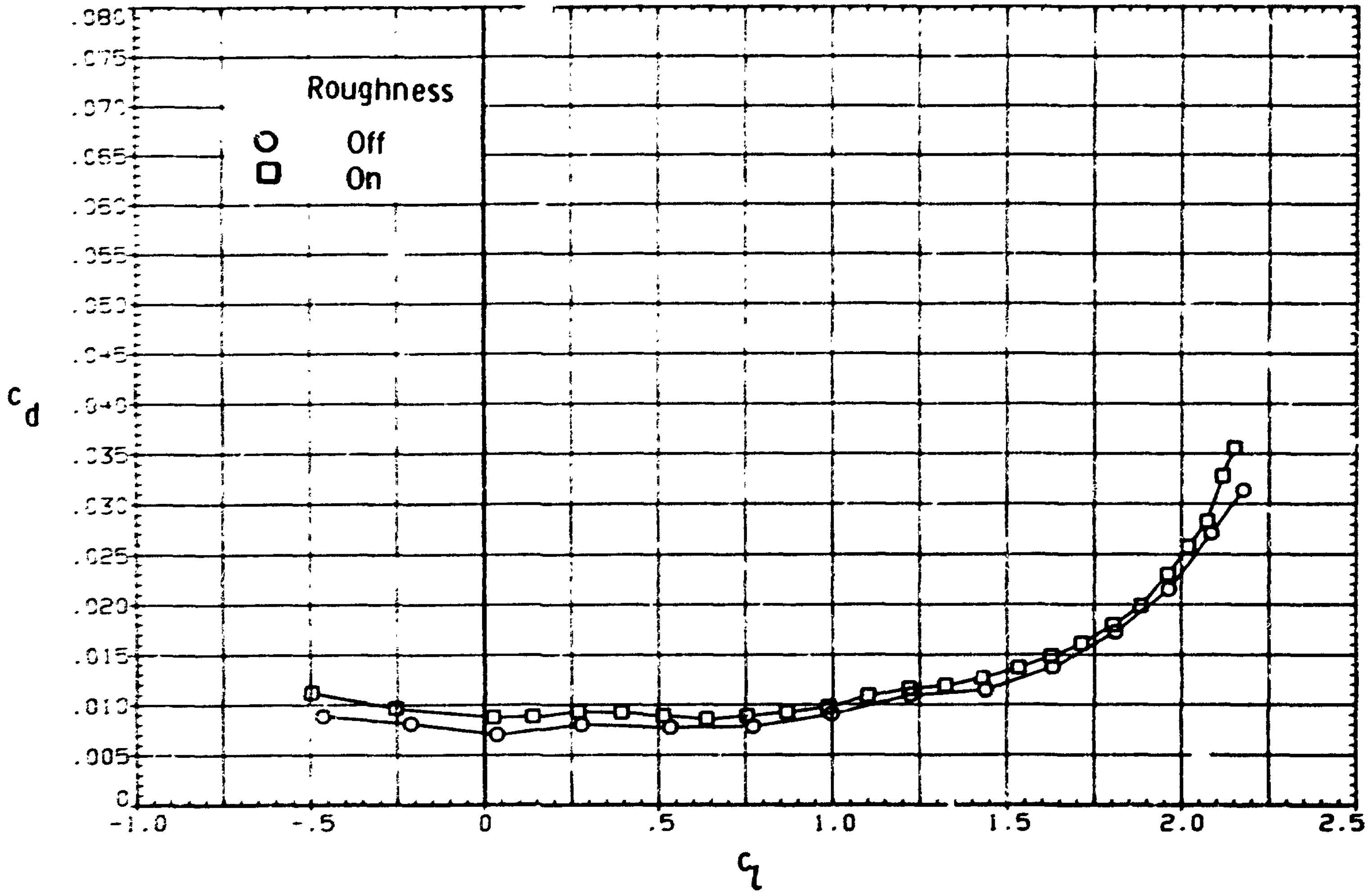

(d) Conluded.

Figure 7.- Continued.

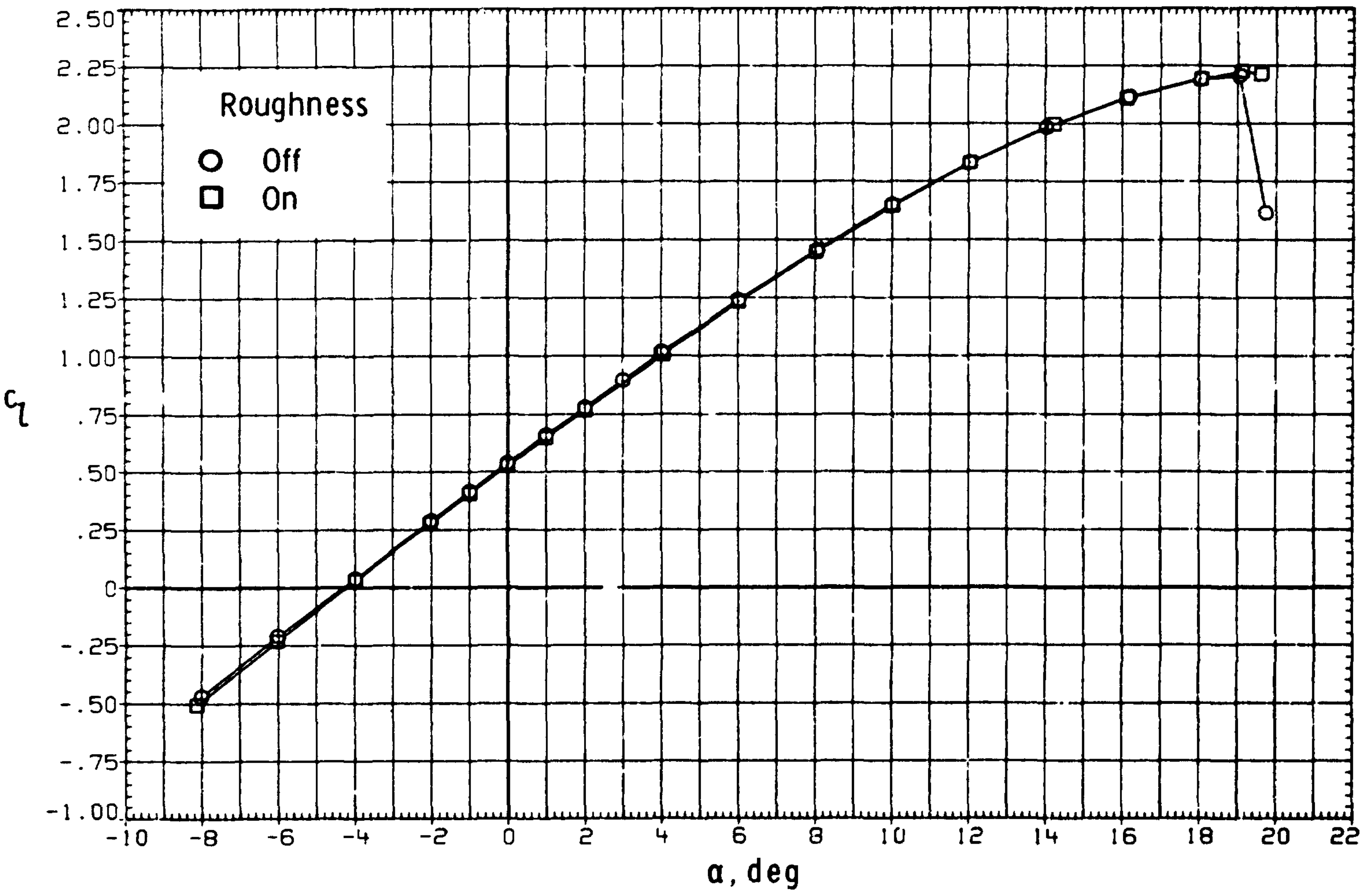

(e) R = 12.0 × 10^6.

Figure 7.- Continued.

ORIGINAL PAGE IS
OF POOR QUALITY

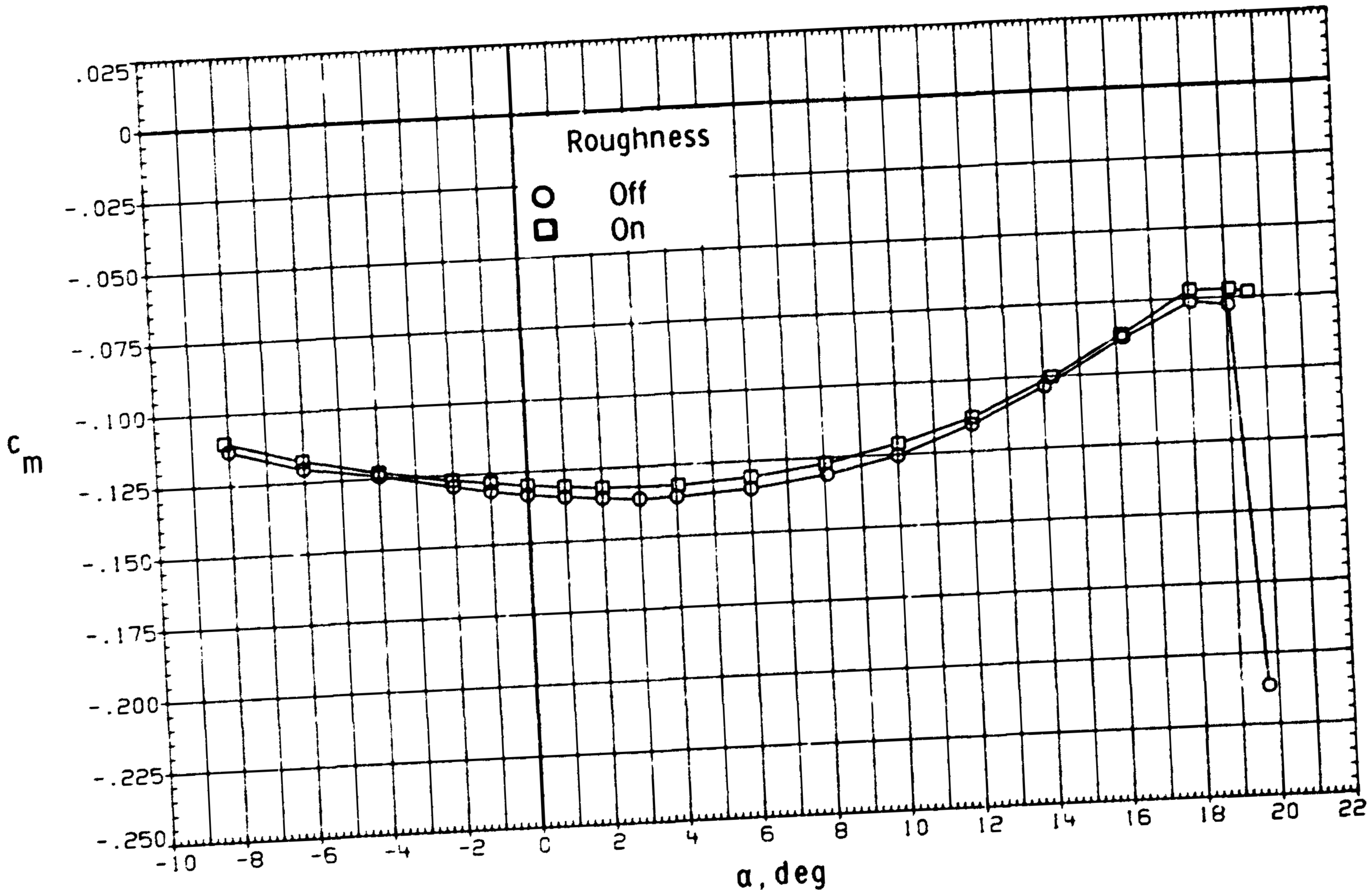

(e) Continued.

Figure 7.- Continued.

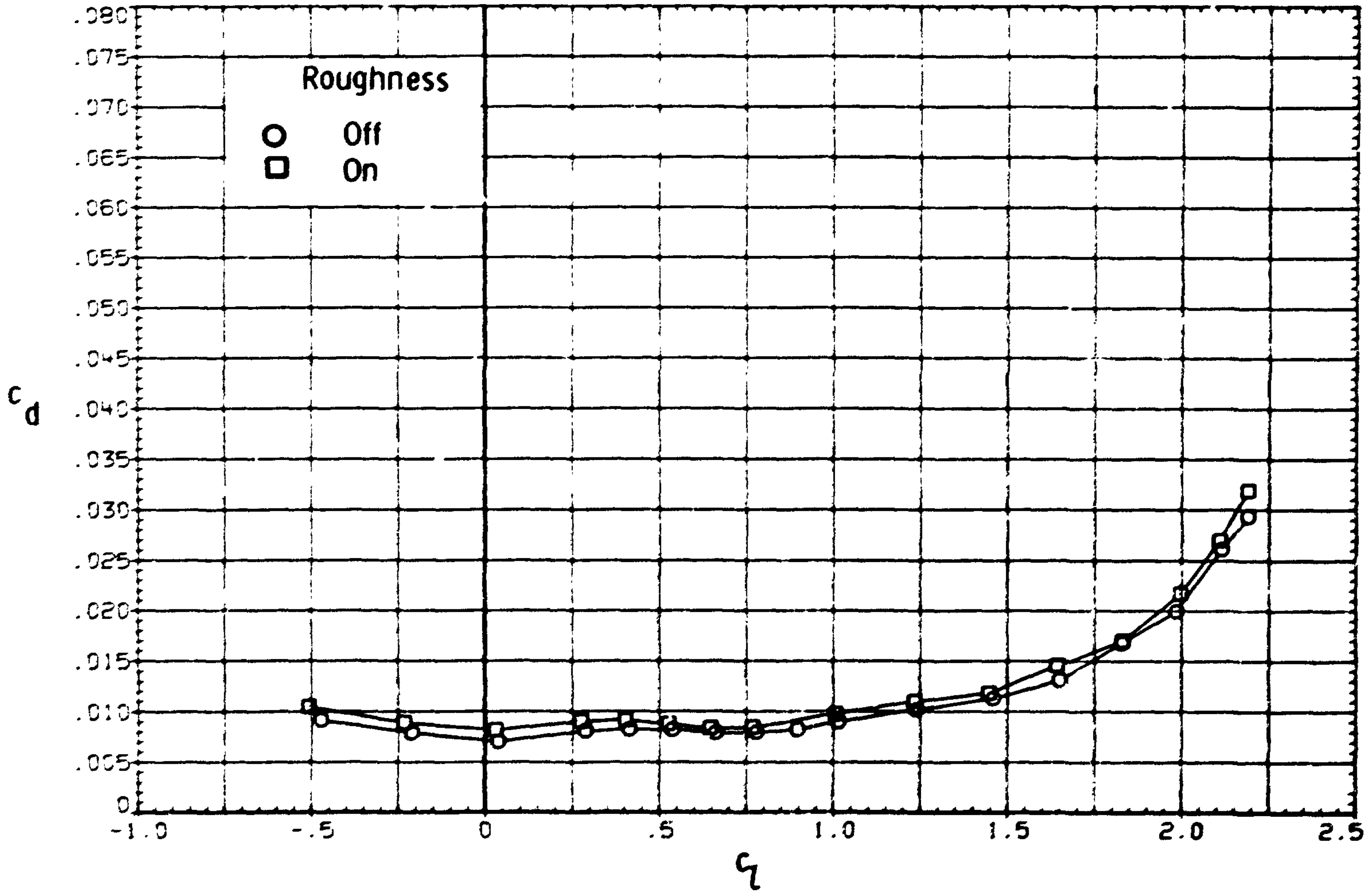

(e) Concluded.

Figure 7.- Continued.

ORIGINAL PAGE IS OF POOR QUALITY

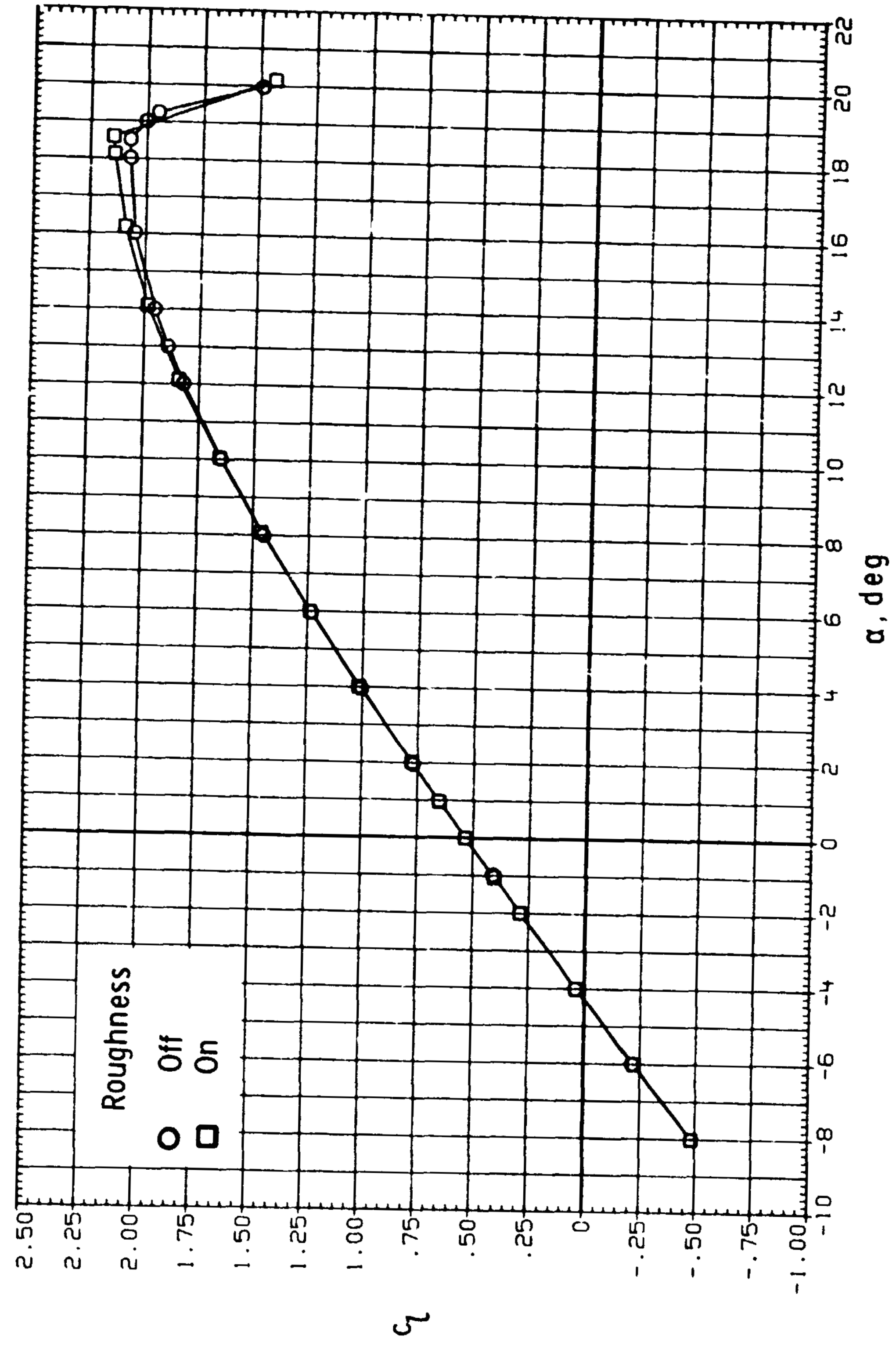

(f) $R = 18.0 \times 10^6$.

Figure 7.- Continued.

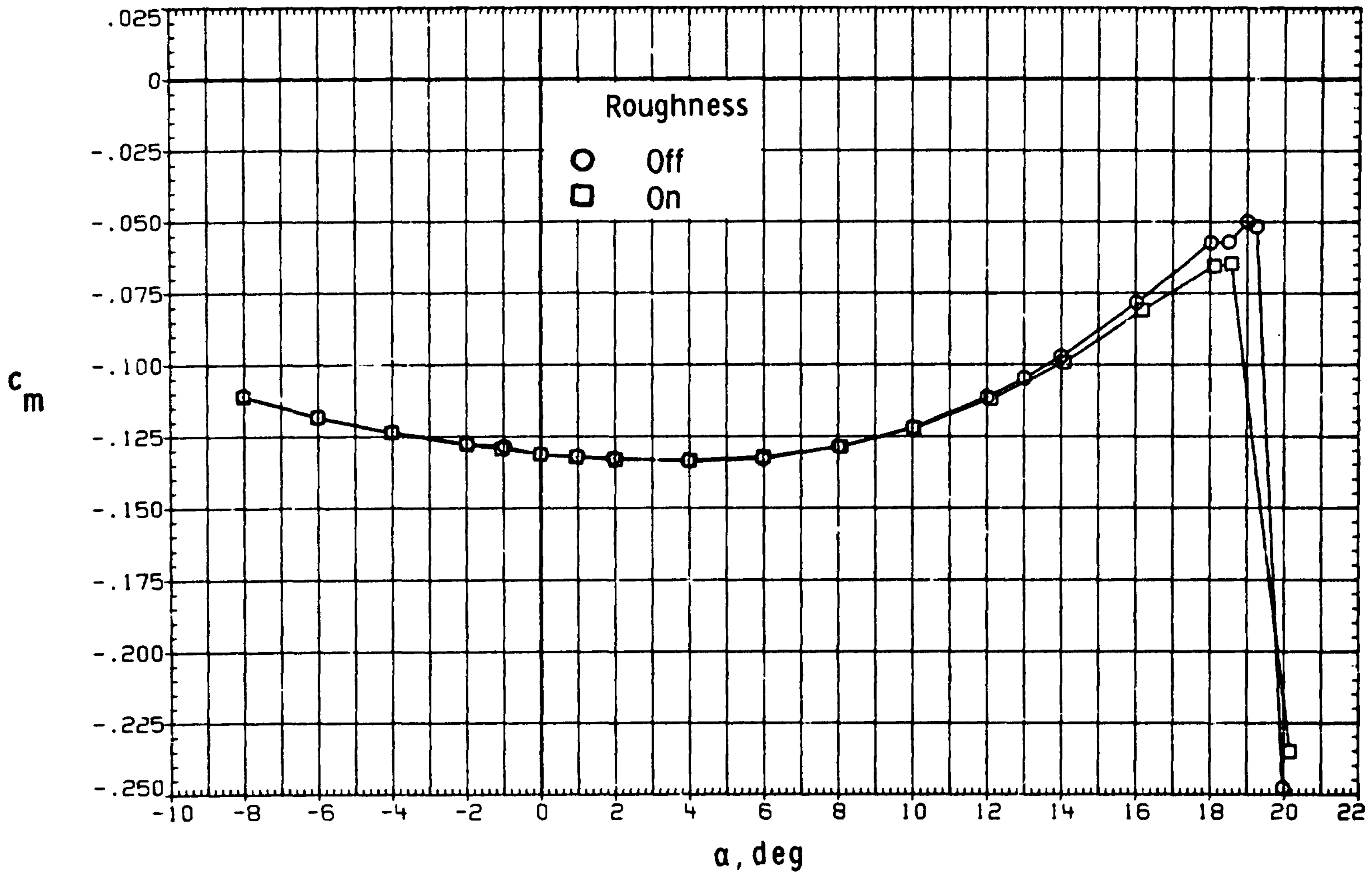

(f) Continued.

Figure 7.- Continued.

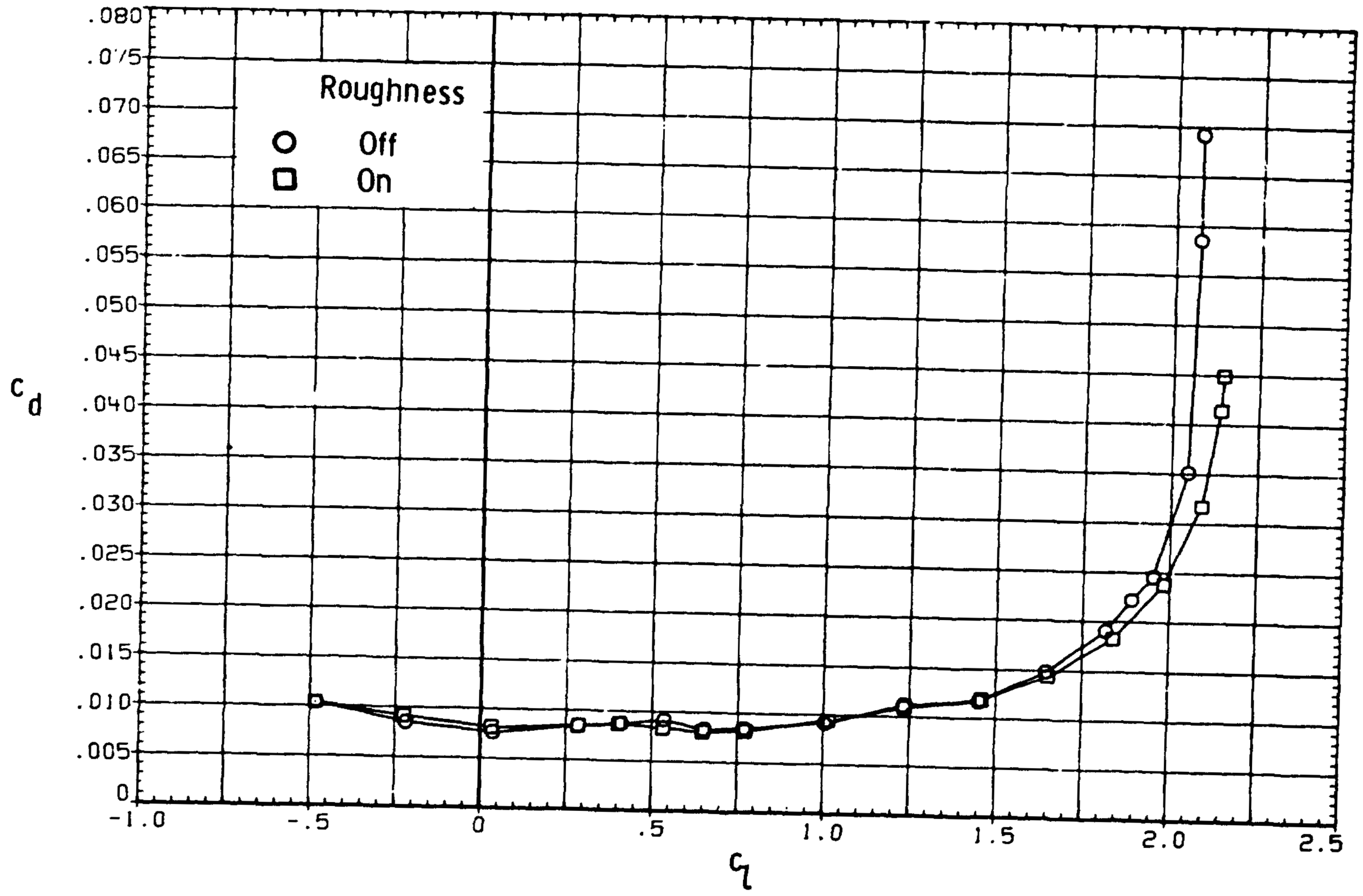

(f) Concluded.

Figure 7.- Concluded.

**ORIGINAL PAGE IS
OF POOR QUALITY**

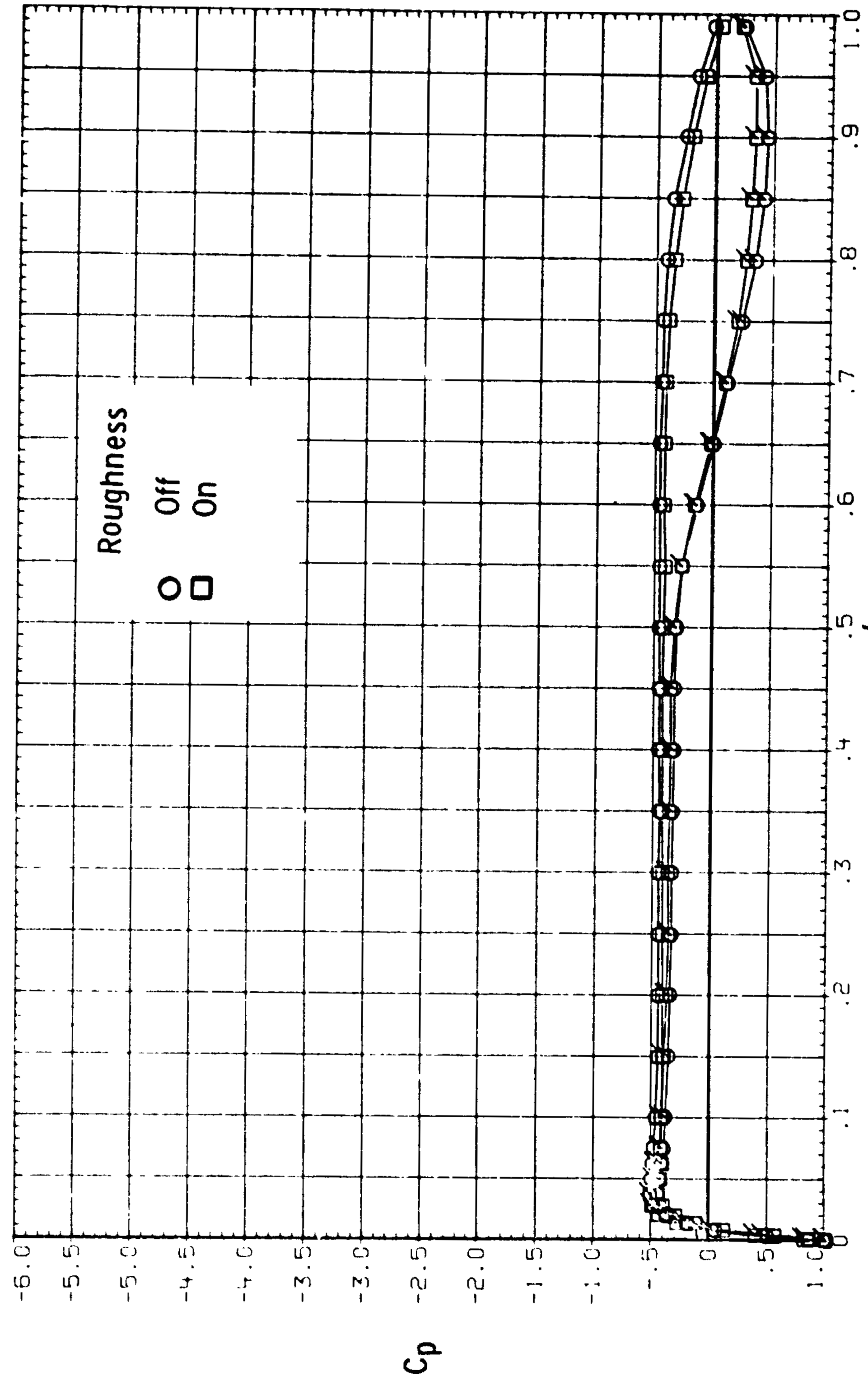

(a) $R = 2.0 \times 10^6$, $\alpha = -2^\circ$.

Figure 8.- Effect of fixing transition on chordwise pressure distributions; $M = 0.15$. (Flagged symbols indicate lower surface.)

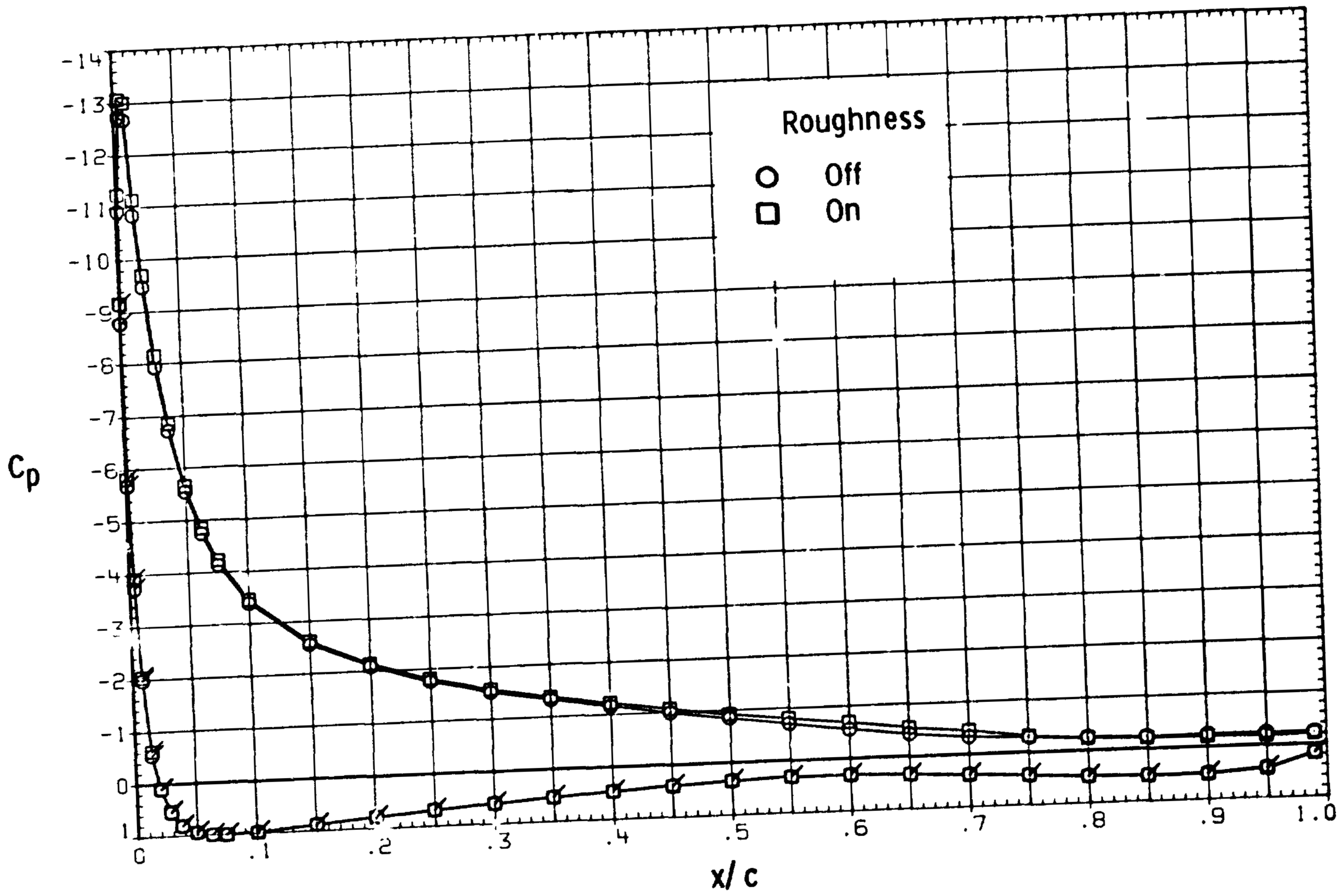

(b) R = 18.0 × 10^6, α = 18°.

Figure 8.- Concluded.

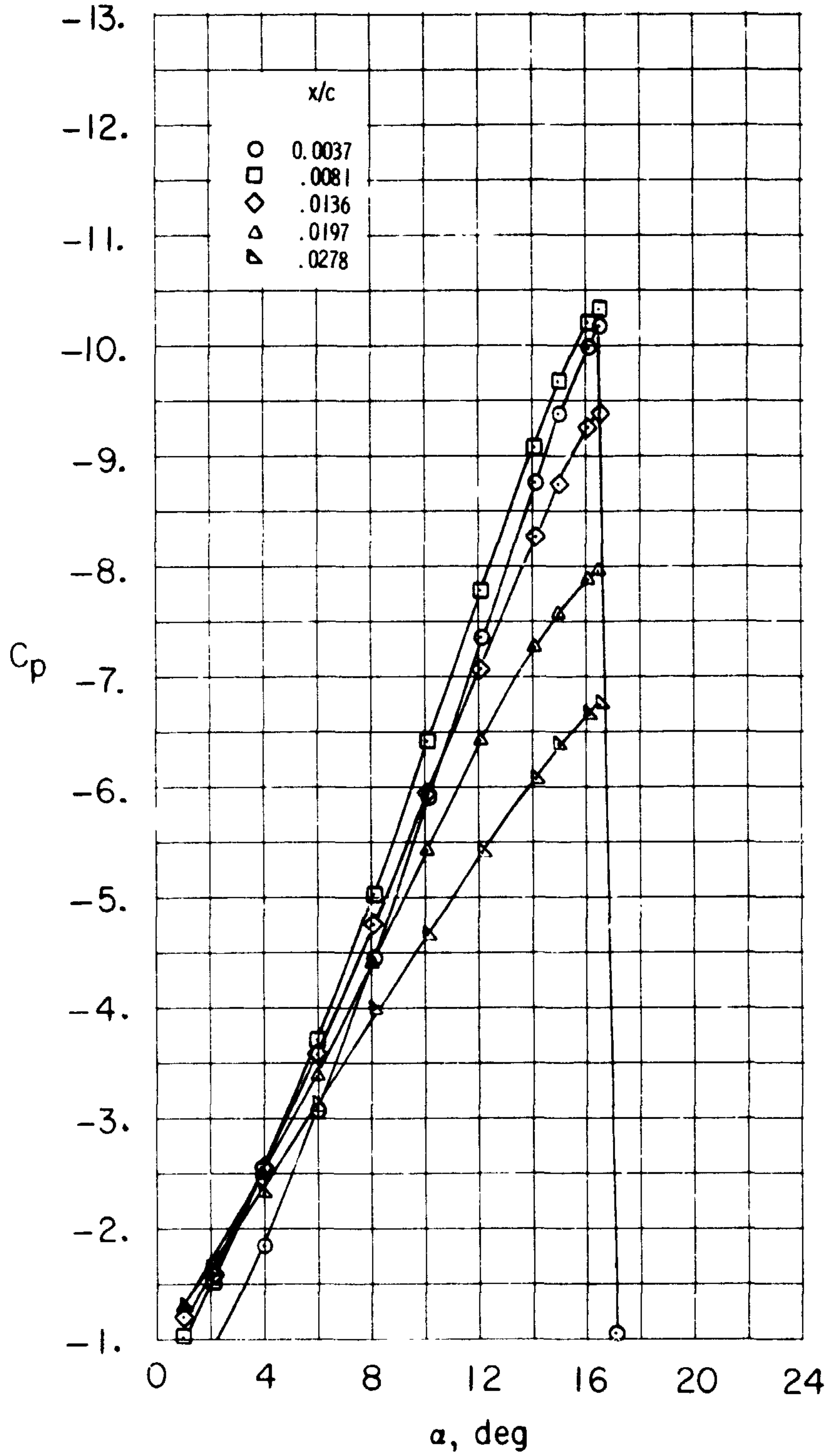

(a) $R = 2.0 \times 10^6$.

Figure 9.- Variation of pressure coefficient on upper surface at particular chordwise stations with angle of attack; M = 0.15. model smooth.

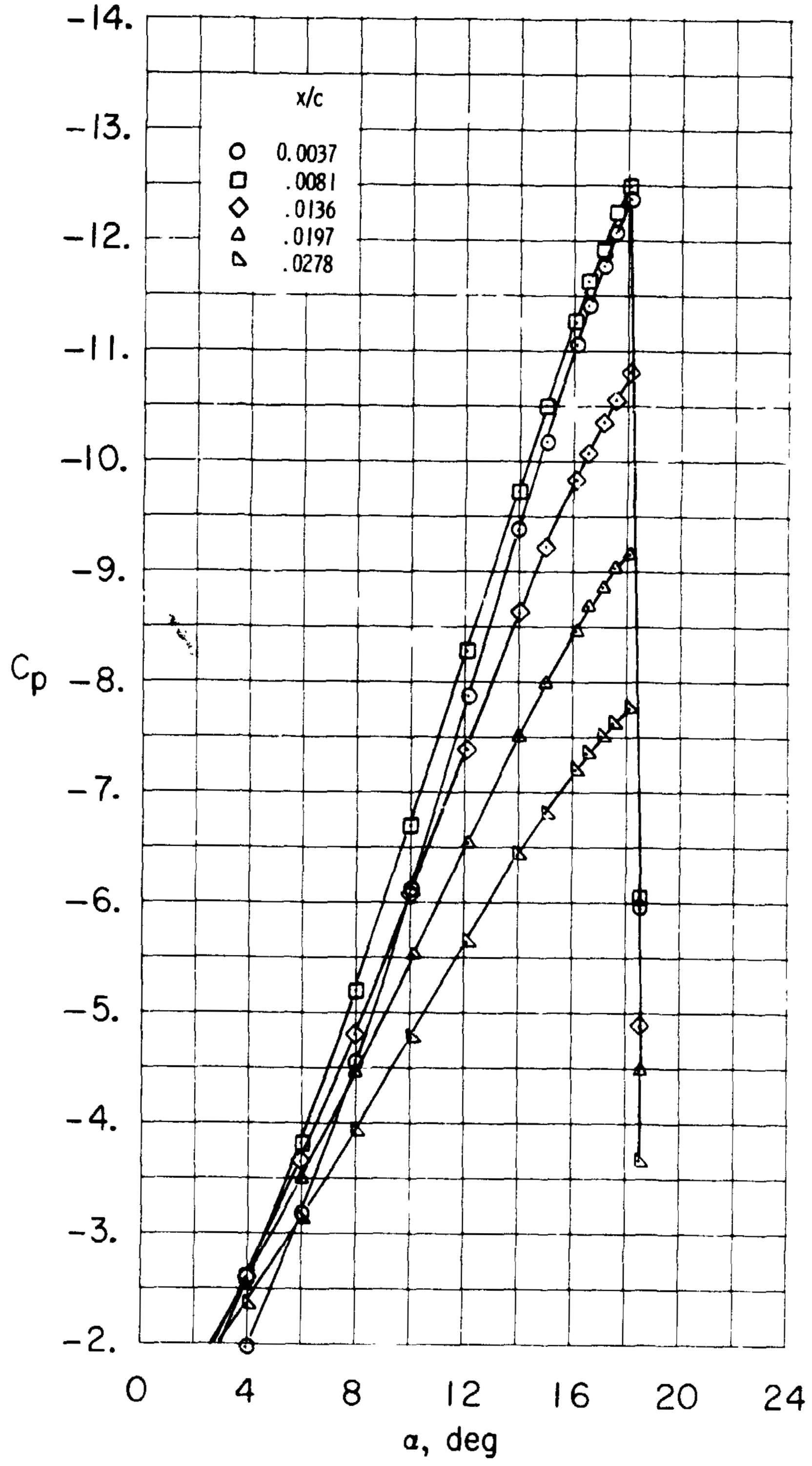

(b) R = 4.0 × 10^6.

Figure 9.- Continued.

ORIGINAL PAGE IS
OF POOR QUALITY

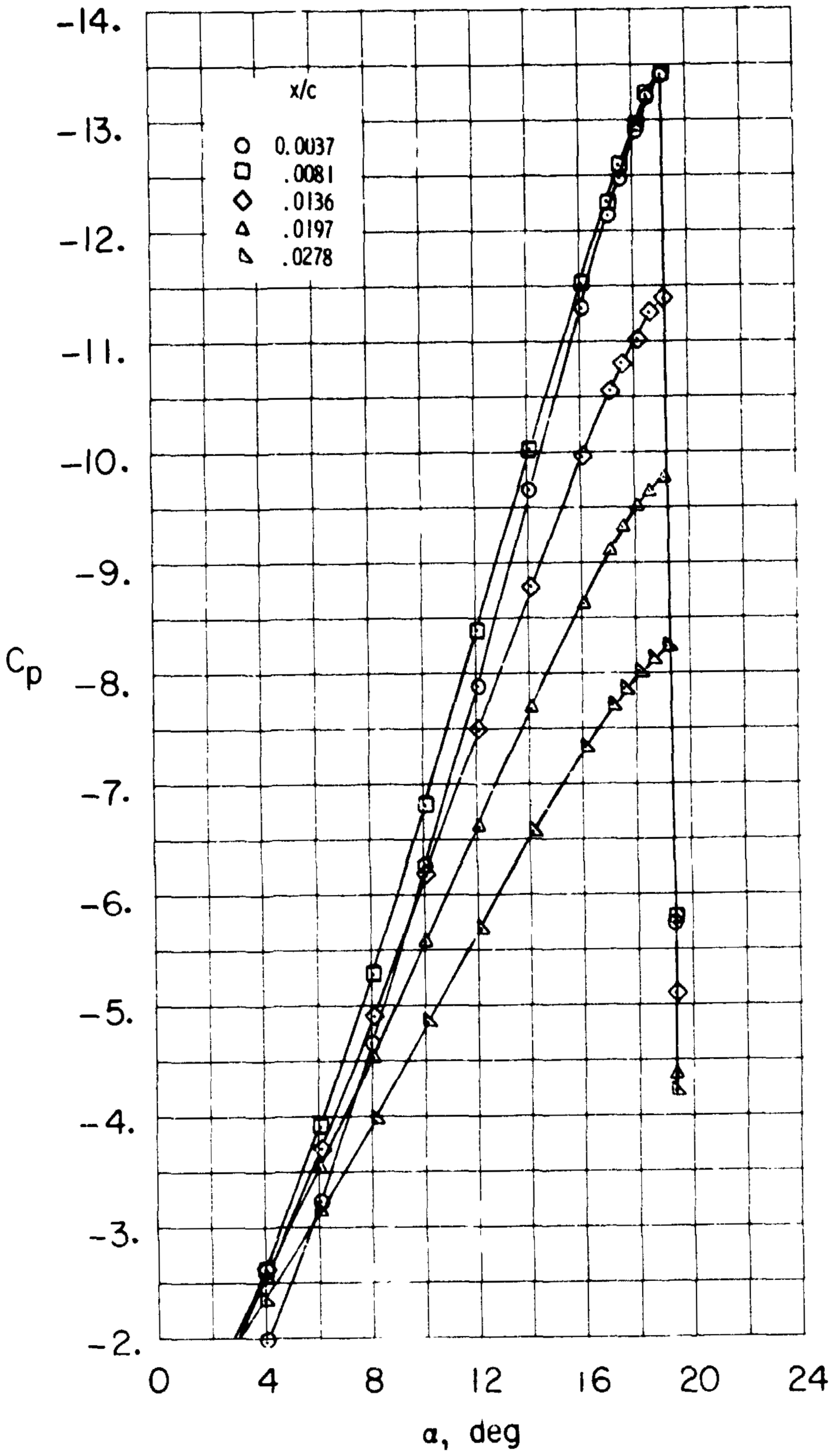

(c) $R = 6.0 \times 10^6$.

Figure 9.- Continued.

ORIGINAL PAGE IS
OF POOR QUALITY

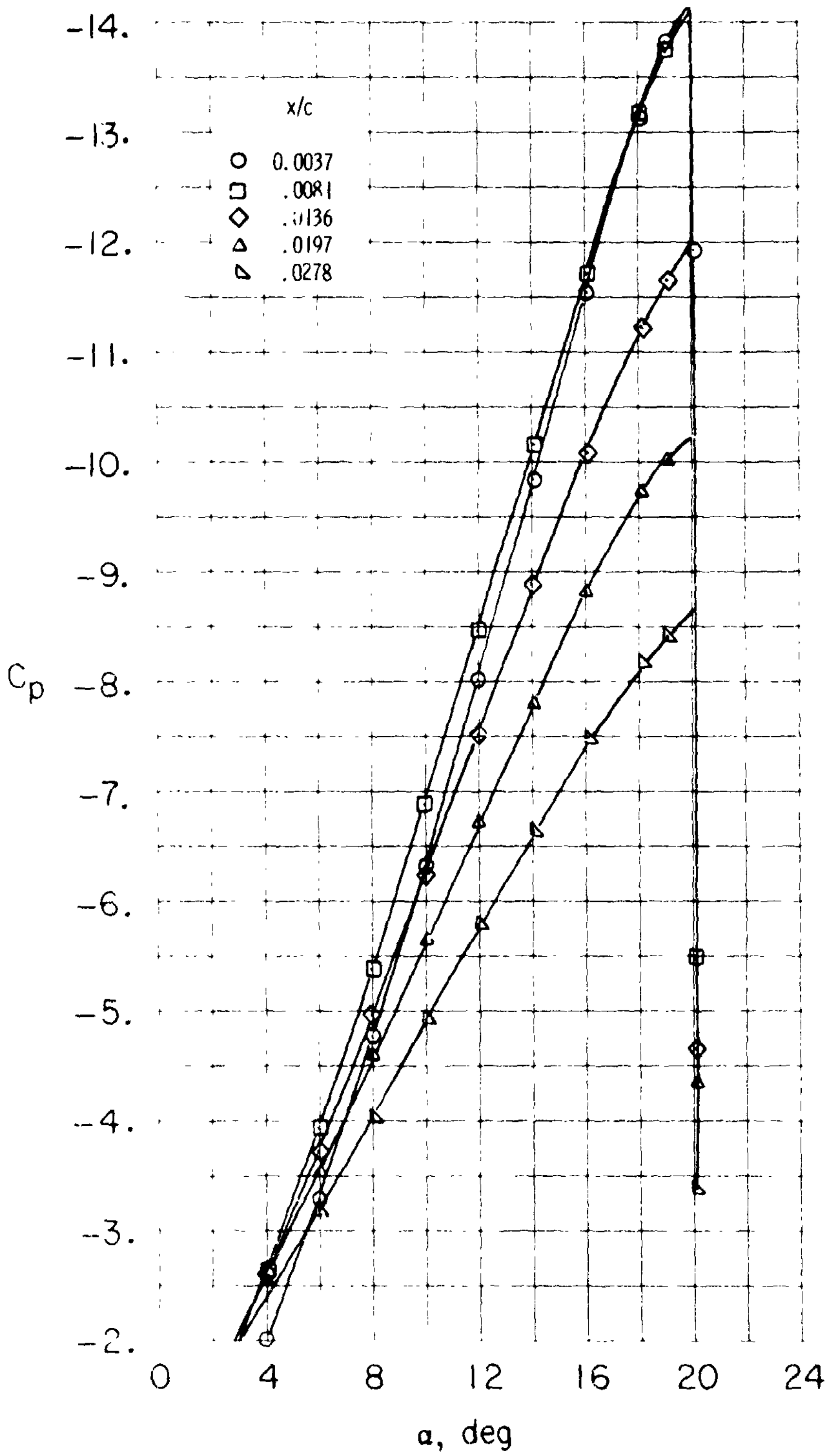

(d) R = 9.0 × 10^6.

Figure 9.- Continued.

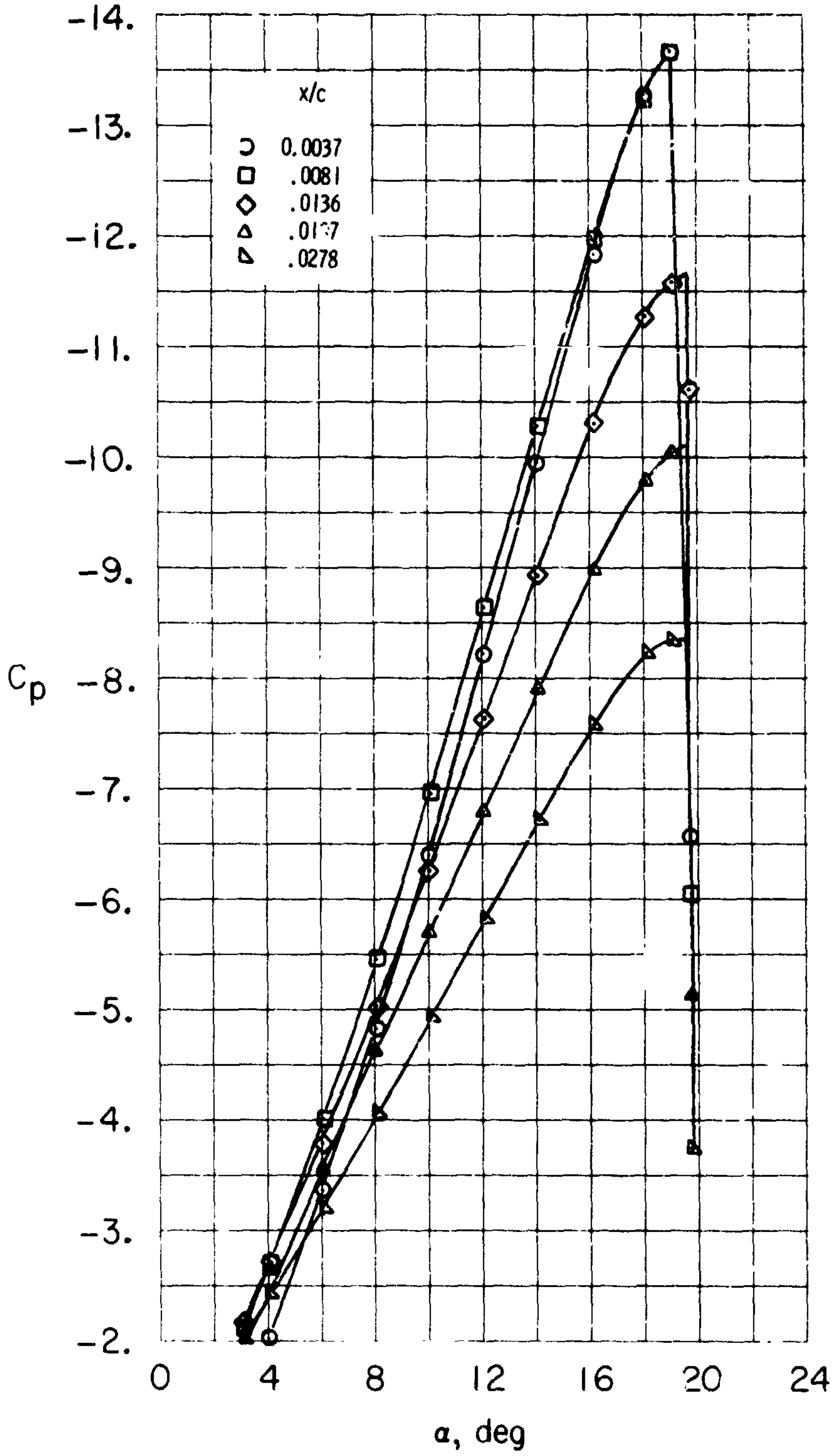

(e) R = 12.0 × 10^6.

Figure 9.- Continued.

ORIGINAL PAGE IS
OF POOR QUALITY

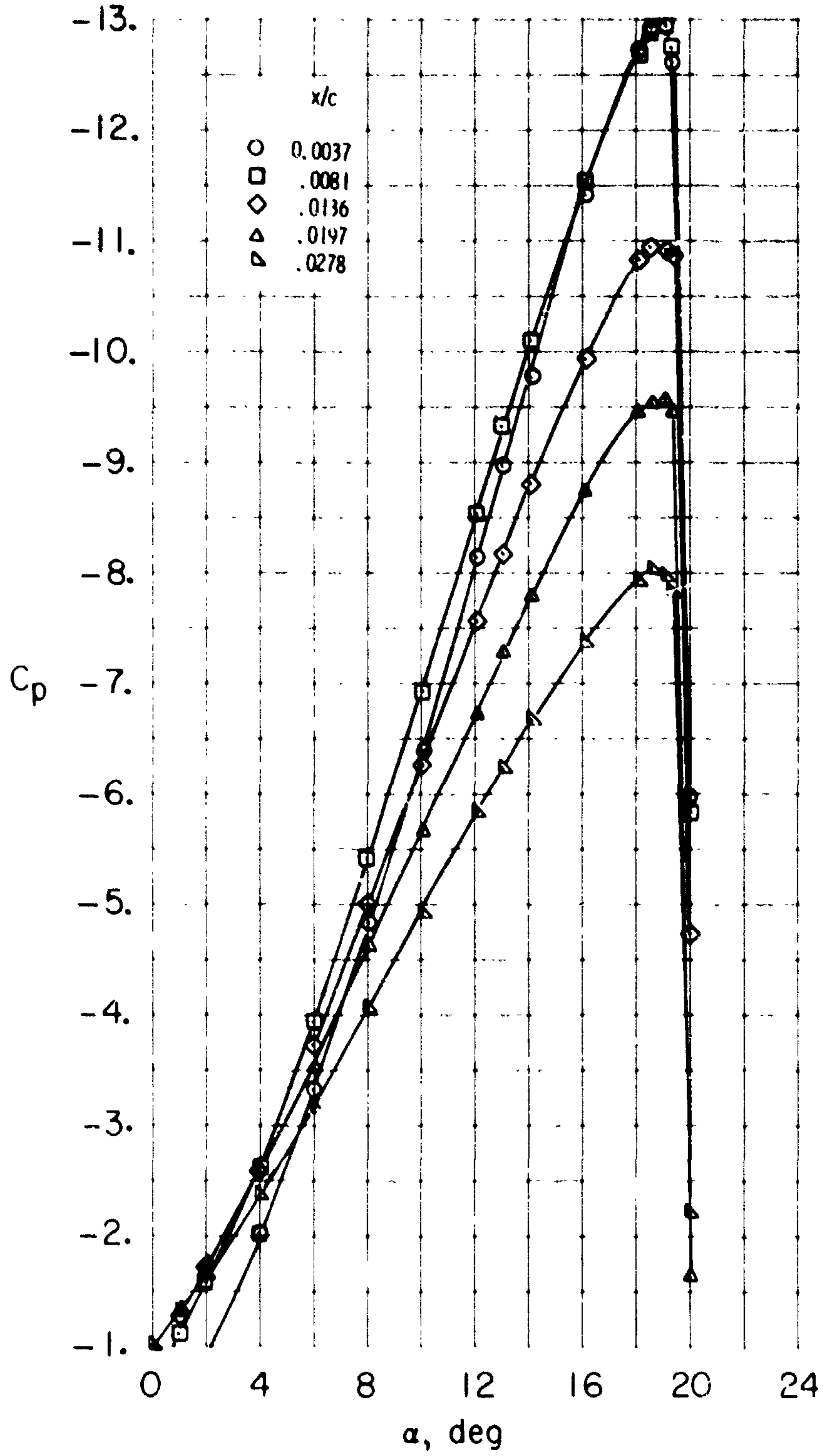

(f) $R = 18.0 \times 10^6$.

Figure 9.- Concluded.

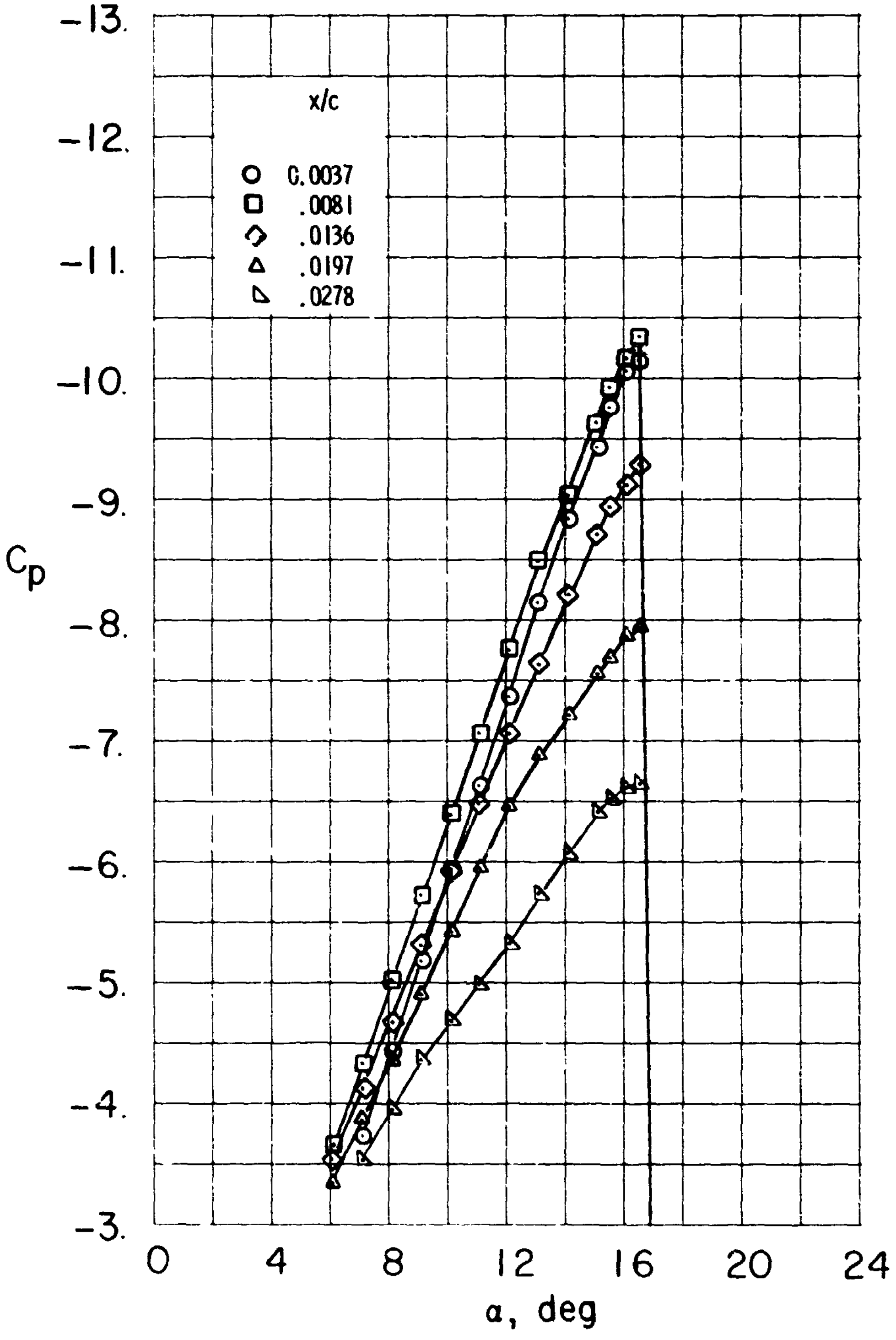

(a) R = 2.0 × 10^6.

Figure 10.- Variation of pressure coefficient on upper surface at particular chordwise stations with angle of attack; M = 0.15, transition fixed.

ORIGINAL PAGE IS
OF POOR QUALITY

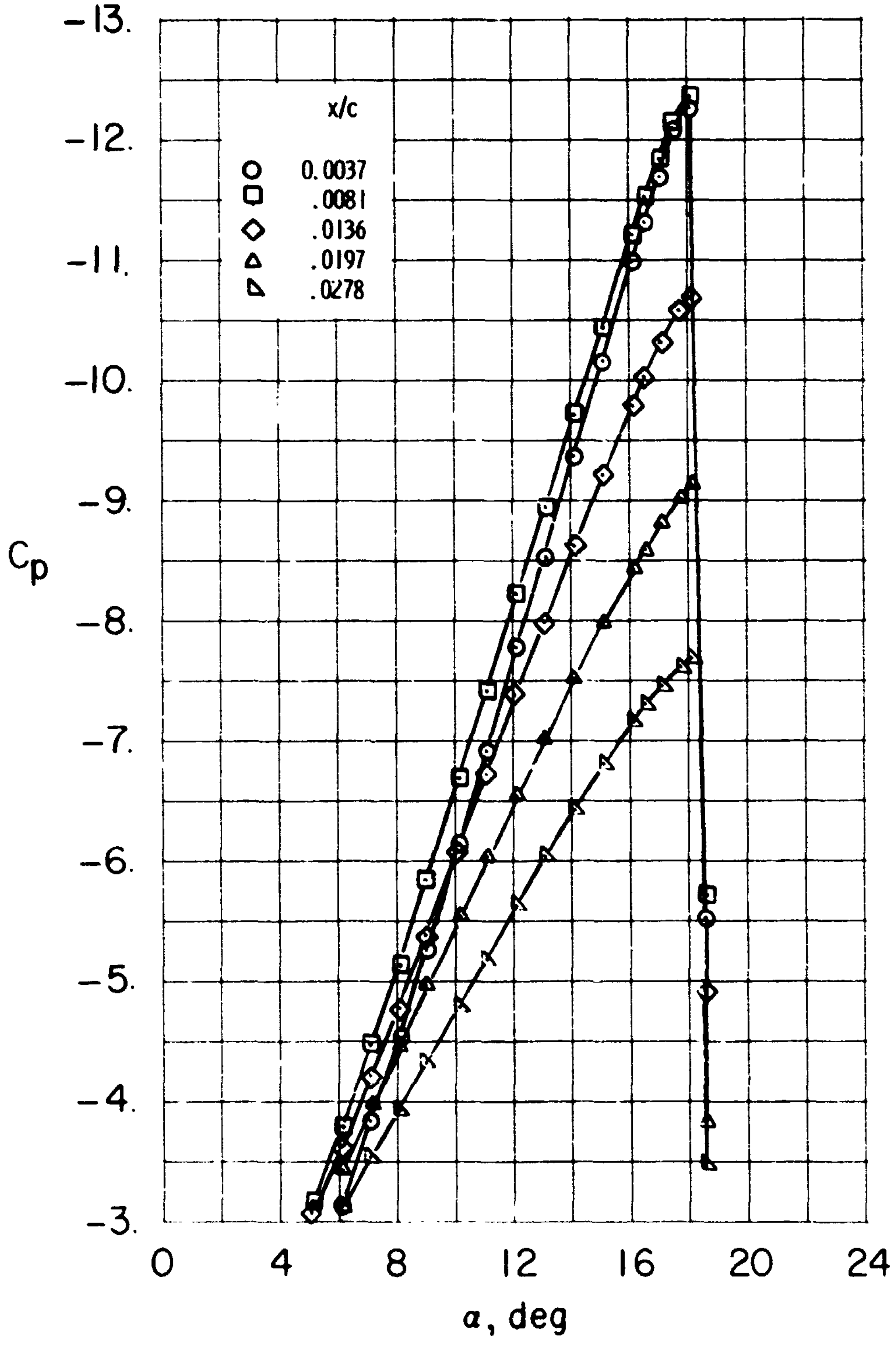

(b) R = 4.0 × 10^6.

Figure 10.- Continued.

ORIGINAL PAGE IS
OF POOR QUALITY

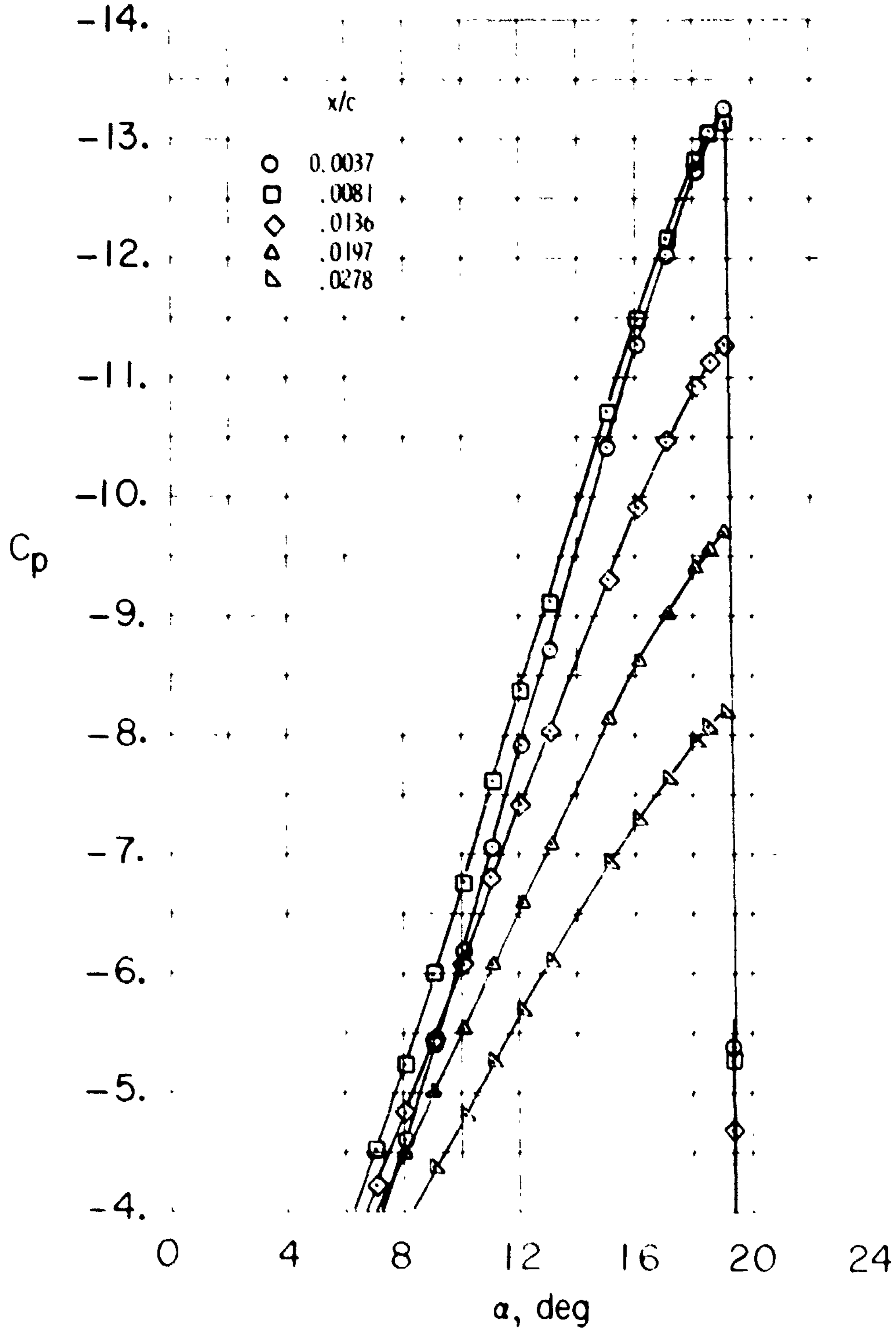

(c) $R = 6.0 \times 10^6$.

Figure 10.- Continued.

ORIGINAL PAGE IS OF POOR QUALITY

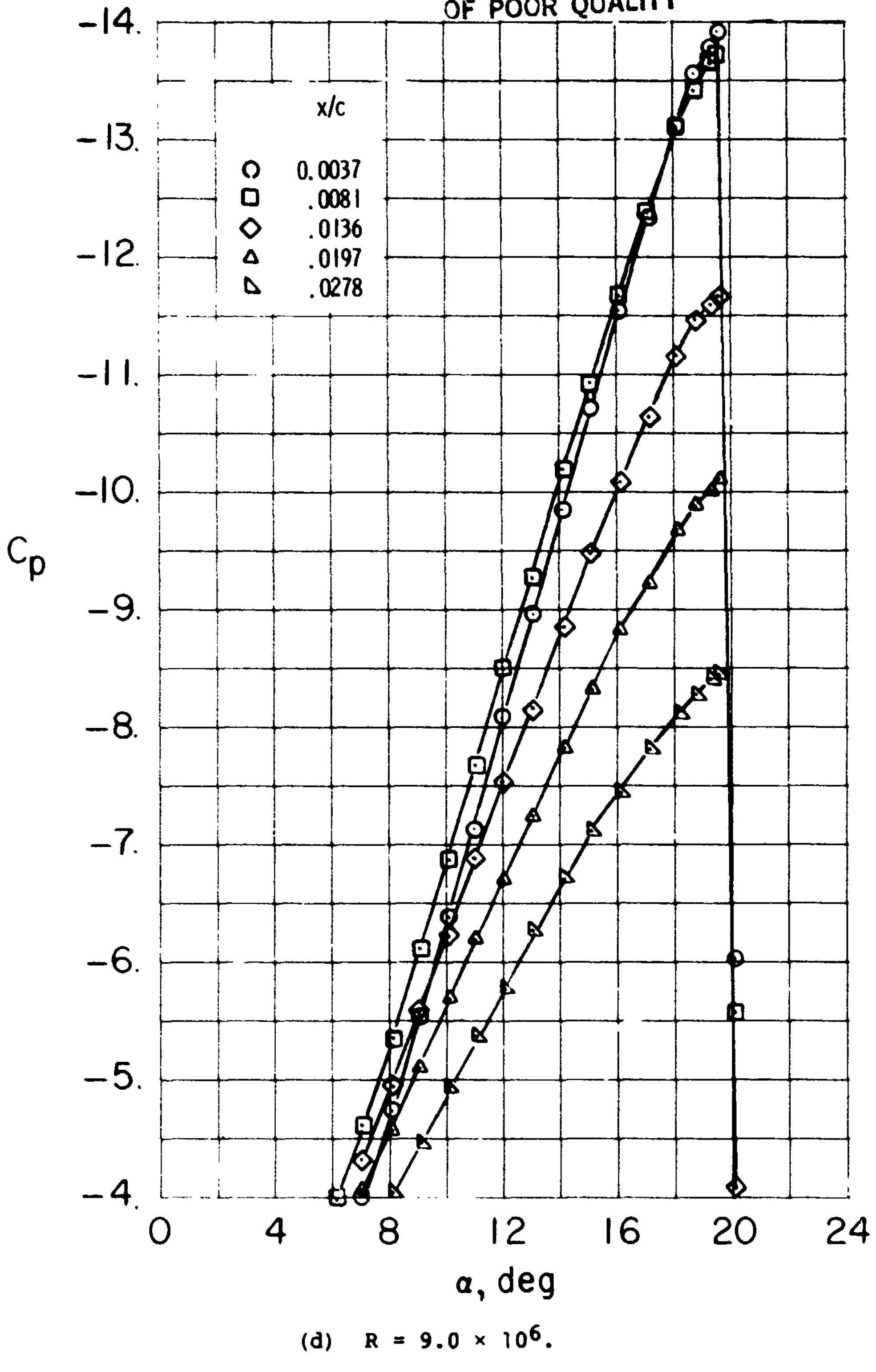

(d) R = 9.0 × 10^6.

Figure 10.- Continued.

ORIGINAL PAGE IS
OF POOR QUALITY

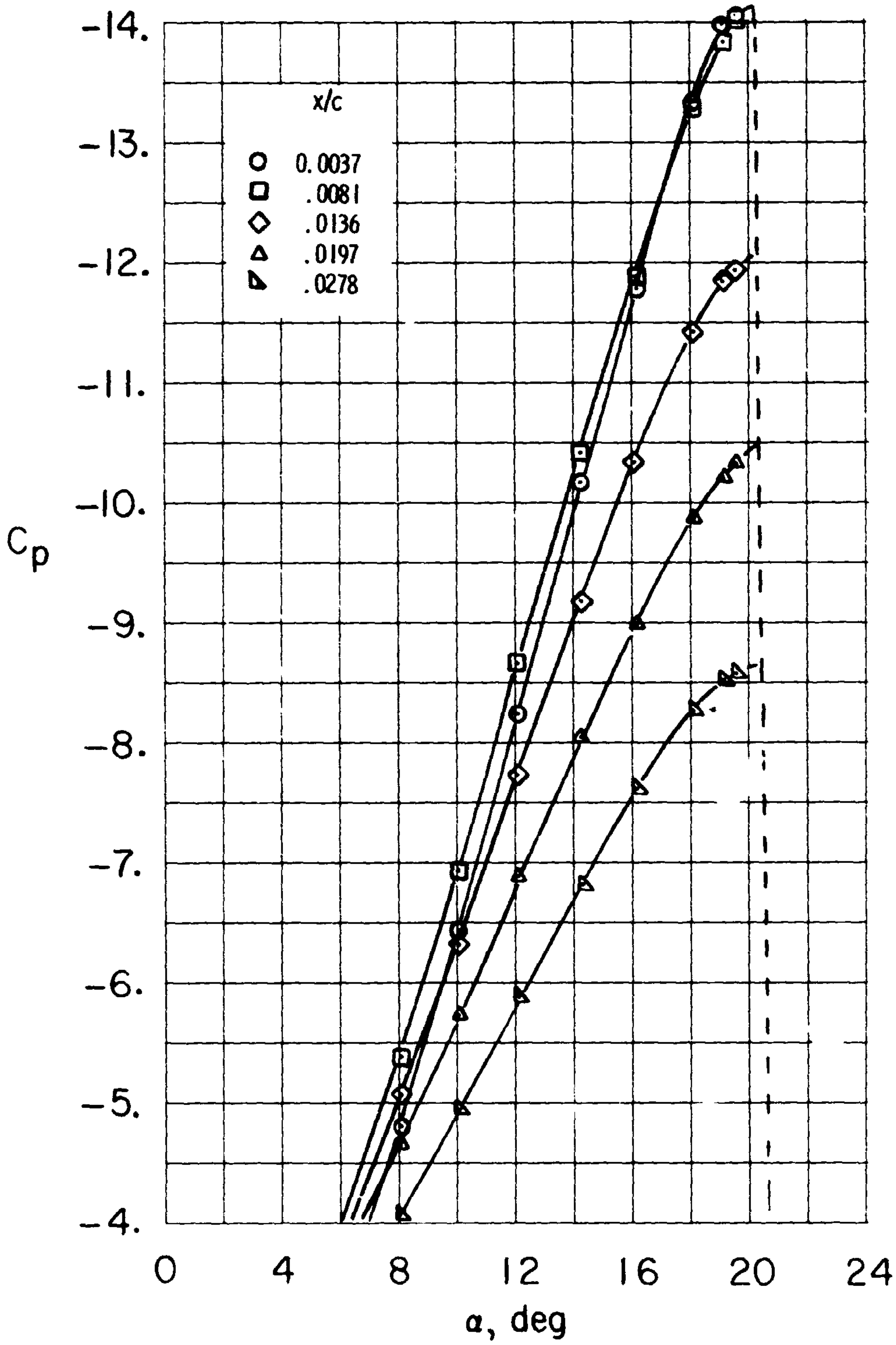

(e) $R = 12.0 \times 10^6$.

Figure 10.- Continued.

ORIGINAL PAGE IS
OF POOR QUALITY

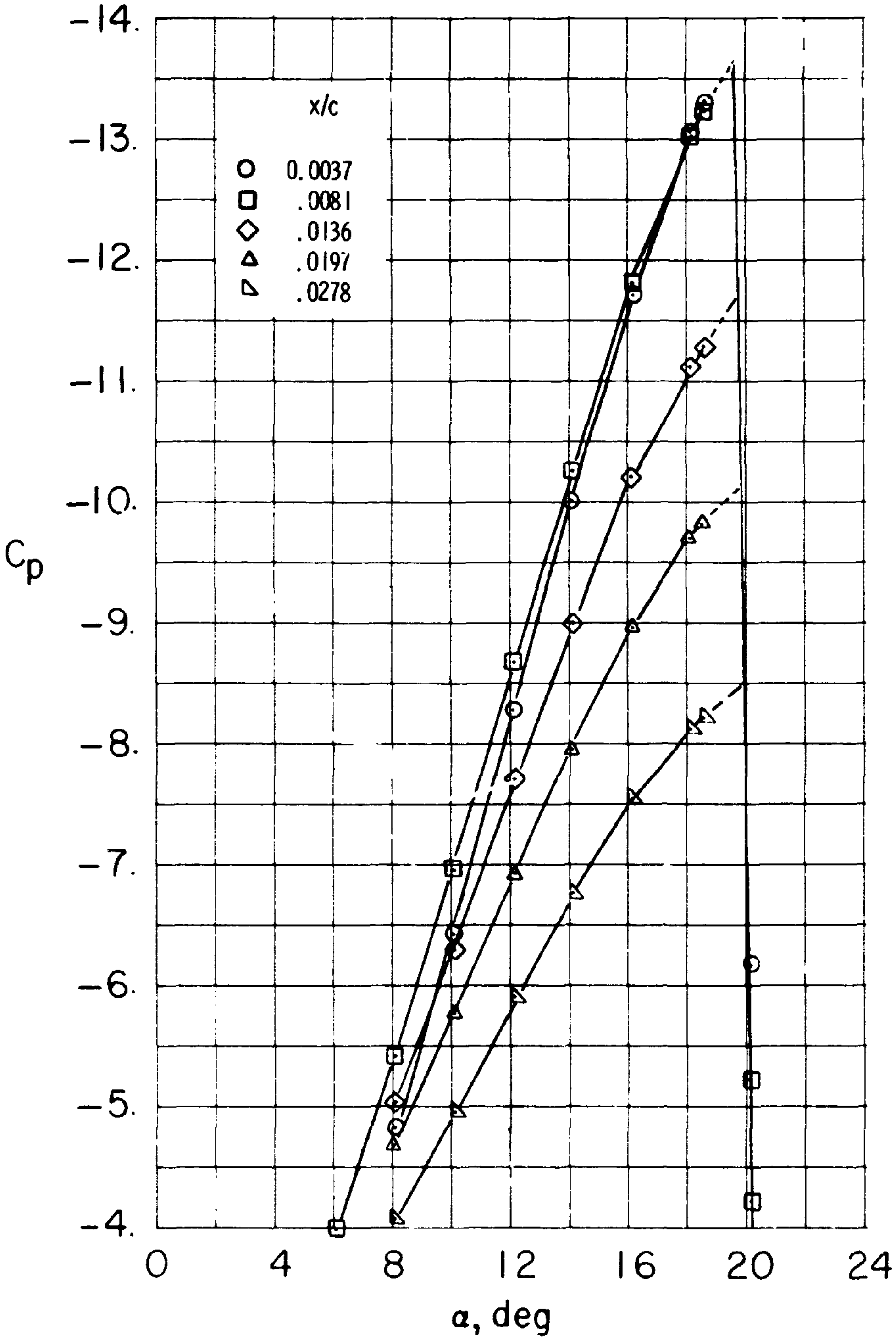

(f) $R = 18.0 \times 10^6$.

Figure 10.- Concluded.

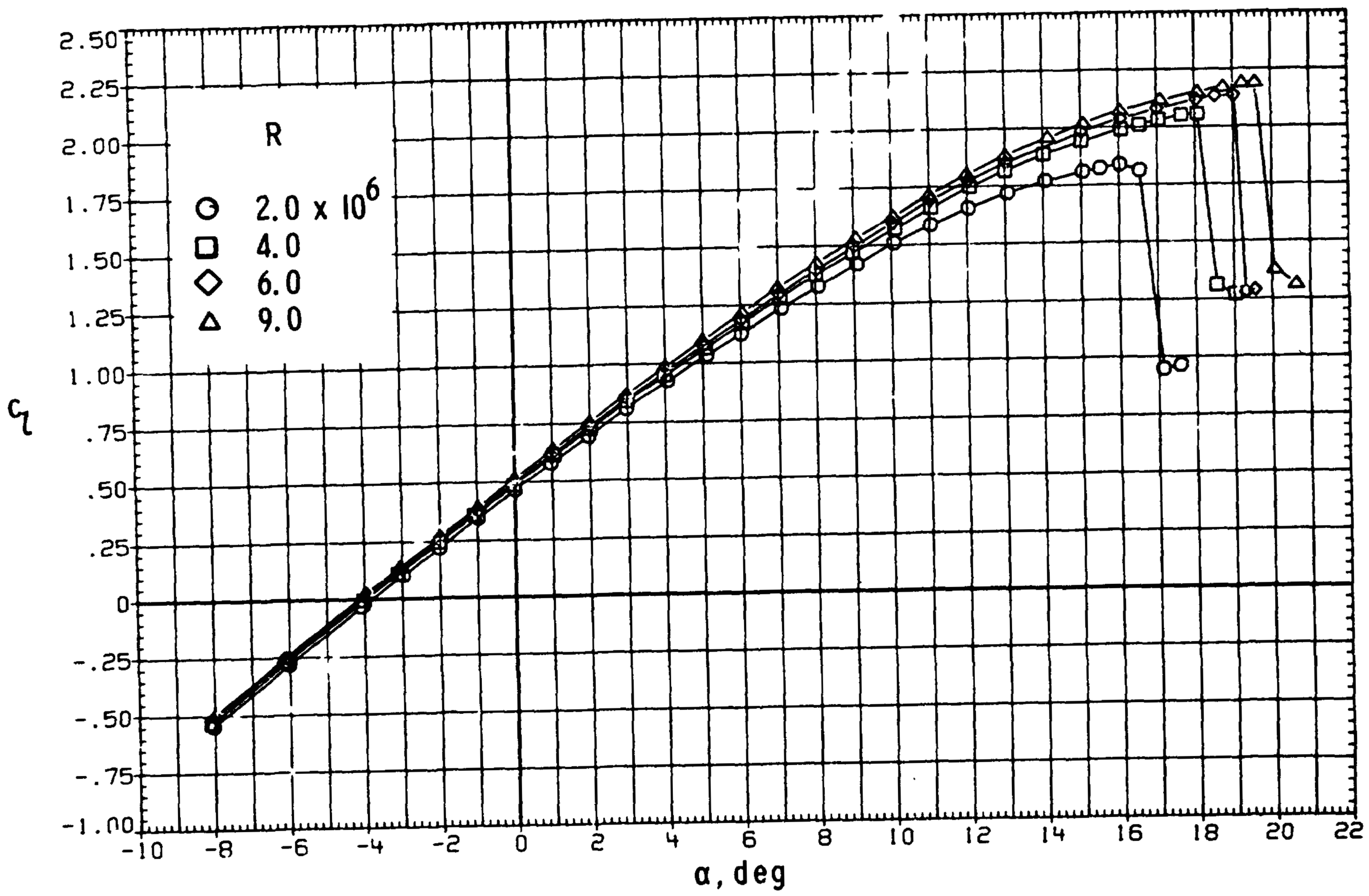

(a) c_l versus α.

Figure 11.- Effect of Reynolds number on section characteristics; M = 0.15, transition fixed.

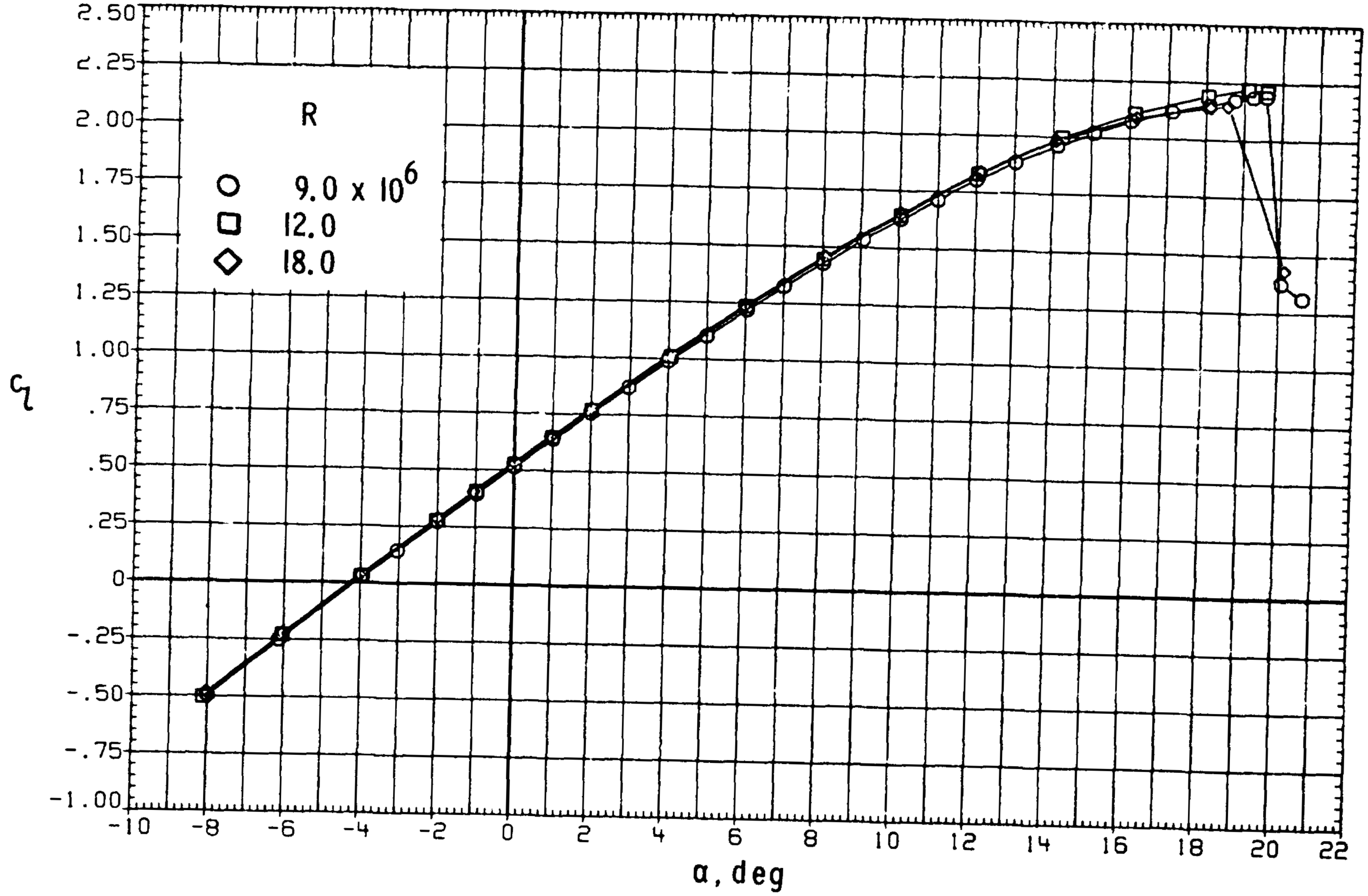

(a) Concluded.

Figure 11.- Continued.

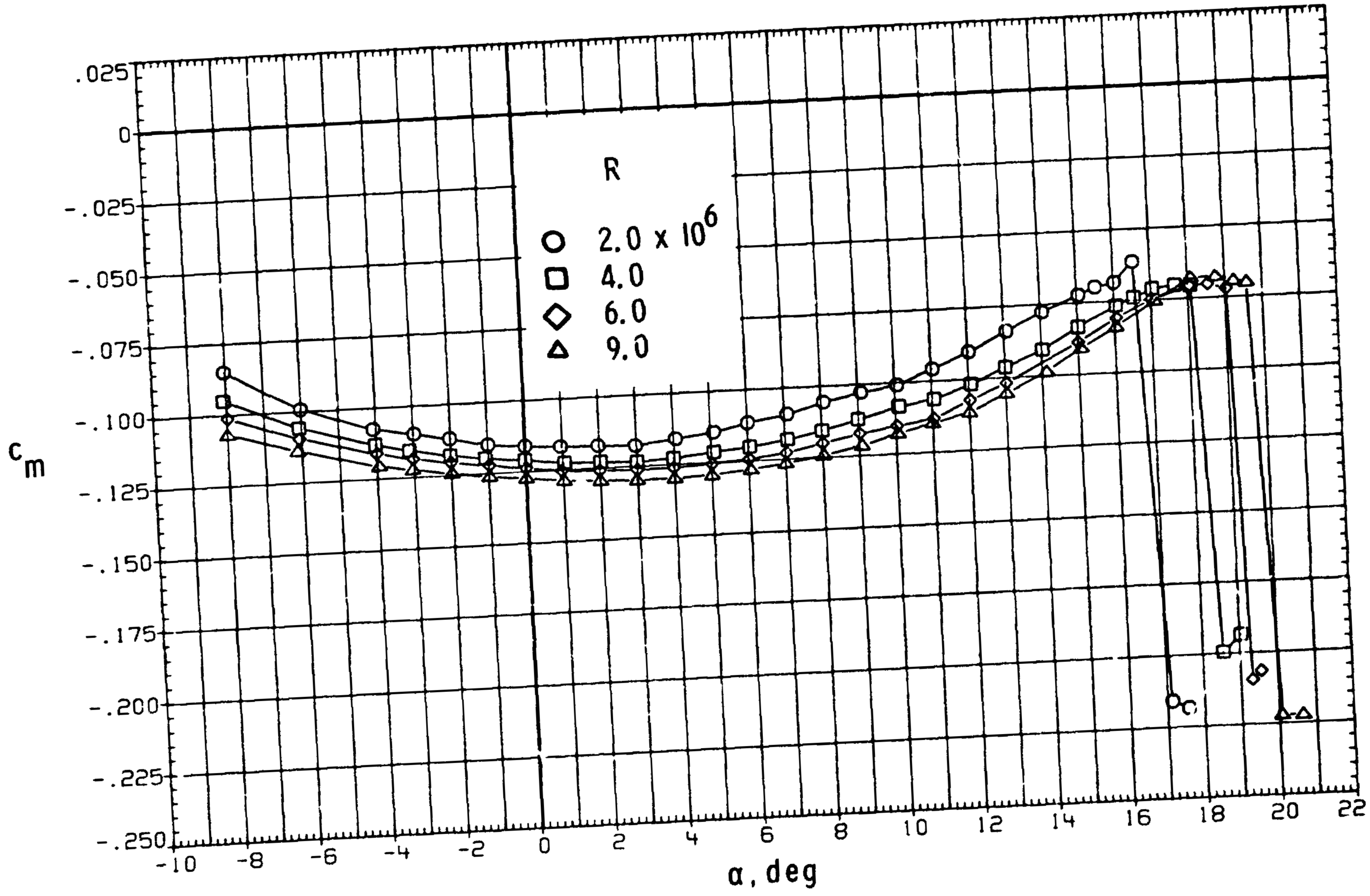

(b) c_m versus α.

Figure 11.- Continued.

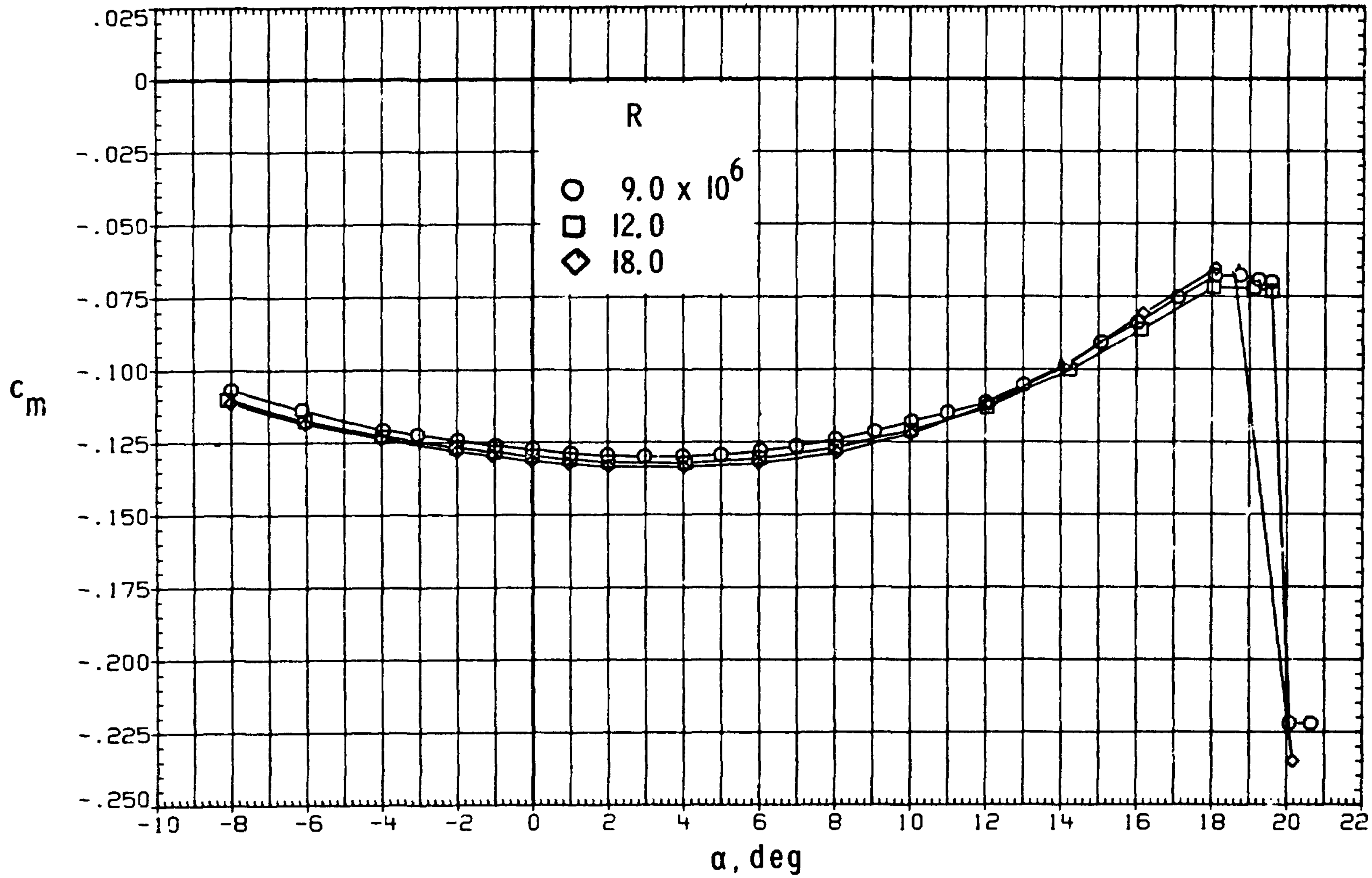

(b) Concluded.

Figure 11.- Continued.

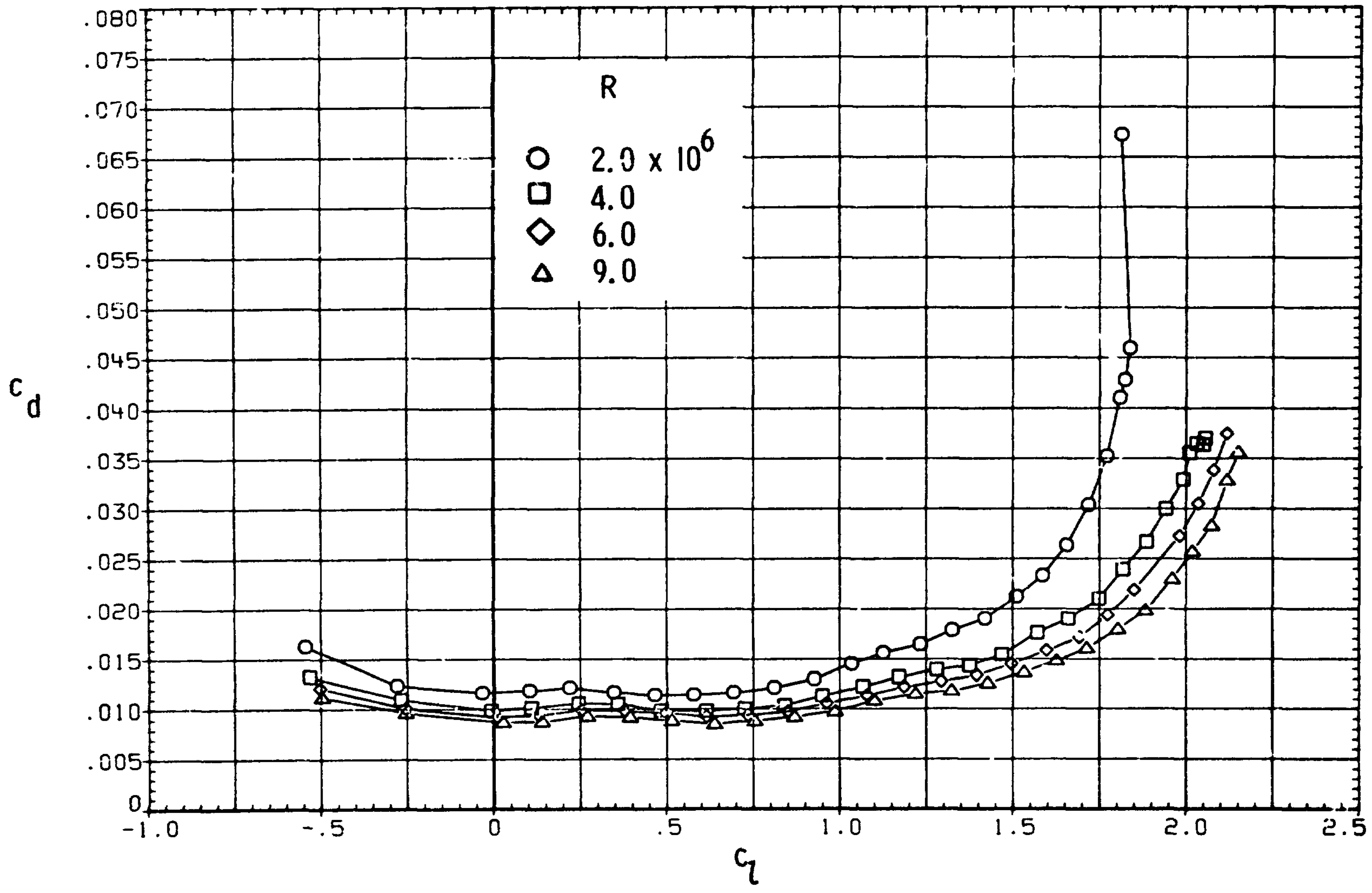

(c) c_d versus c_l.

Figure 11.- Continued.

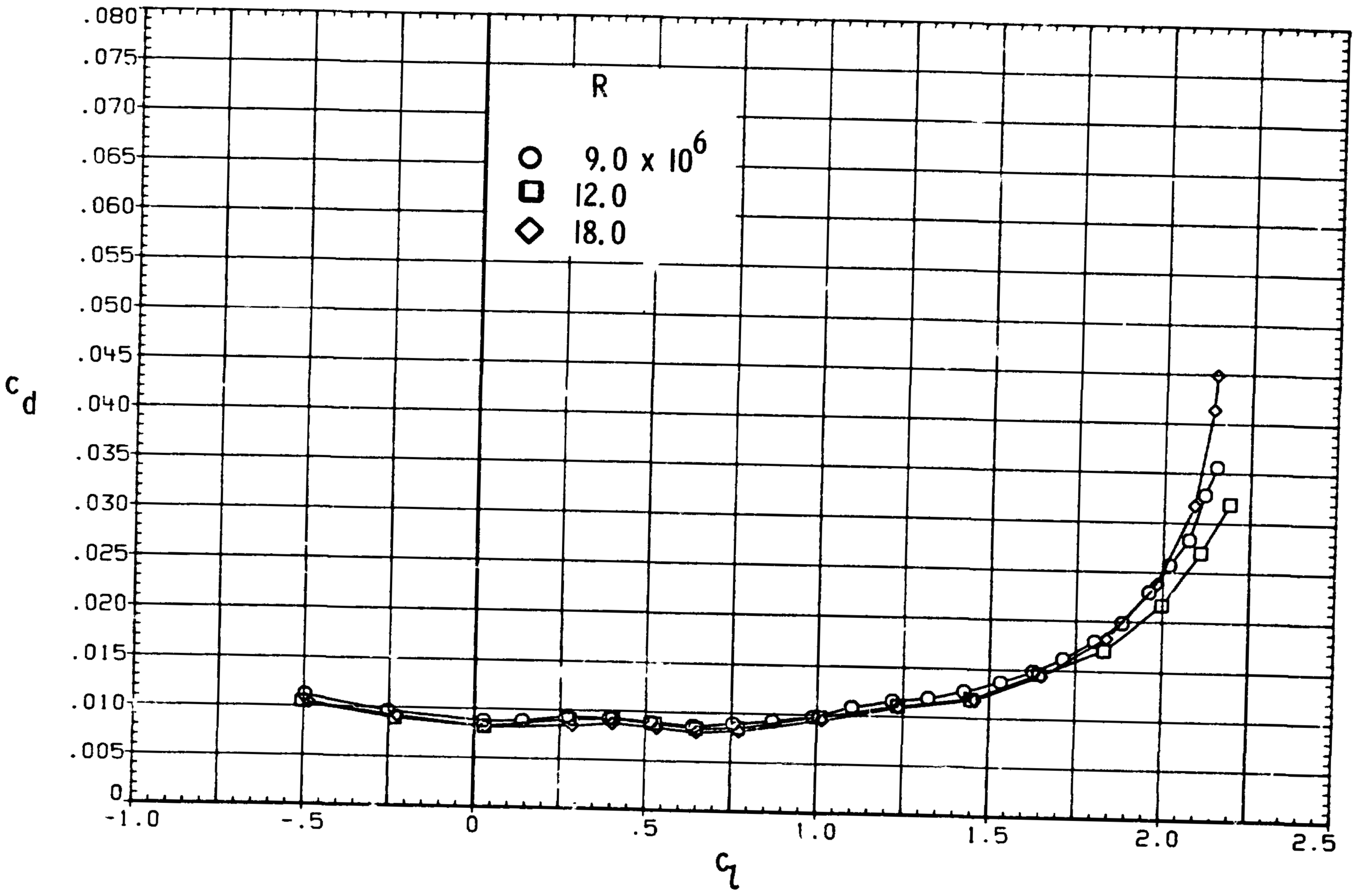

(c) Concluded.

Figure 11.- Continued.

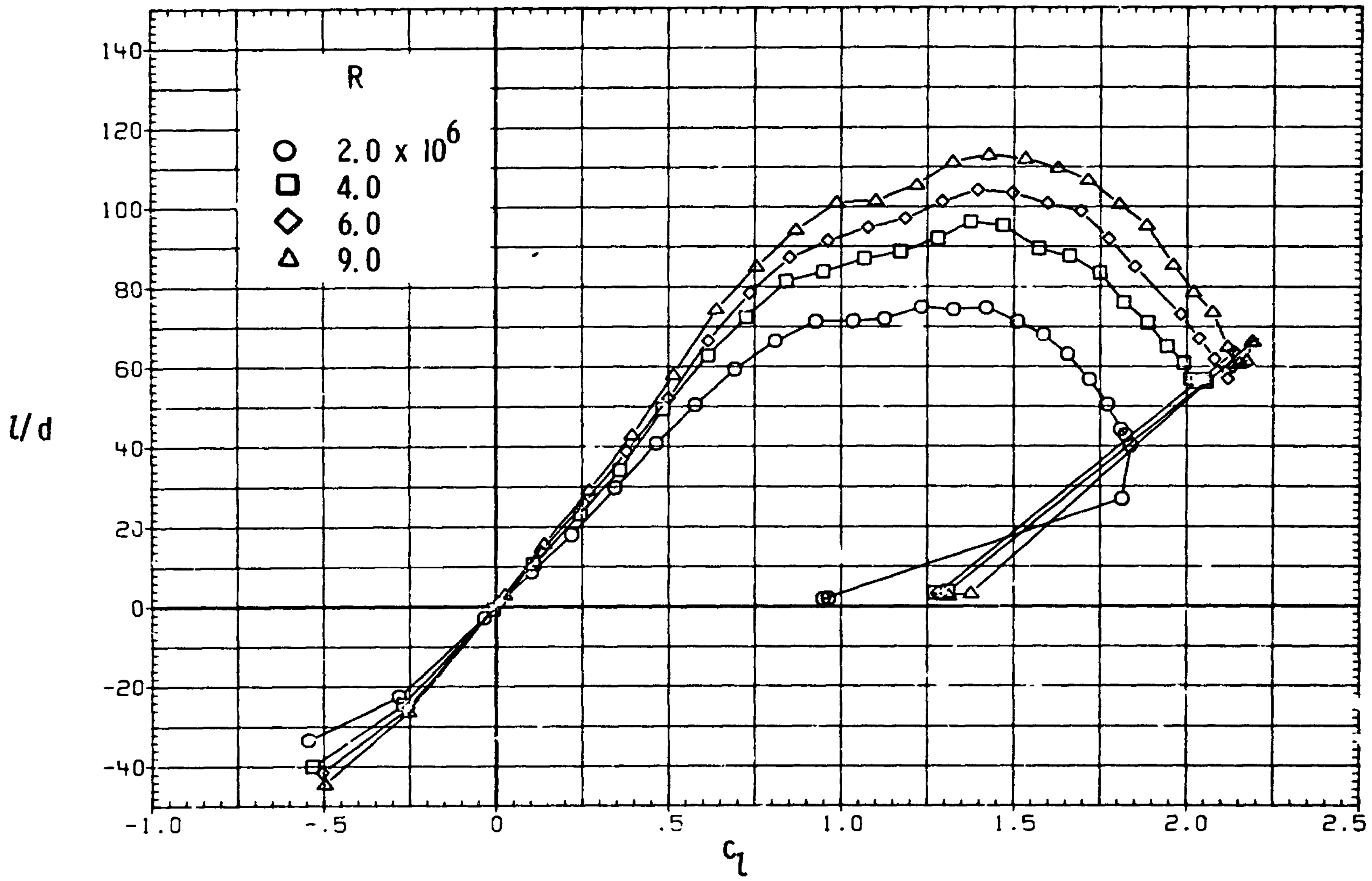

(d) l/d versus c_l.

Figure 11.- Continued.

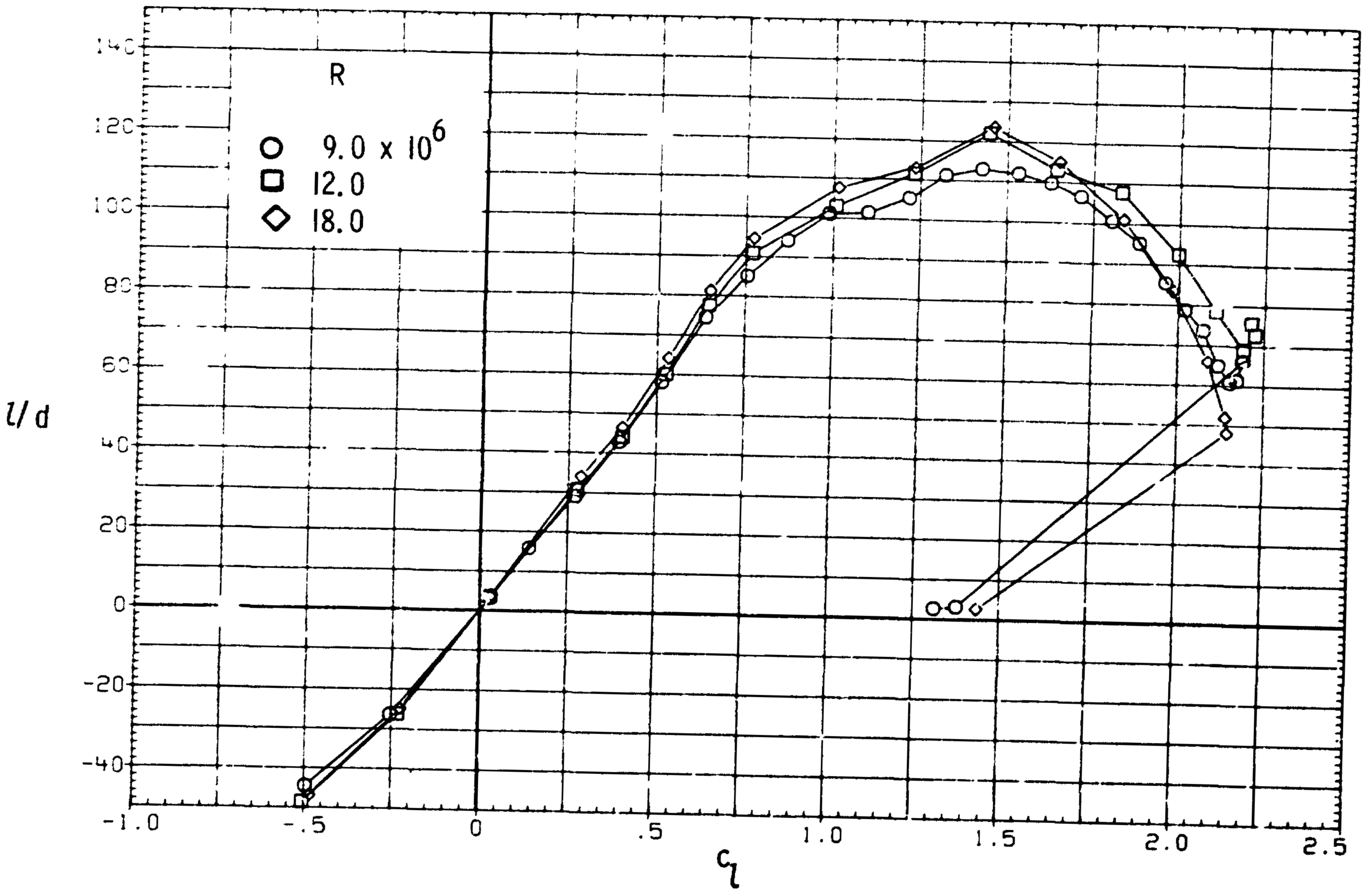

(d) Concluded.

Figure 11.- Concluded.

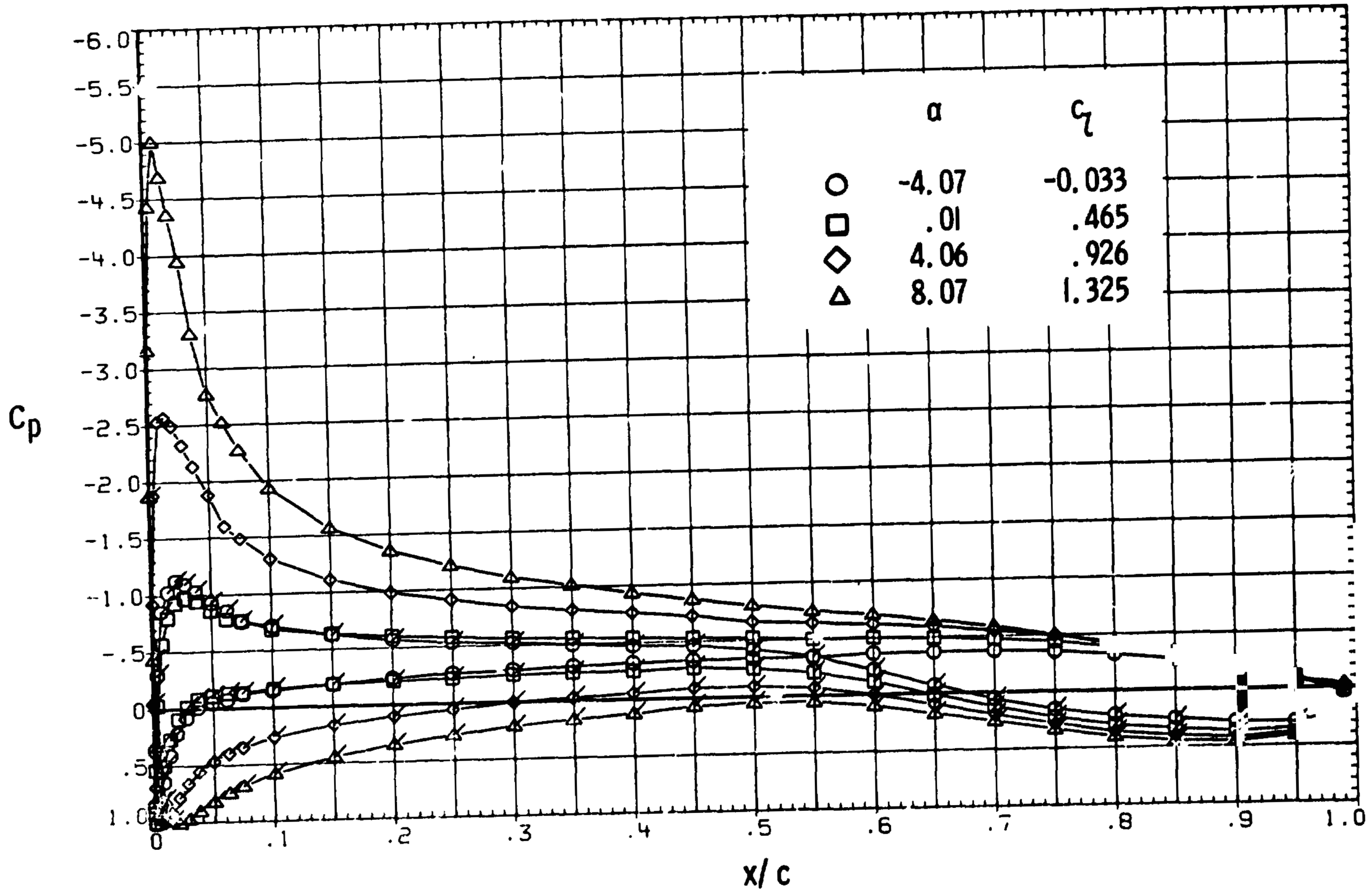

(a) R = 2.0 × 10^6.

Figure 12.- Effect of angle of attack and Reynolds number on chordwise pressure distribution; M = 0.15, transition fixed. (Flagged symbols indicate lower surface.)

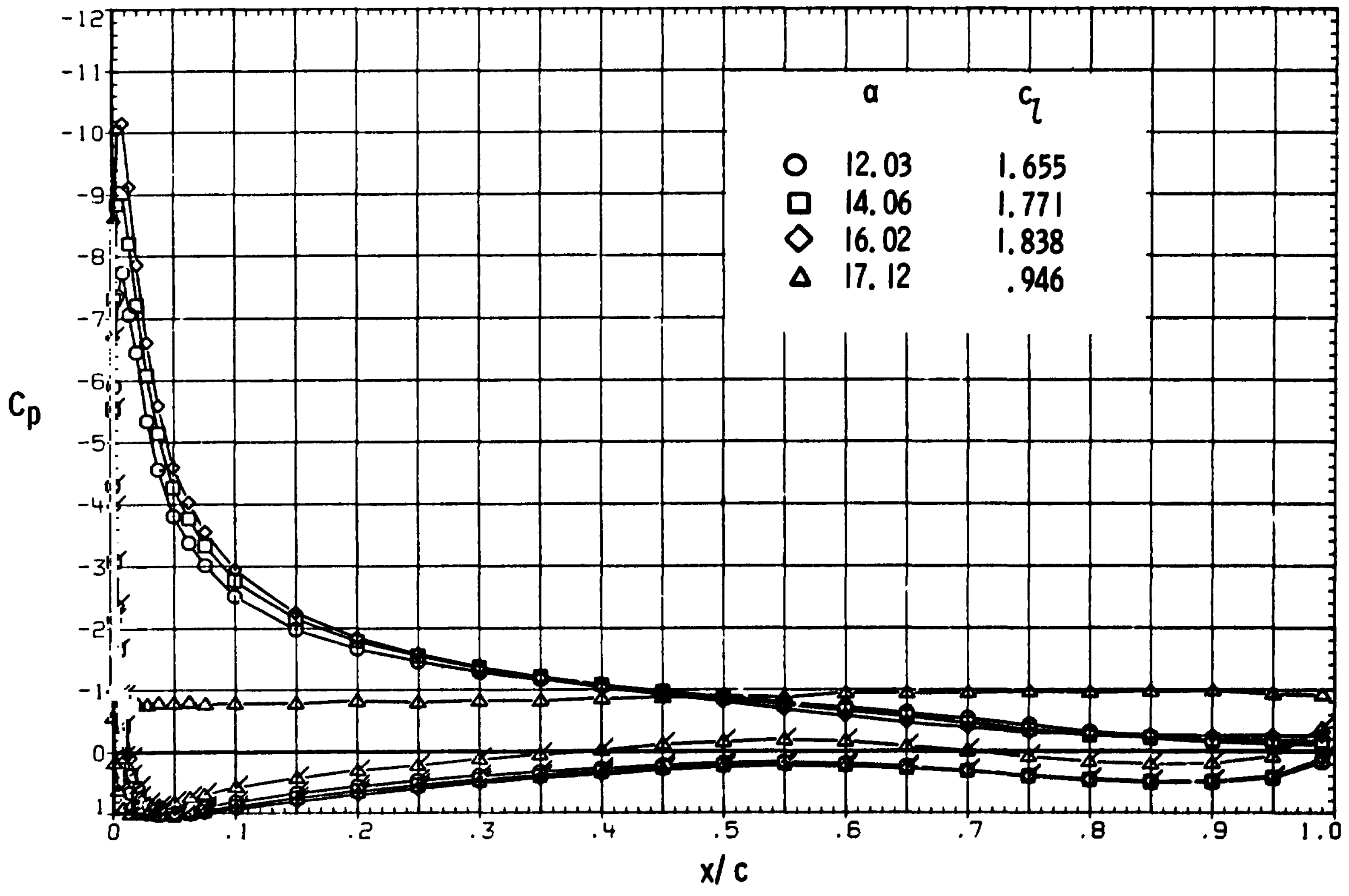

(a) Concluded.

Figure 12.- Continued.

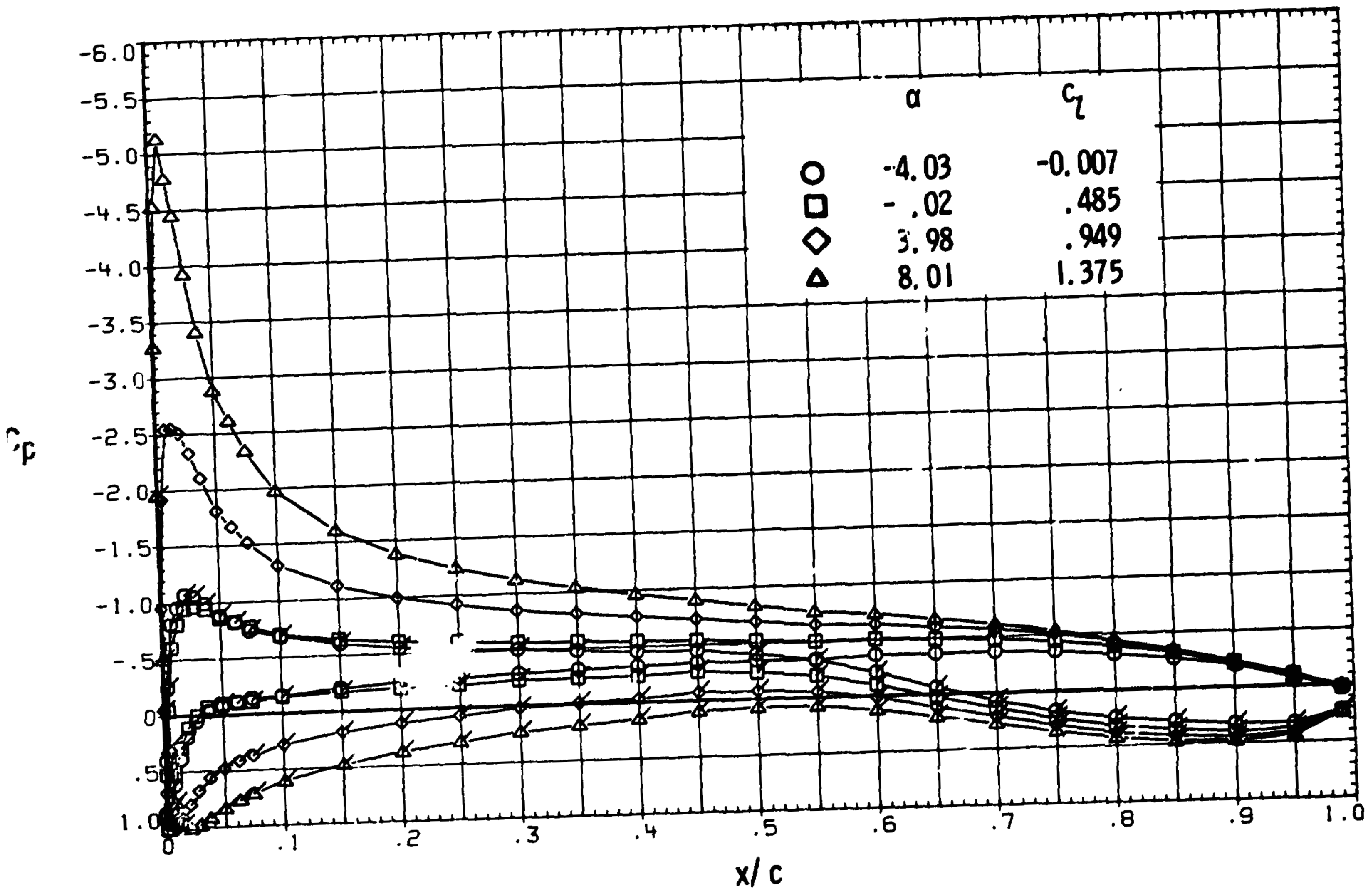

(b) R = 4.0 × 10^6.

Figure 12.- Continued.

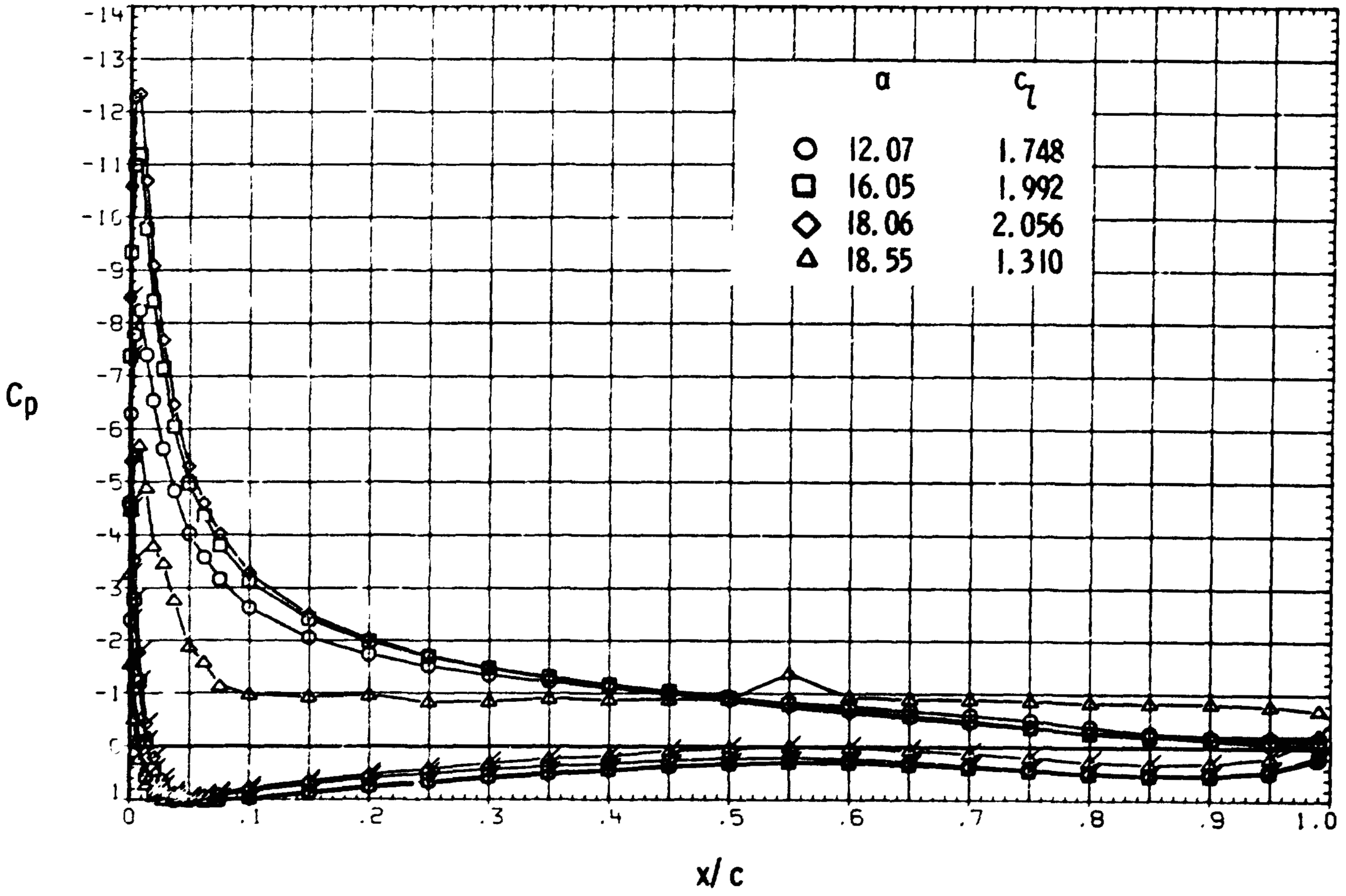

(b) Concluded.

Figure 12.- Continued.

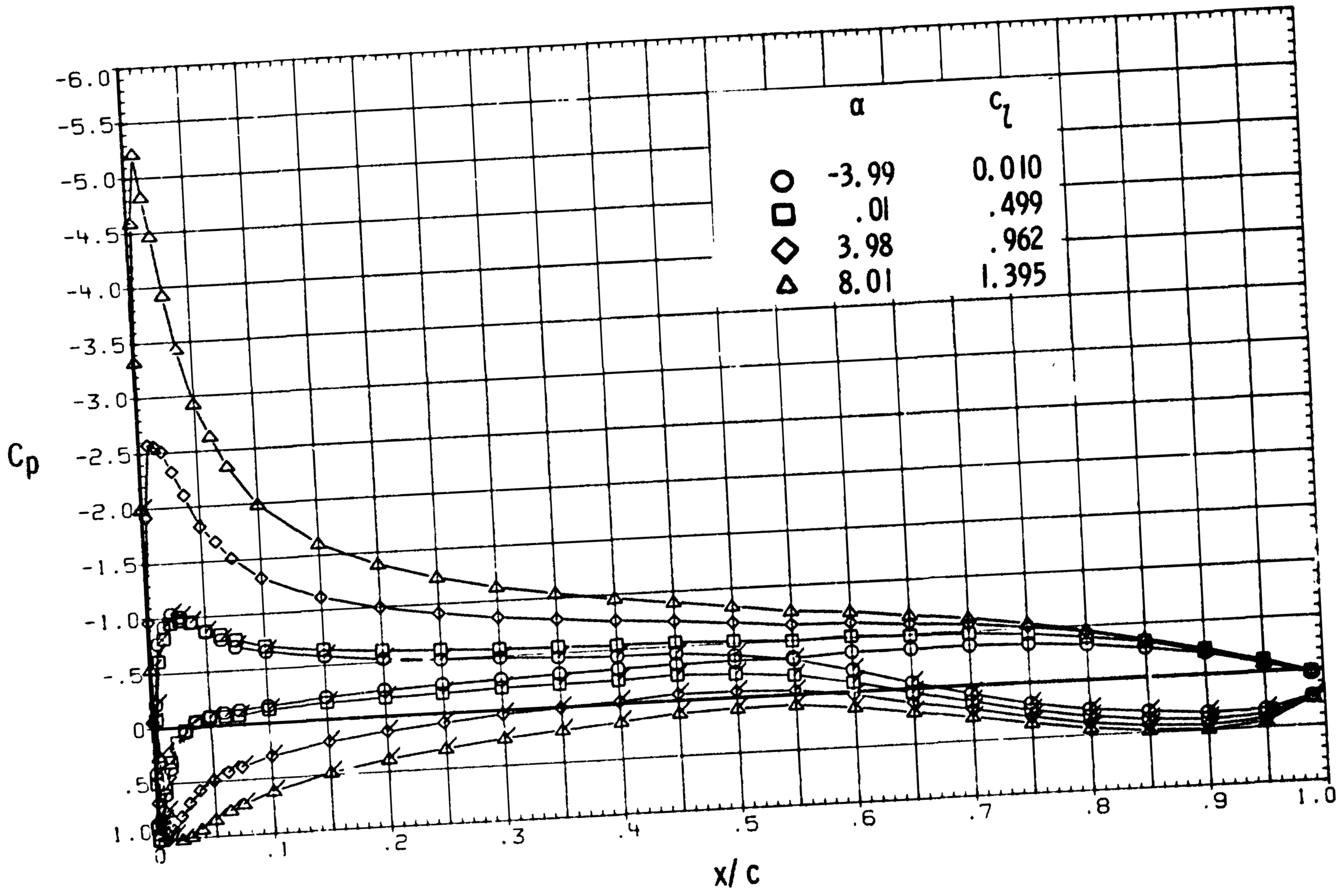

(c) R = 6.0 × 10^6.

Figure 12.- Continued.

ORIGINAL PAGE IS
OF POOR QUALITY

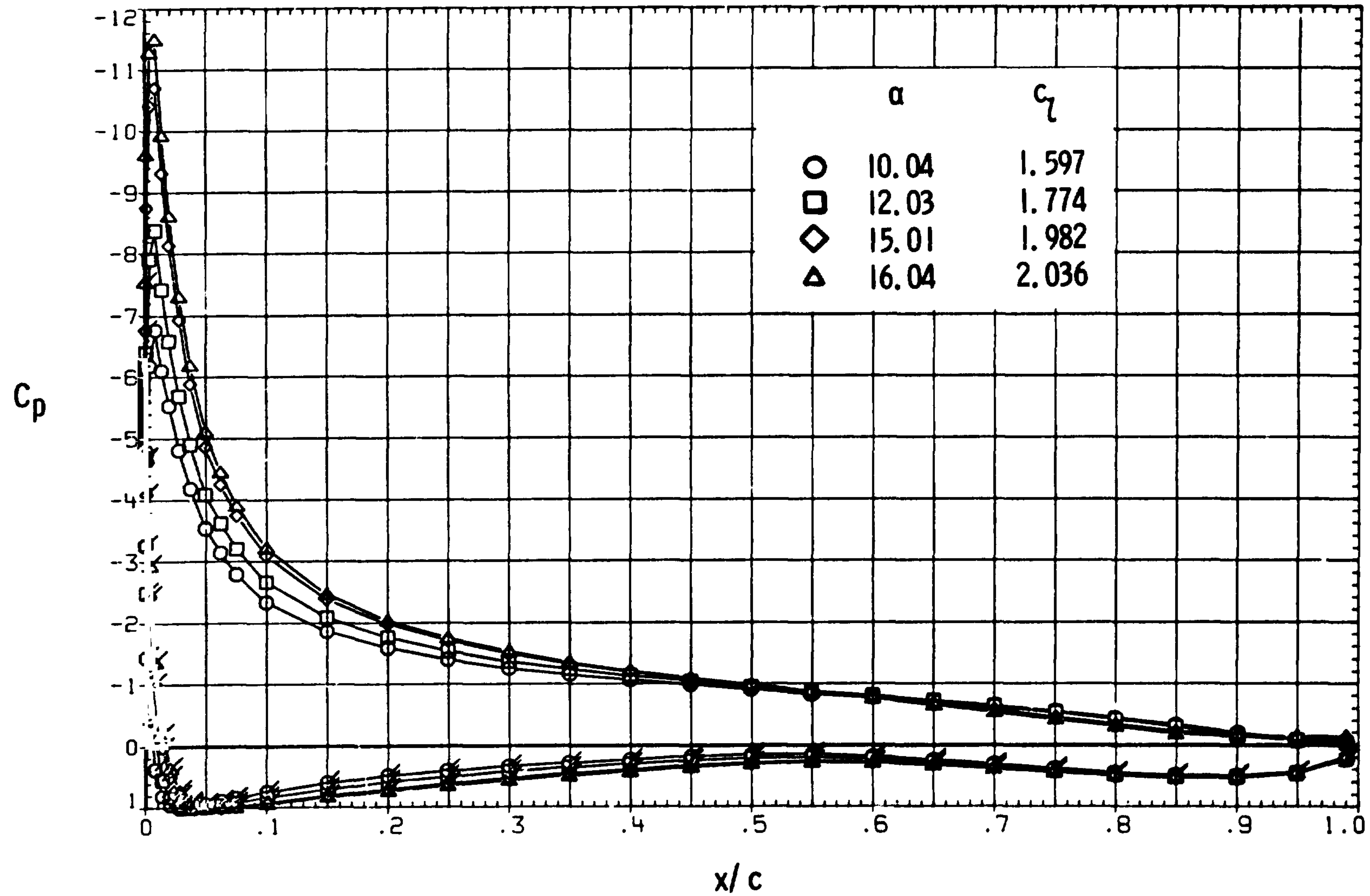

(c) Continued.

Figure 12.- Continued.

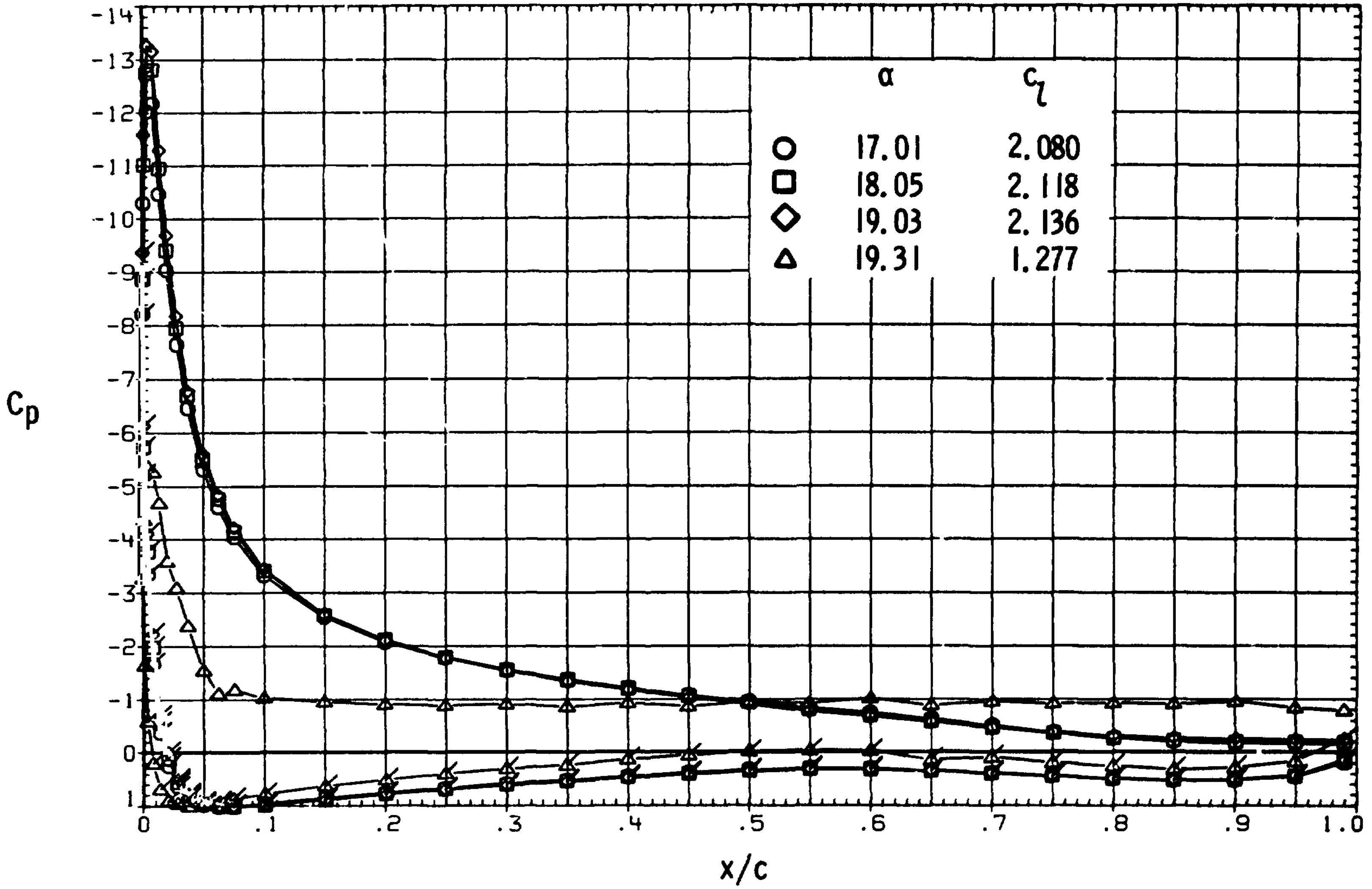

(c) Concluded.

Figure 12.- Continued.

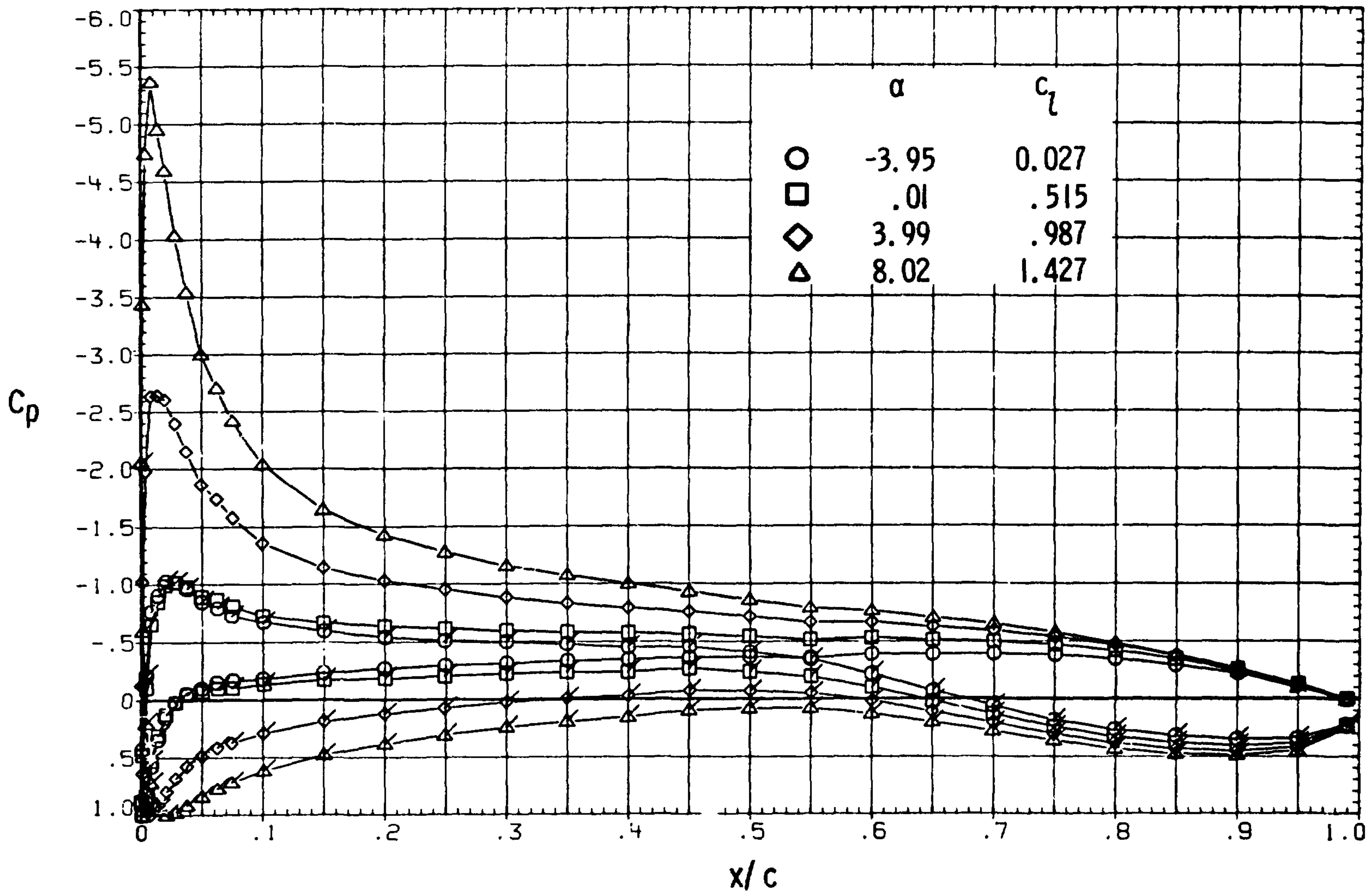

(d) R = 9.0 × 10^6.

Figure 12.- Continued.

ORIGINAL PAGE IS
OF POOR QUALITY

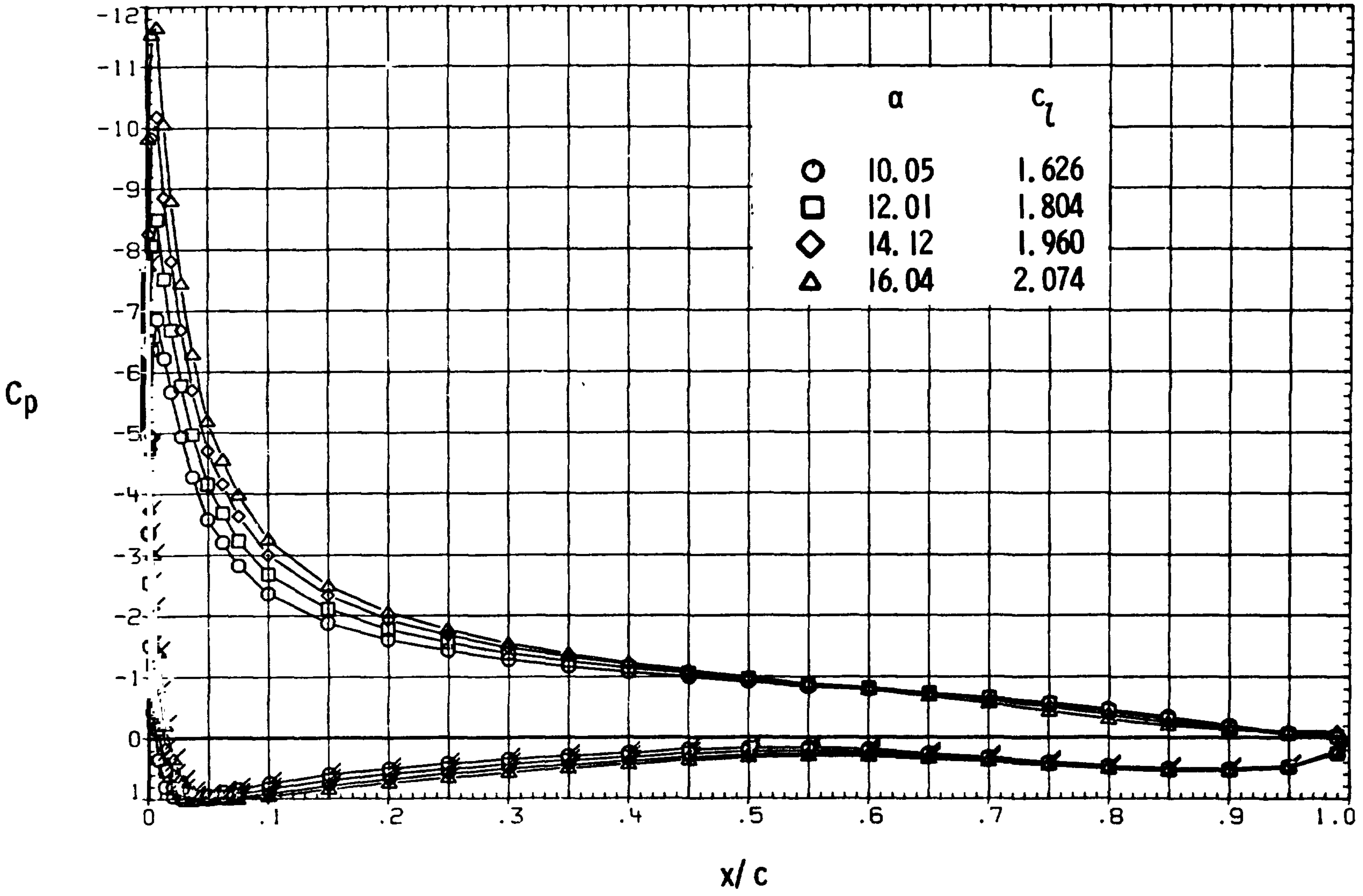

(d) Continued.

Figure 12.- Continued.

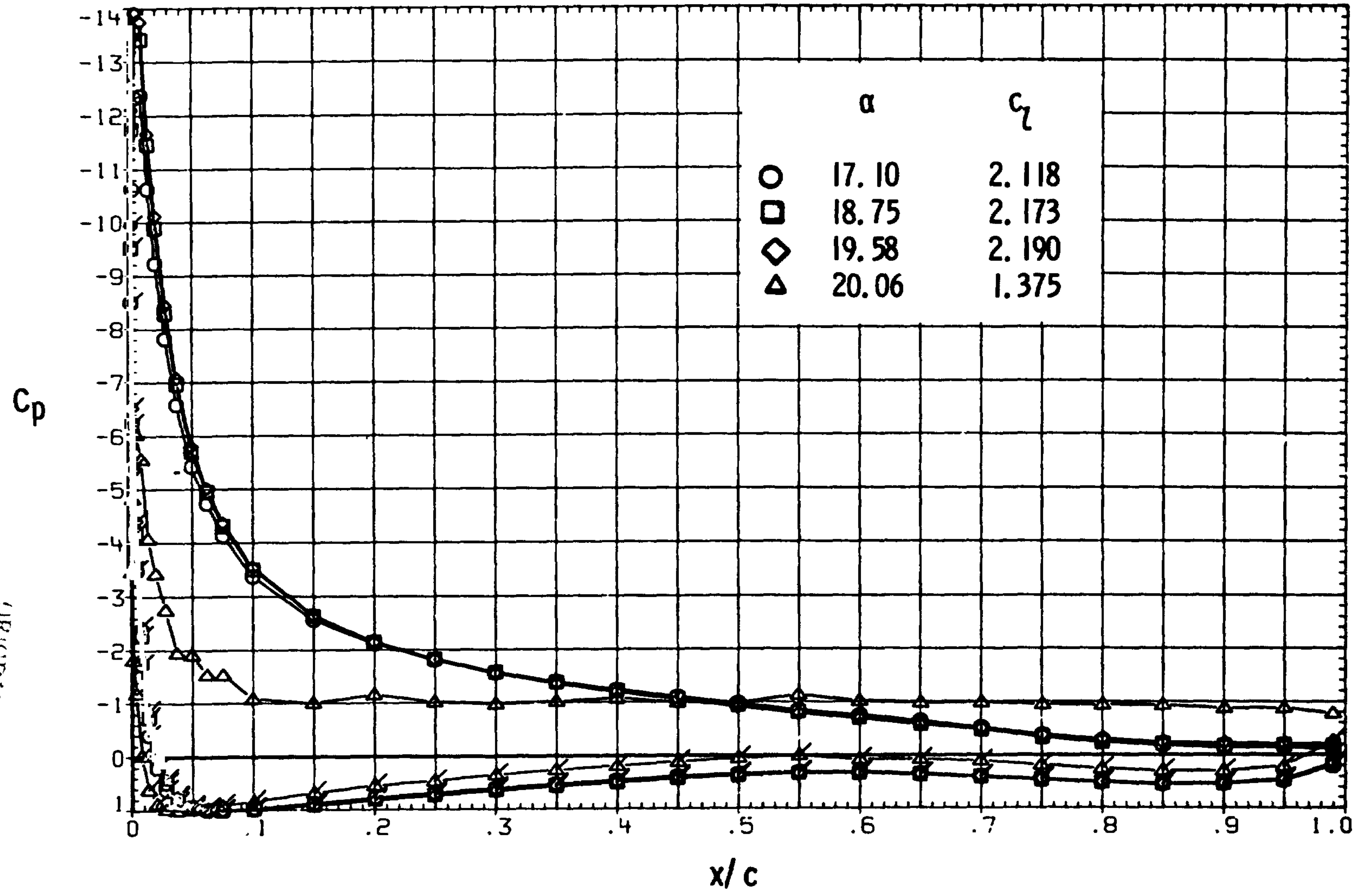

(d) Concluded.

Figure 12.- Continued.

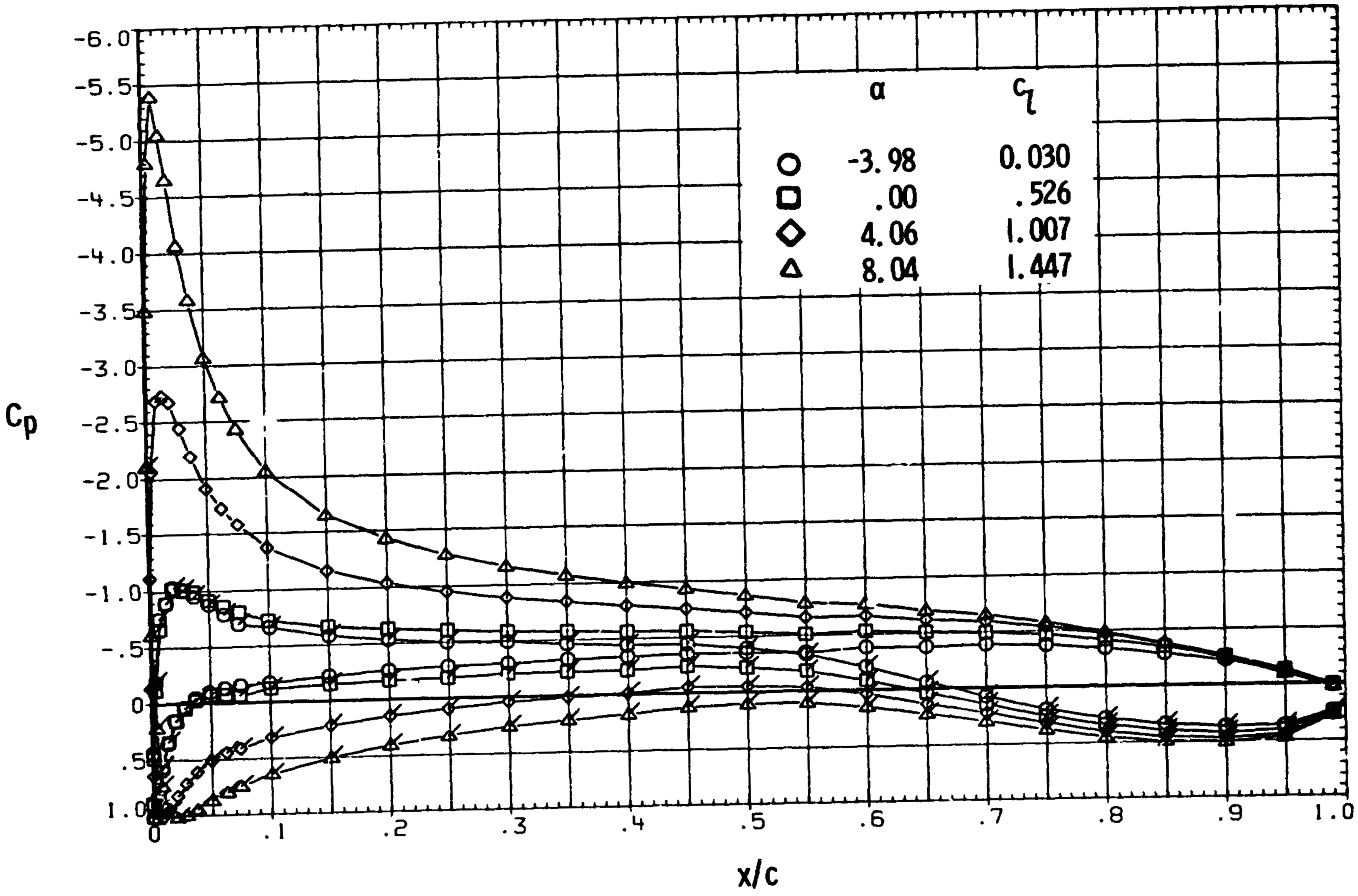

(e) $R = 12.0 \times 10^6$.

Figure 12.- Continued.

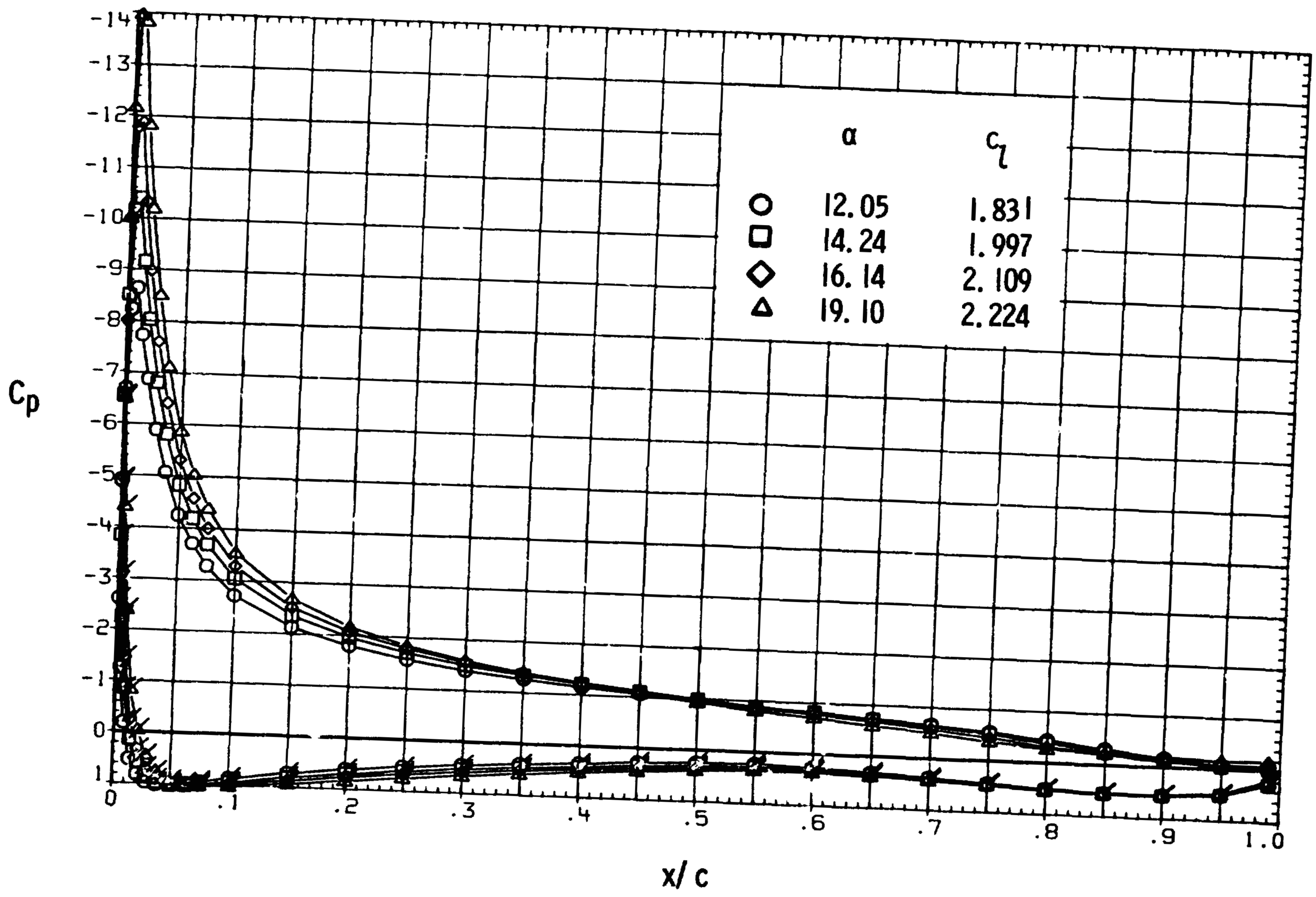

(e) Concluded.

Figure 12.- Continued.

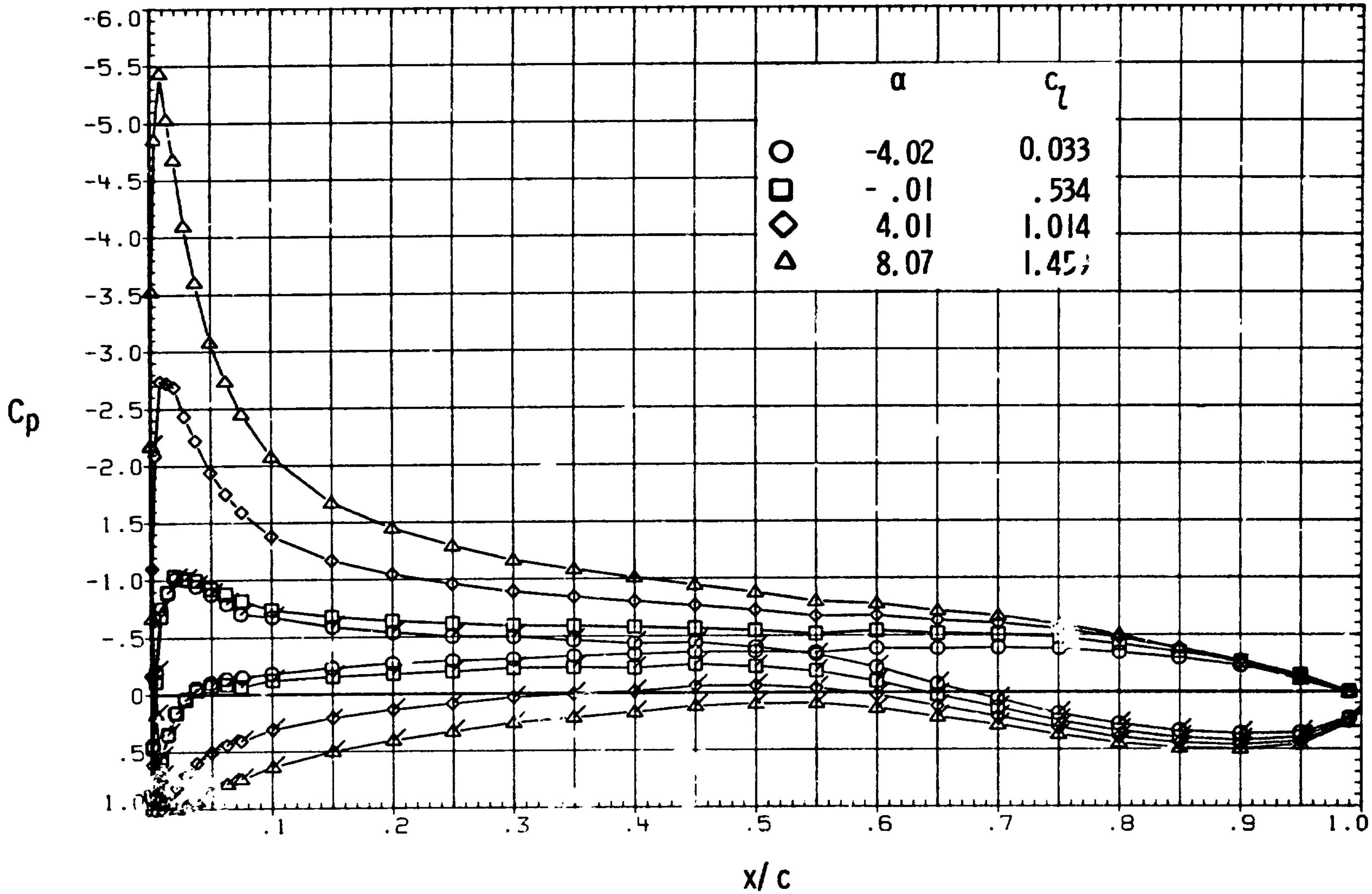

(f) R = 18.0 × 10^6.

Figure 12.- Continued.

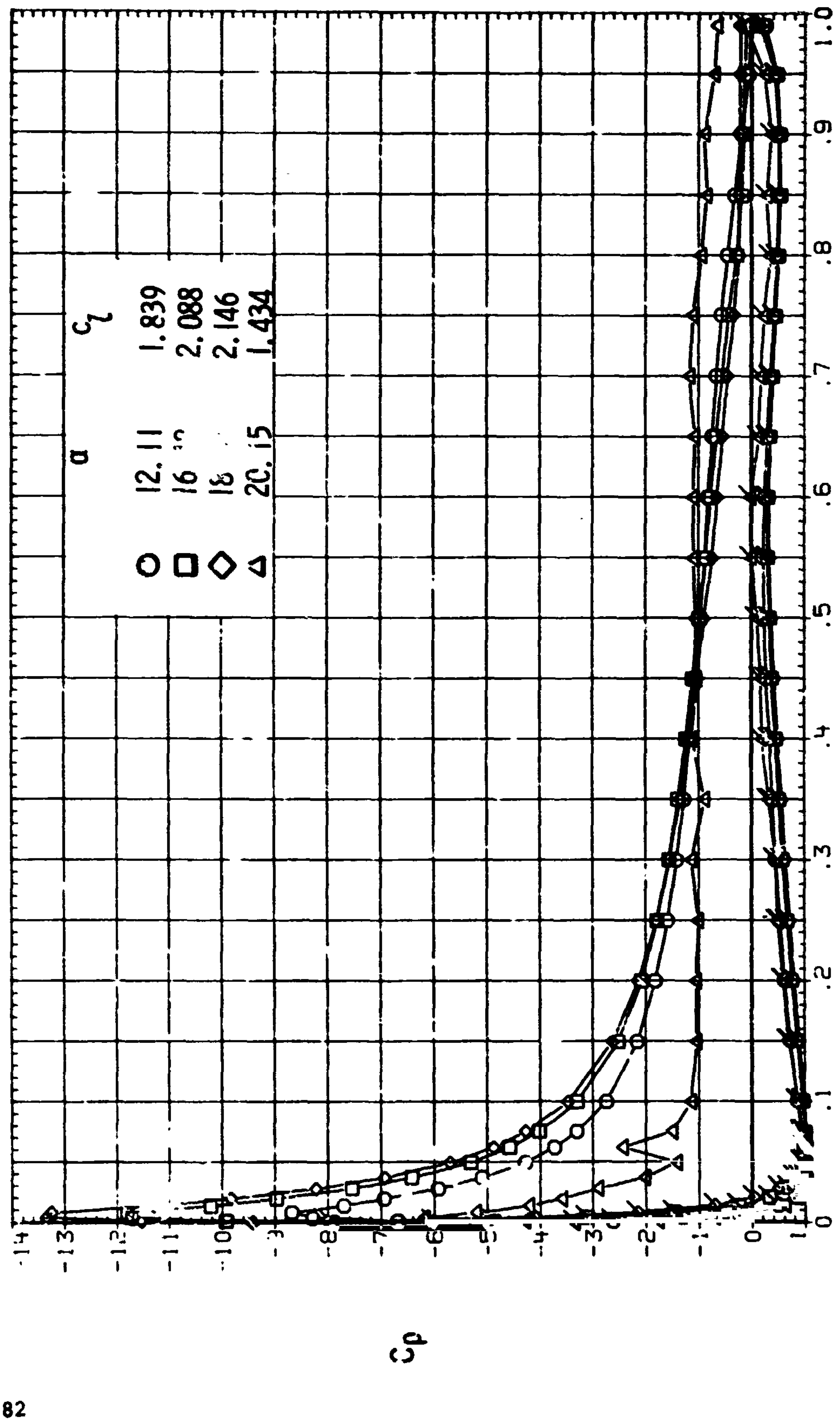

(f) Concluded.

Figure 12.- Concluded.

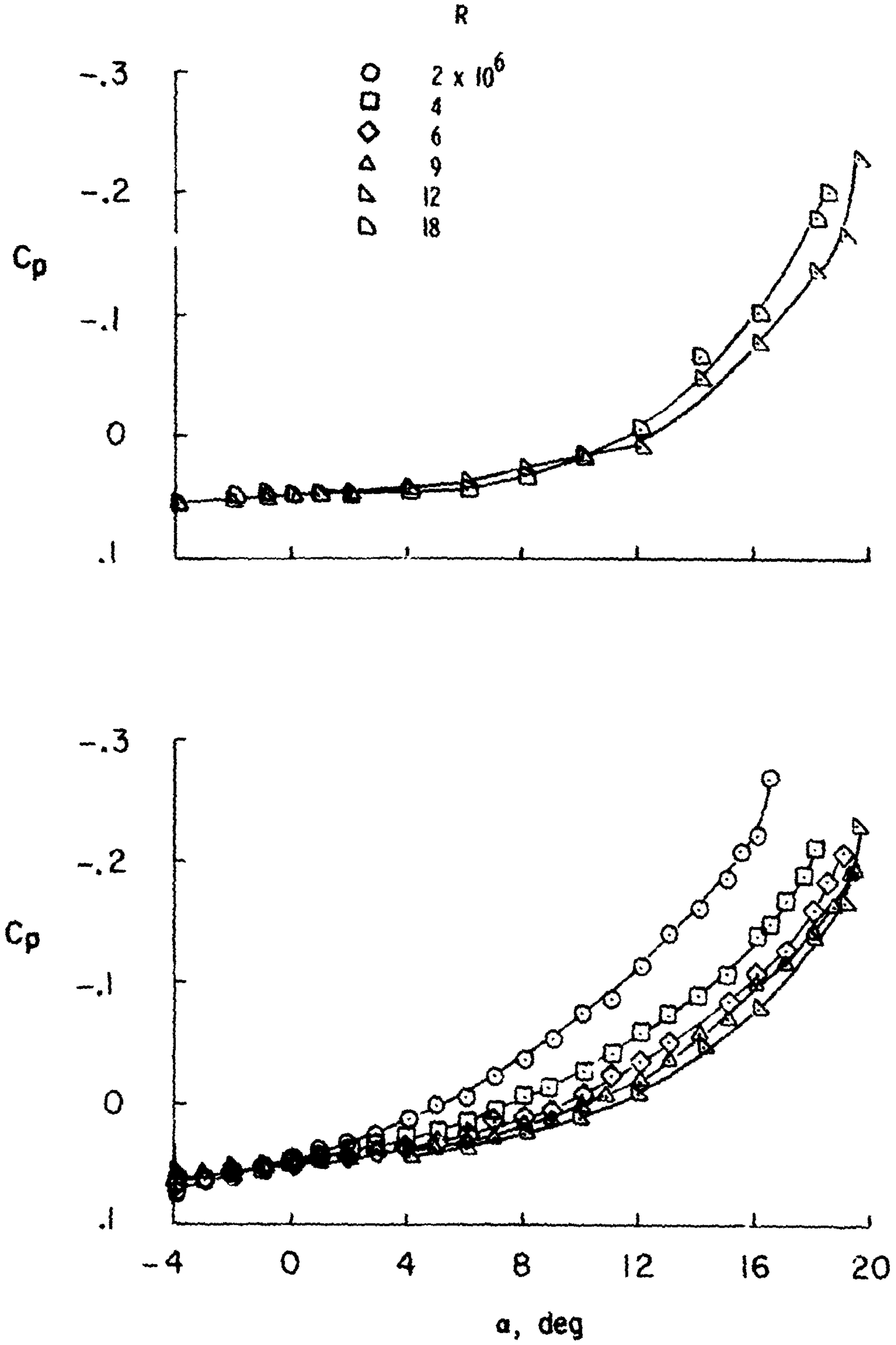

(a) Base of model.

Figure 13.- Base and upper-surface pressure coefficients; M = 0.15, transition fixed.

ORIGINAL PAGE IS
OF POOR QUALITY

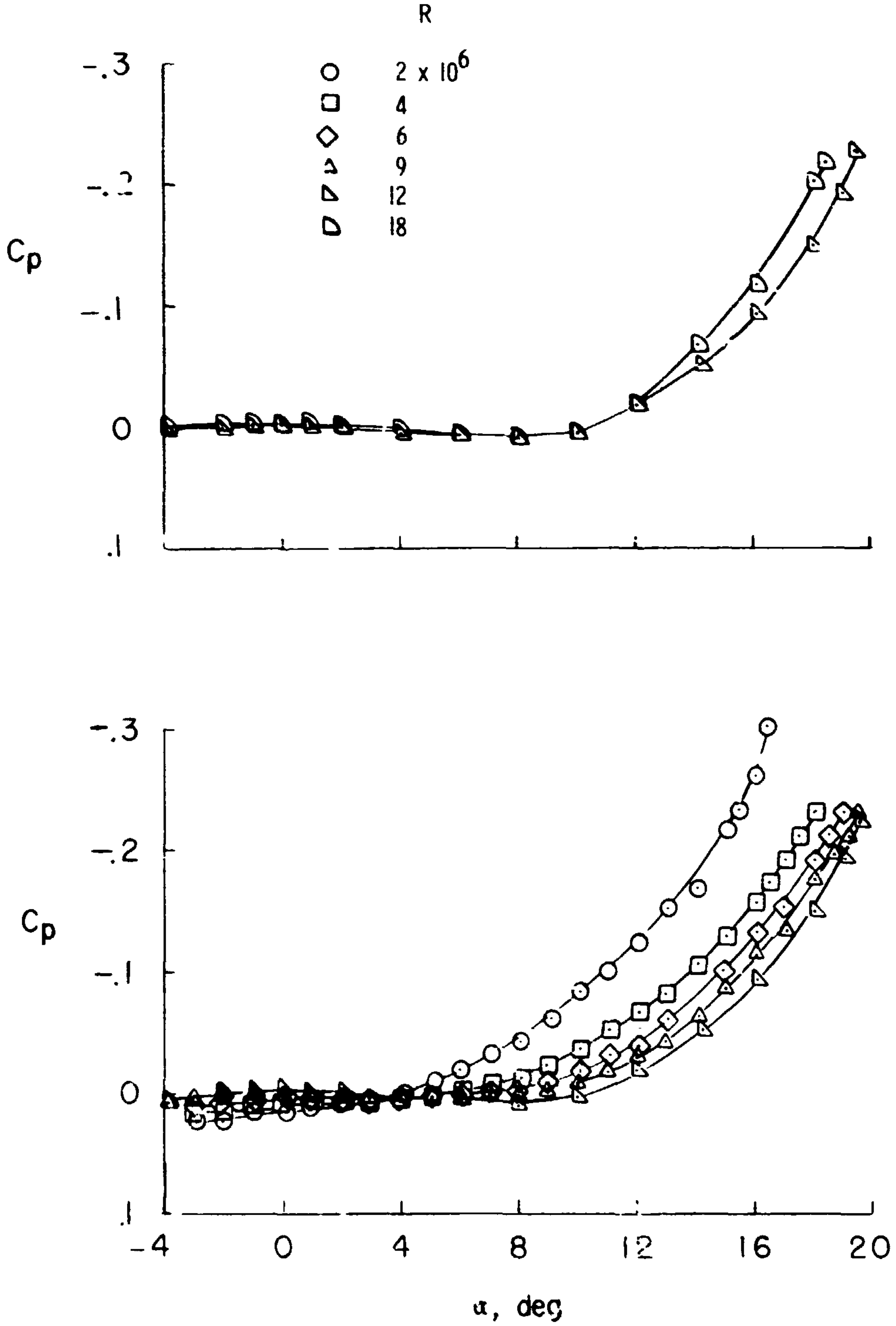

(b) Upper surface; x/c = 0.99.

Figure 13. - Continued.

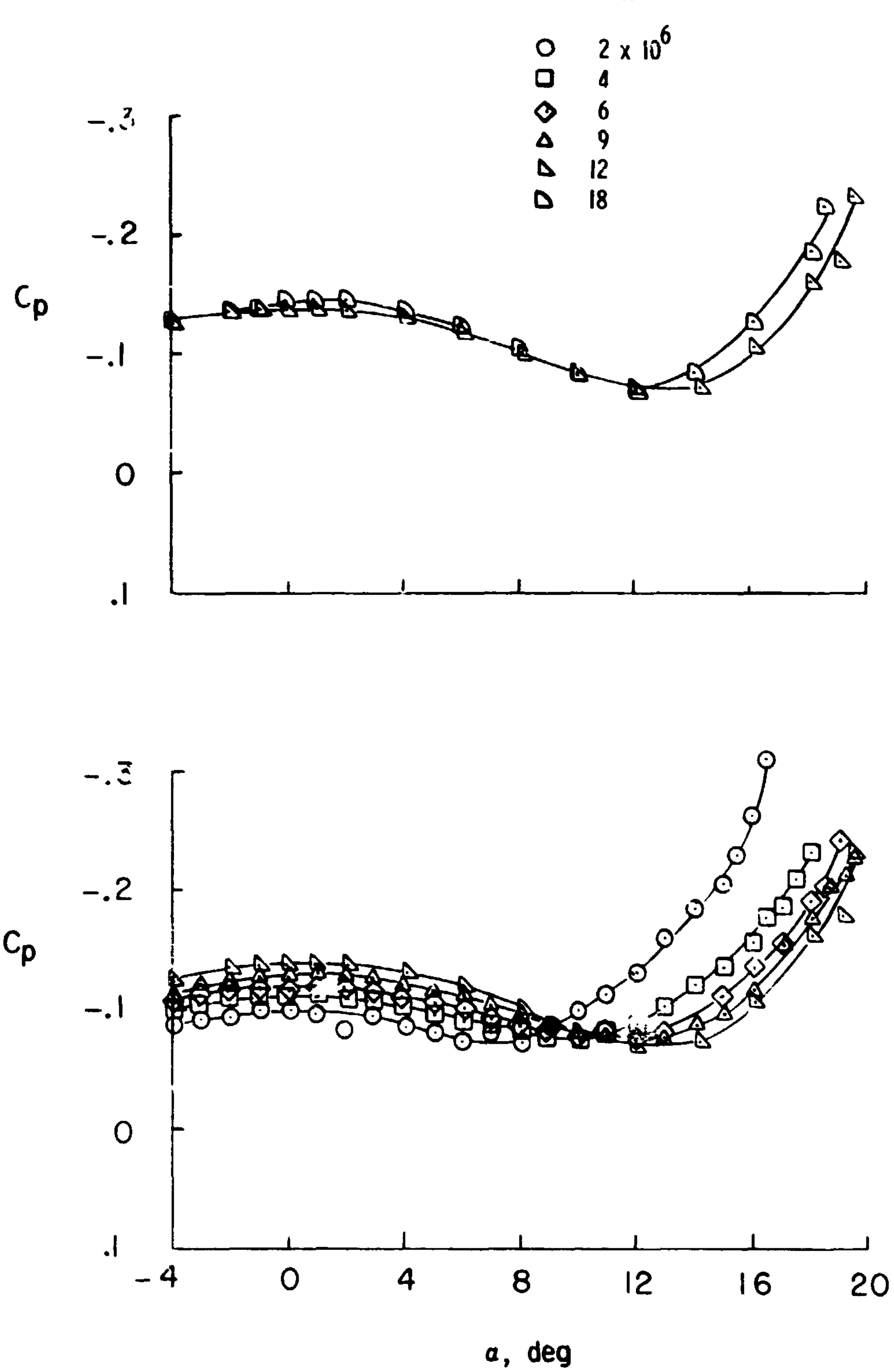

(c) Upper surface; x/c = 0.95.

Figure 13.- Concluded.

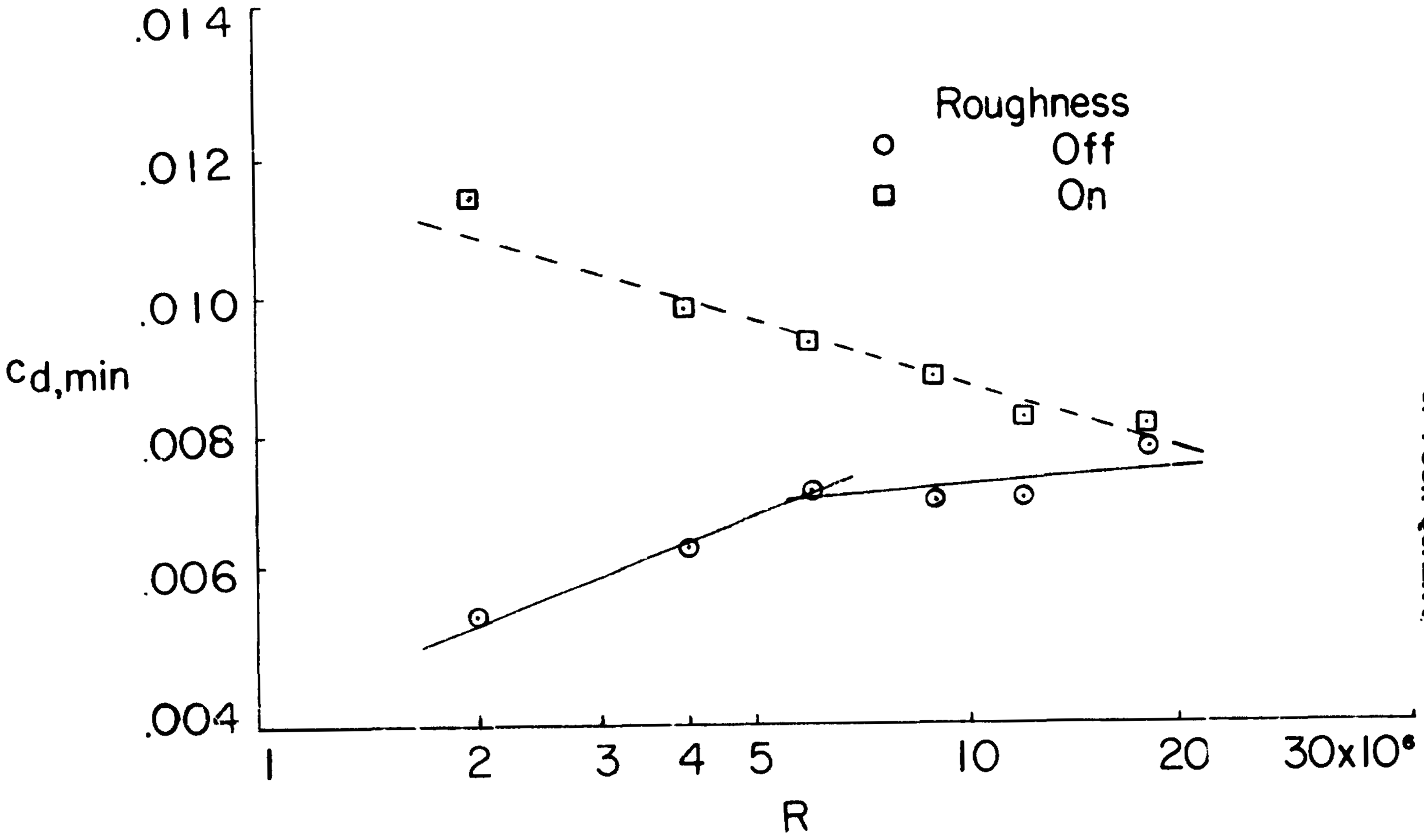

Figure 14.- Variation of minimum drag coefficient with Reynolds number; M = 0.15.

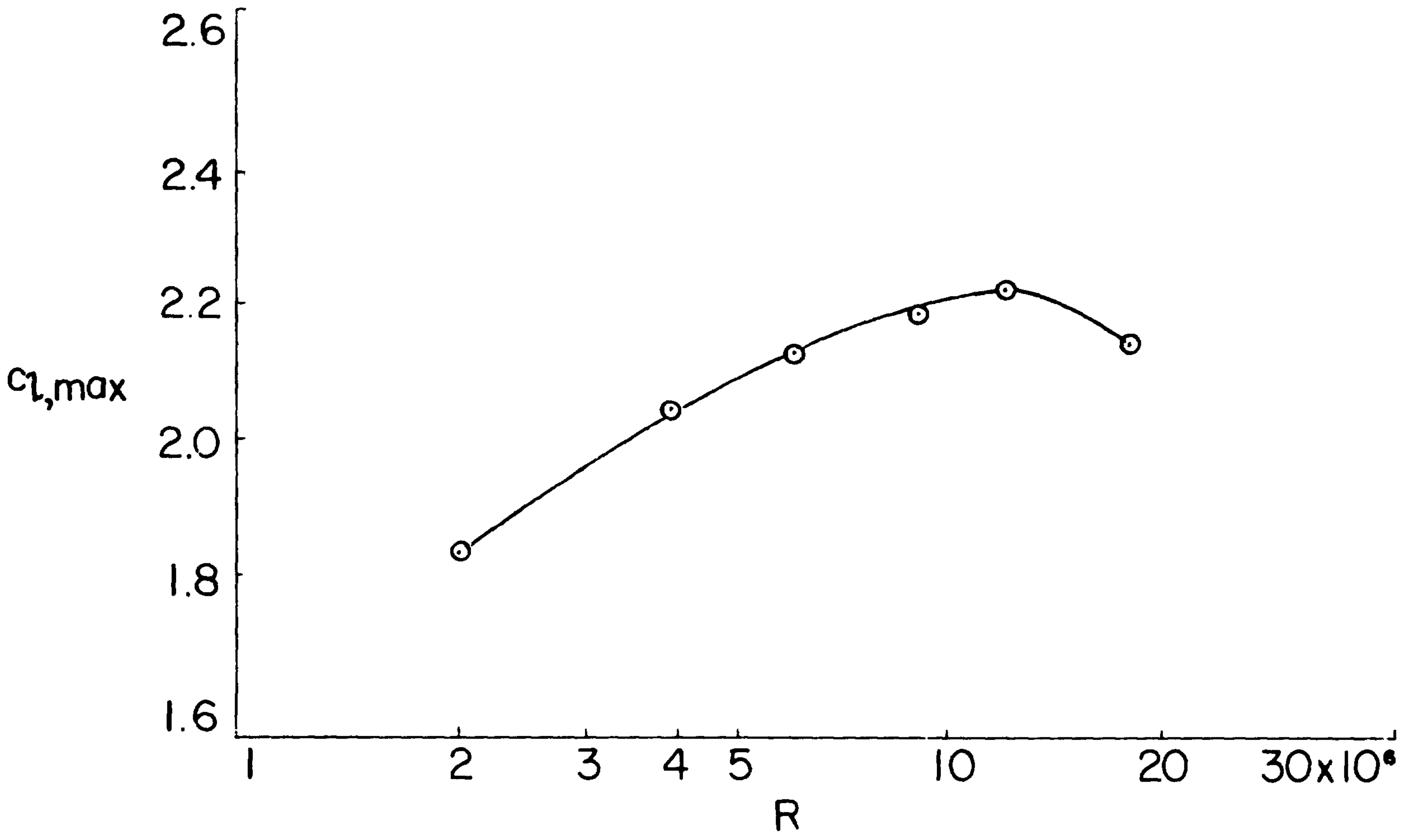

Figure 15.- Variation of maximum lift coefficient with Reynolds number; M = 0.15, transition fixed.

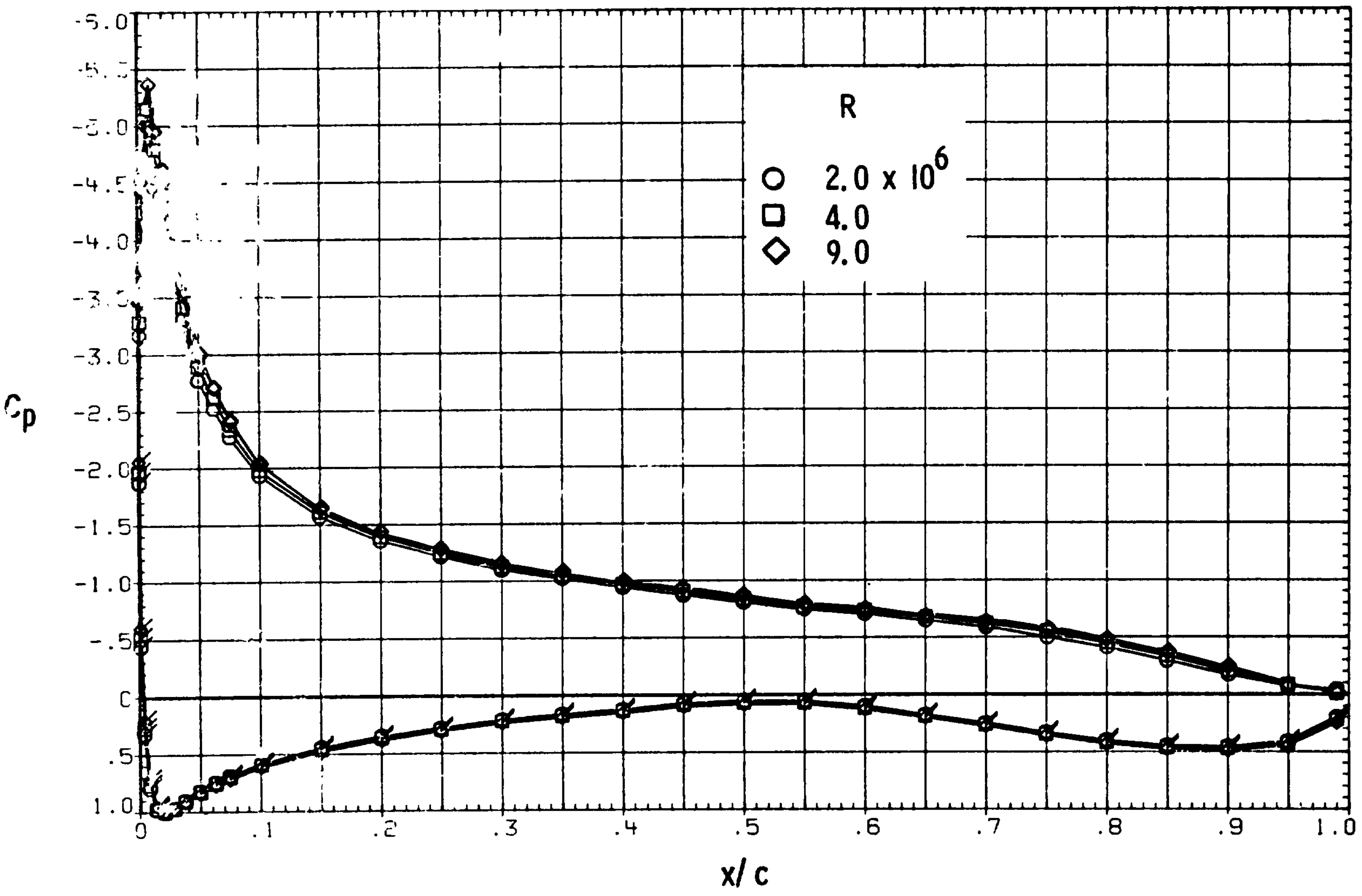

Figure 16.- Effect of Reynolds number on chordwise pressure distribution; M = 0.15, α = 8°, transition fixed. (Flagged symbols indicate lower surface.)

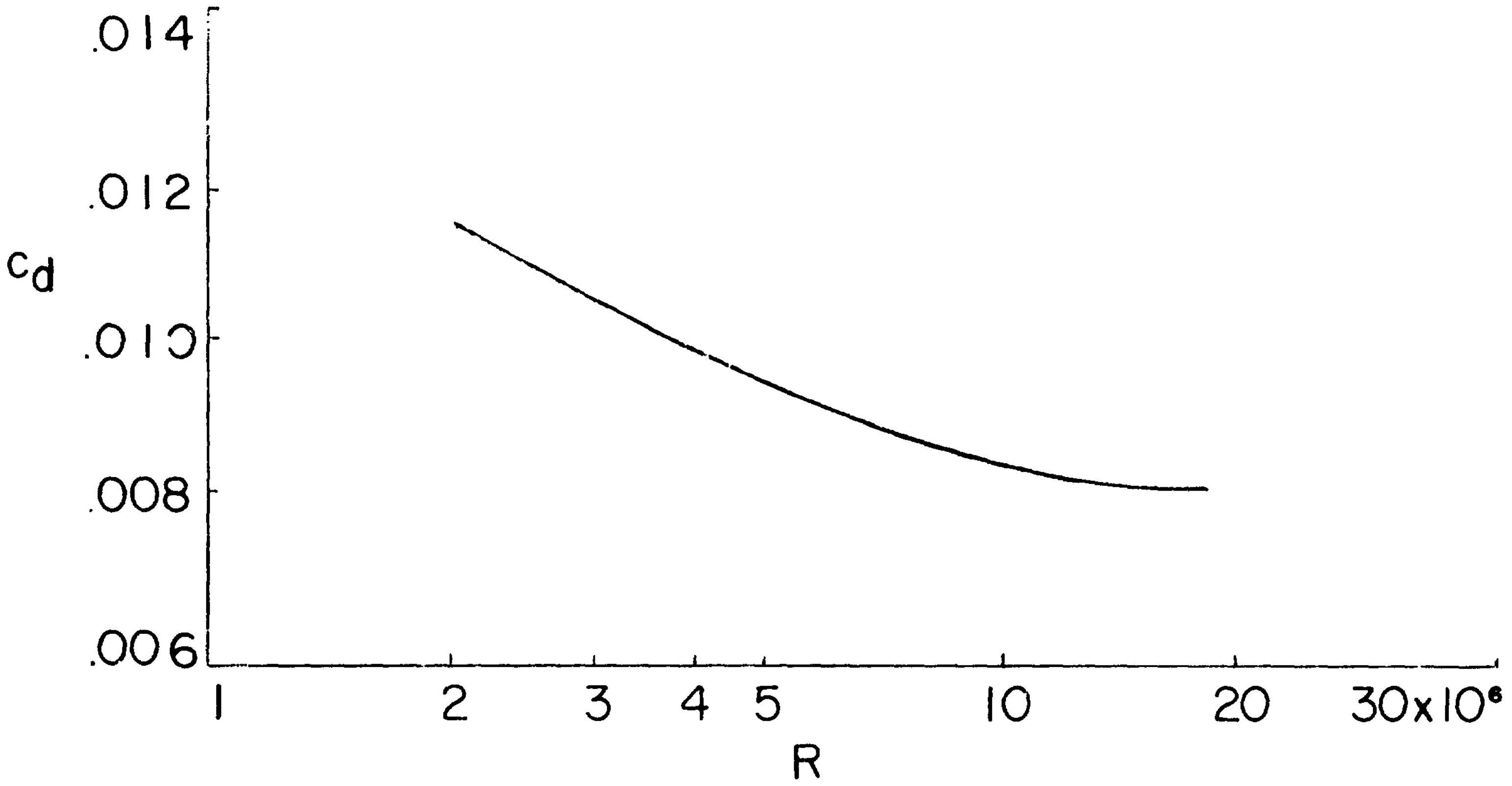

Figure 17.- Variation of section drag coefficient with Reynolds number; $M = 0.15$, $c_l = 0.0$ and 0.7, transition fixed.

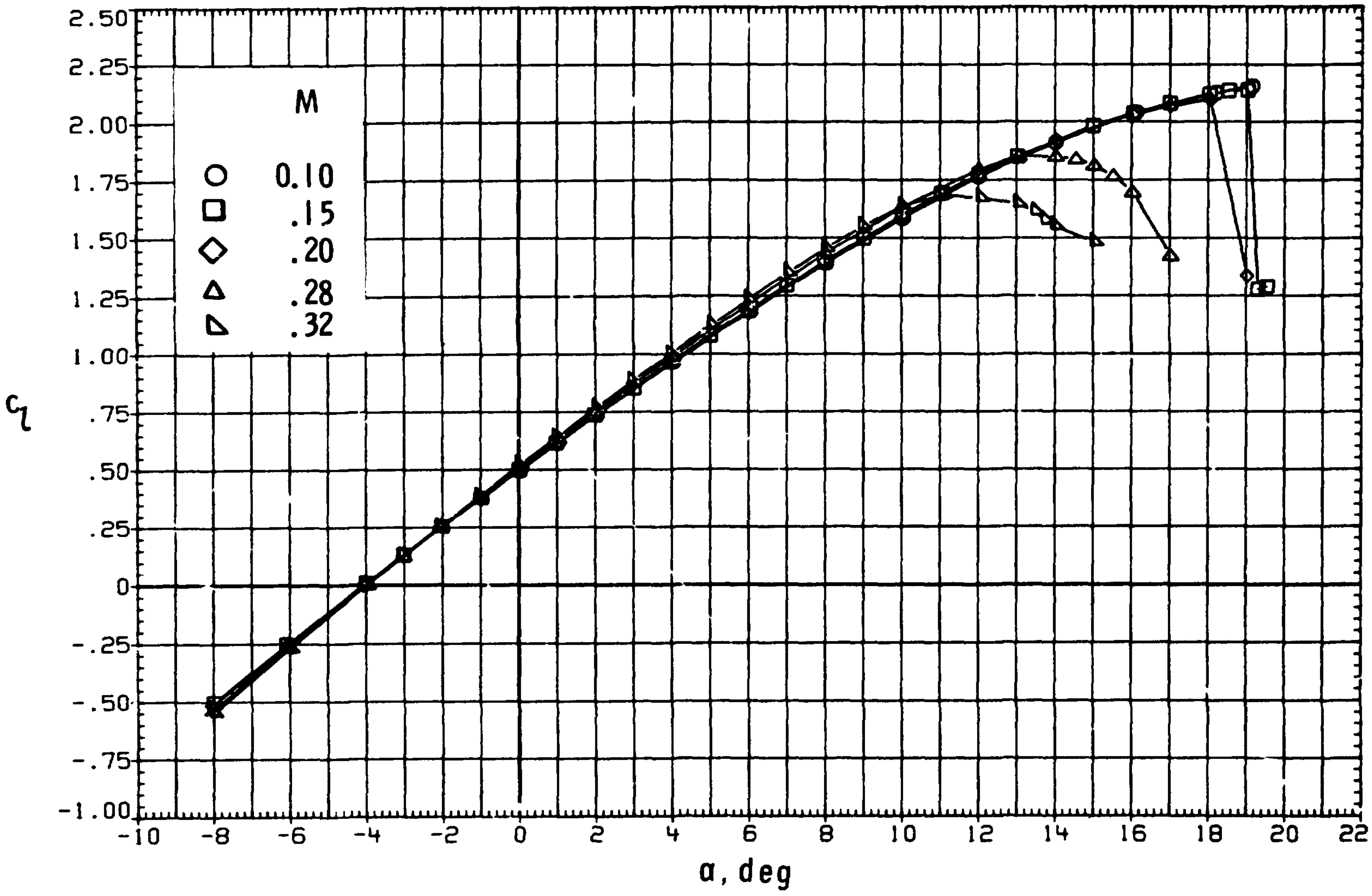

Figure 18.- Effect of Mach number on section characteristics; $R = 6.0 \times 10^6$, transition fixed.

ORIGINAL PAGE IS
OF POOR QUALITY

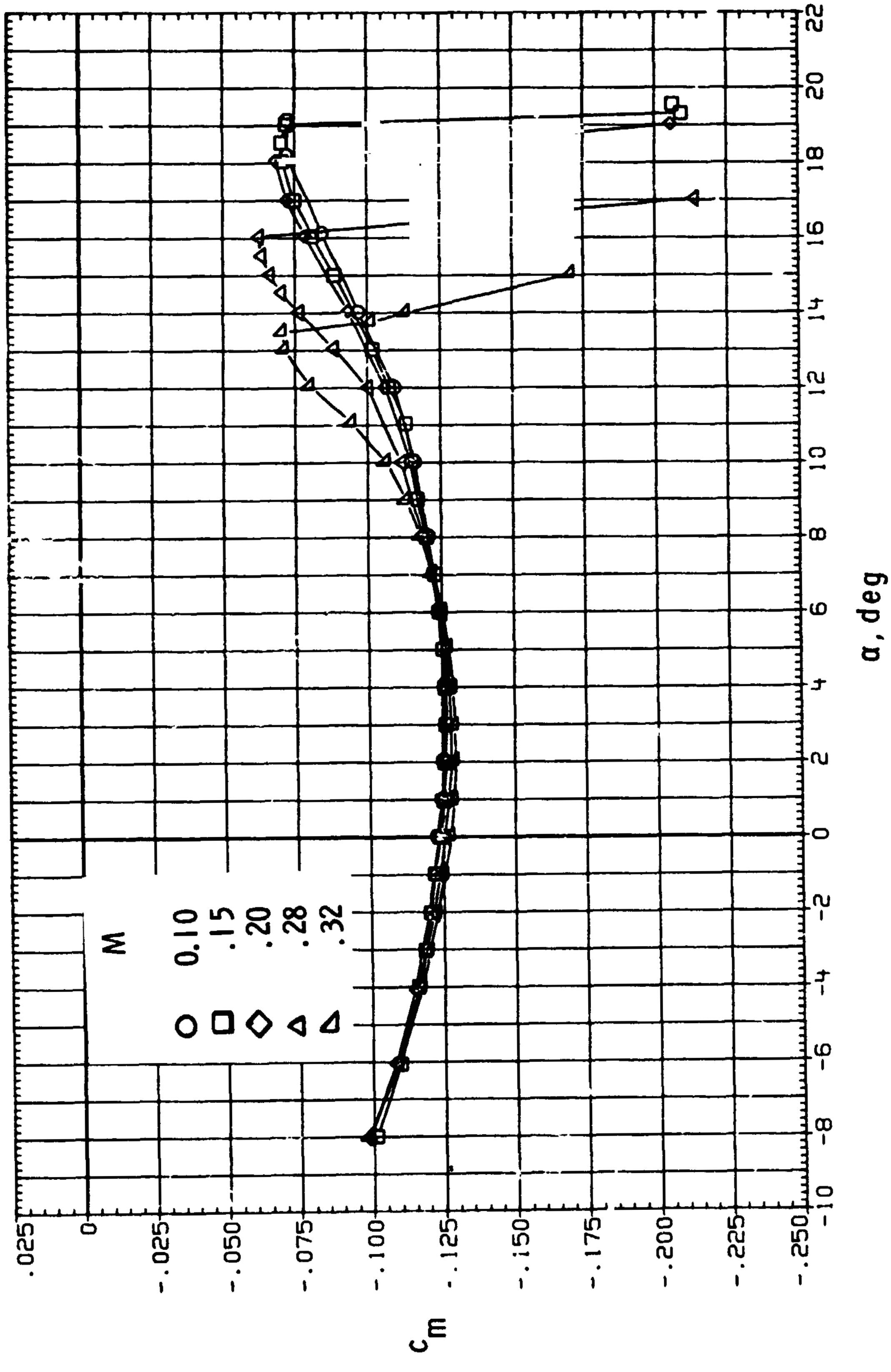

Figure 18.- Continued.

ORIGINAL PAGE IS
OF POOR QUALITY

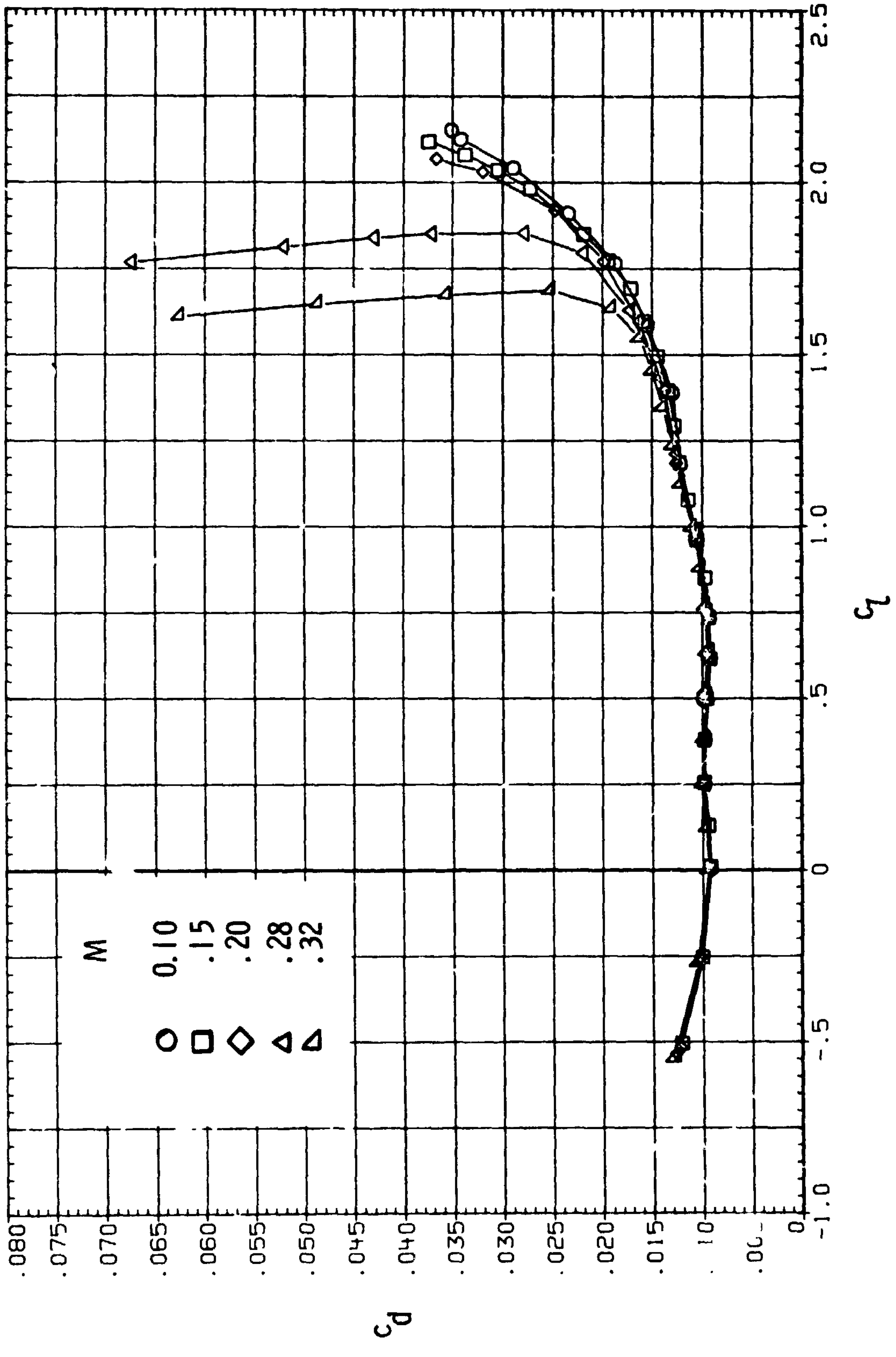

Figure 18.- Continued.

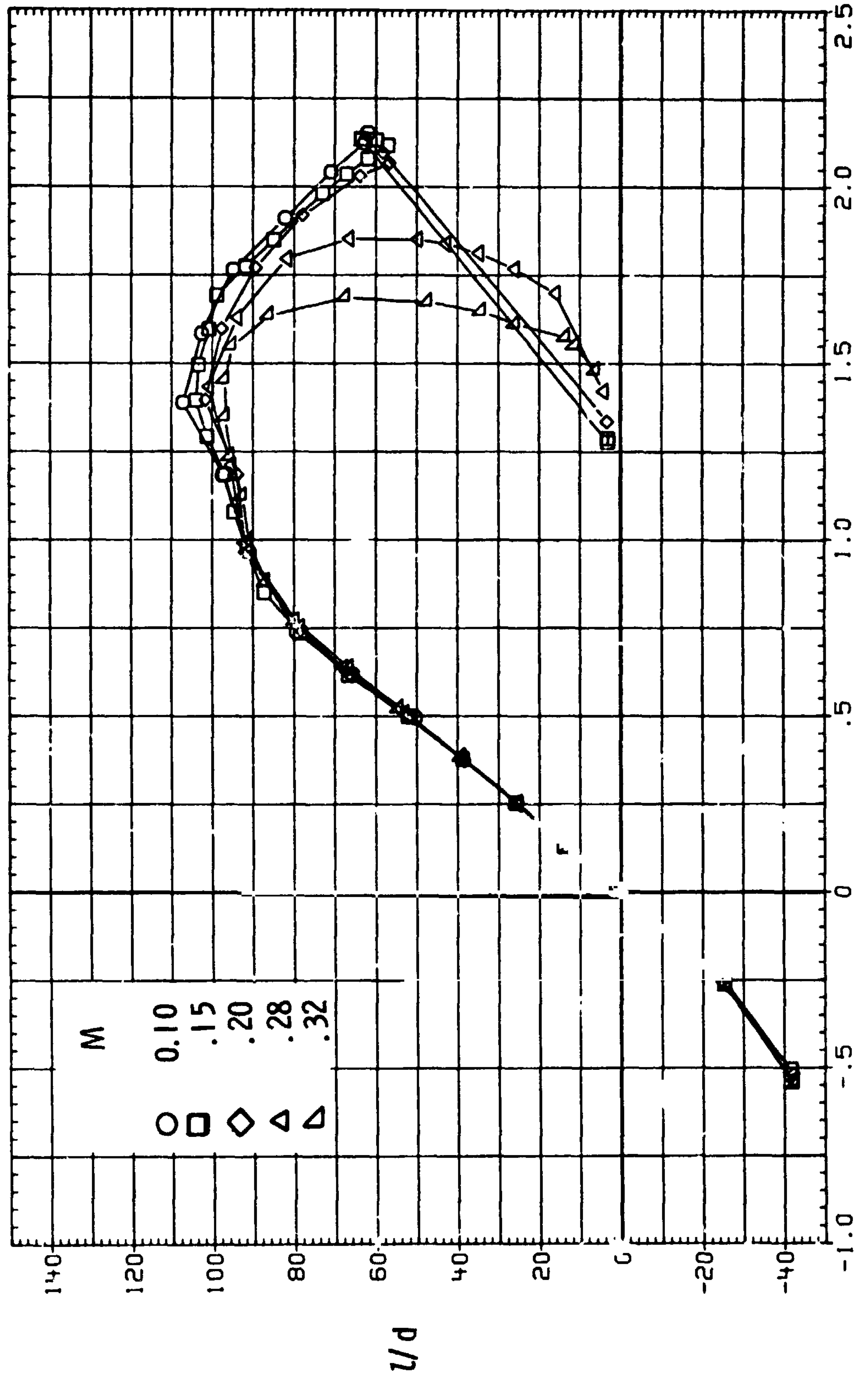

Figure 18.- Concluded.

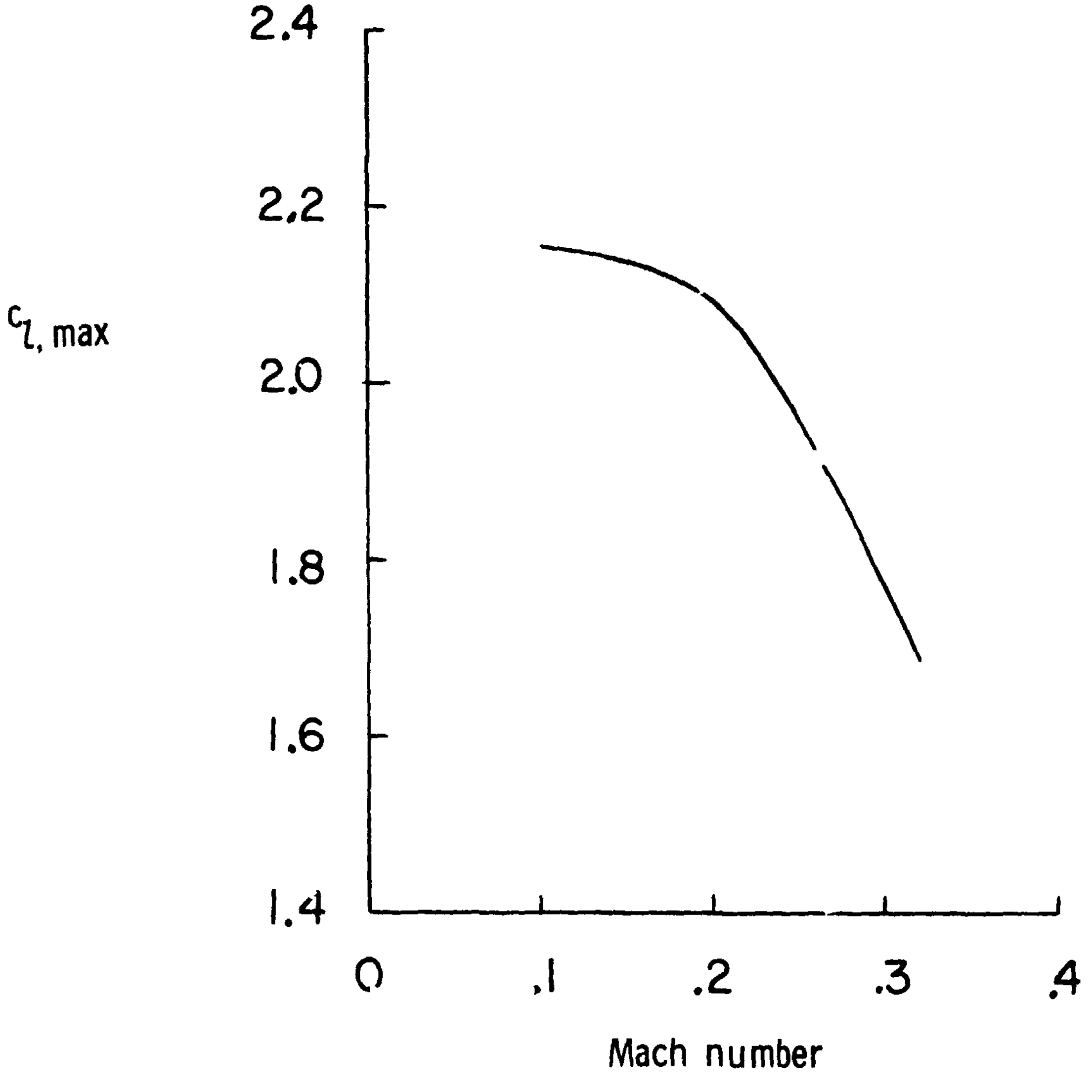

Figure 19.-- Variation of maximum lift coefficient with Mach number; $R = 6.0 \times 10^6$, transition fixed.

ORIGINAL PAGE IS
OF POOR QUALITY

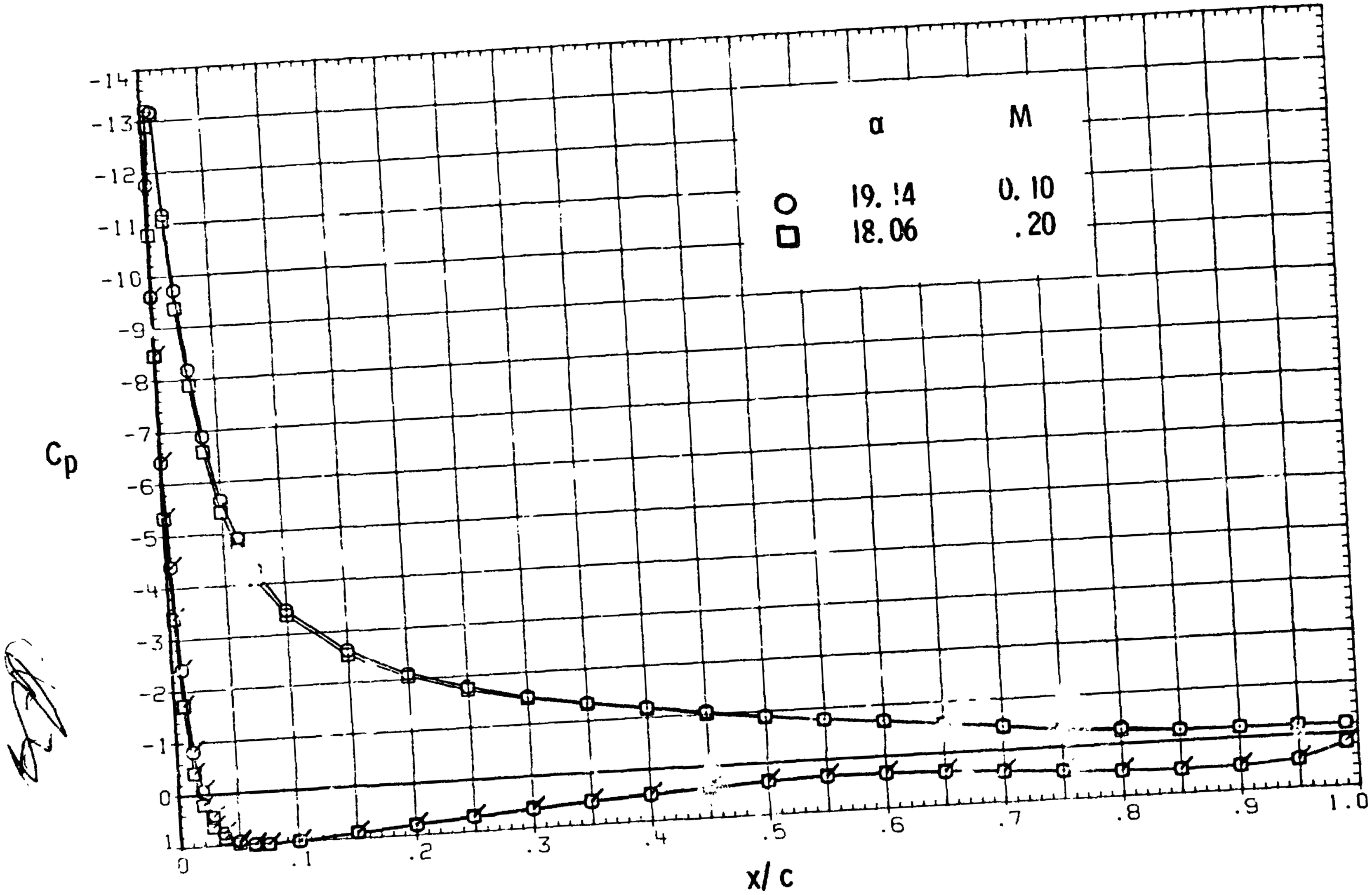

Figure 20.- Chordwise pressure distributions for angles of attack near maximum lift; $R = 6.0 \times 10^6$ transition fixed. (Flagged symbols indicate lower surface.)

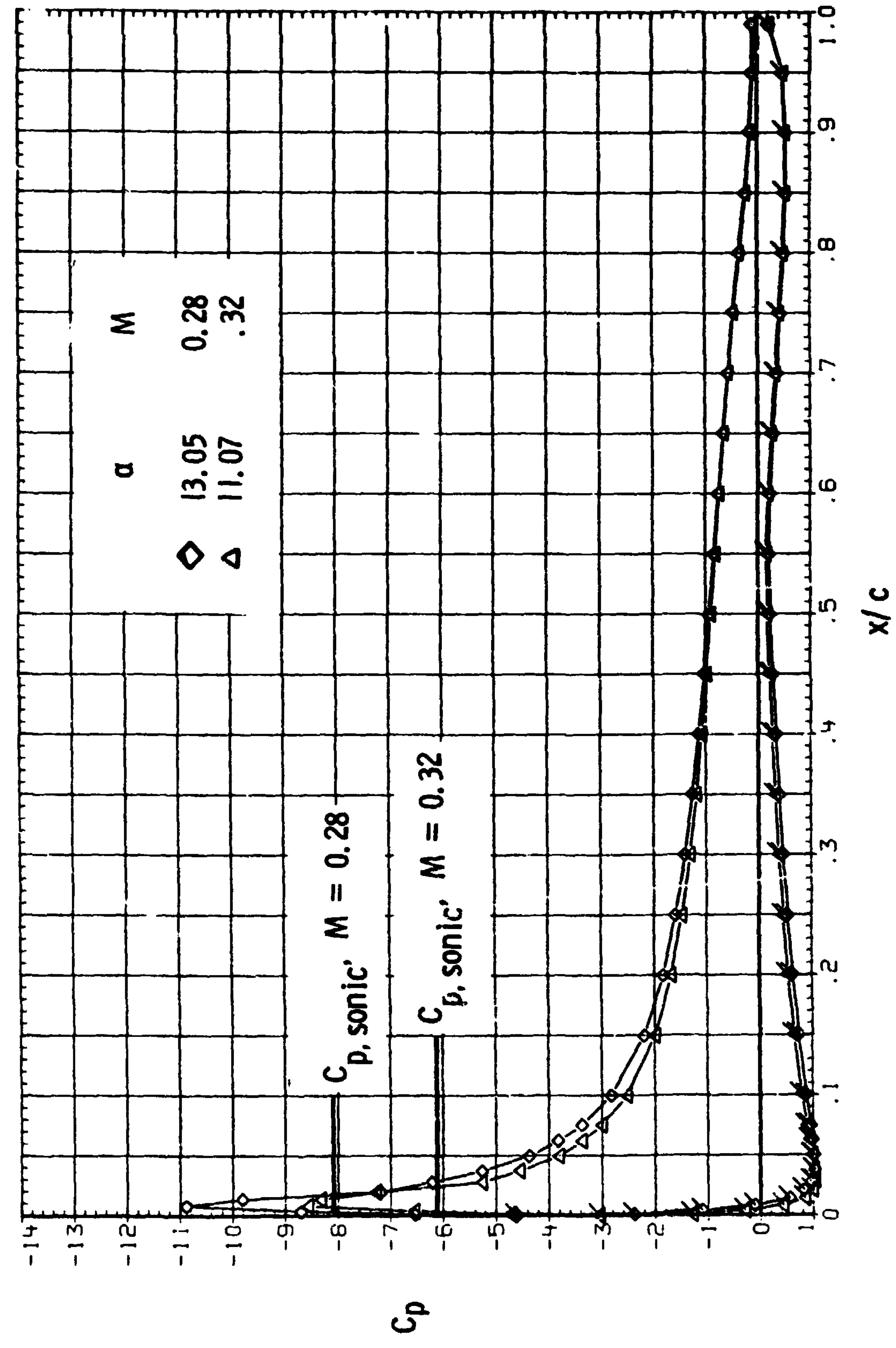

Figure 20.- Concluded.

C-2

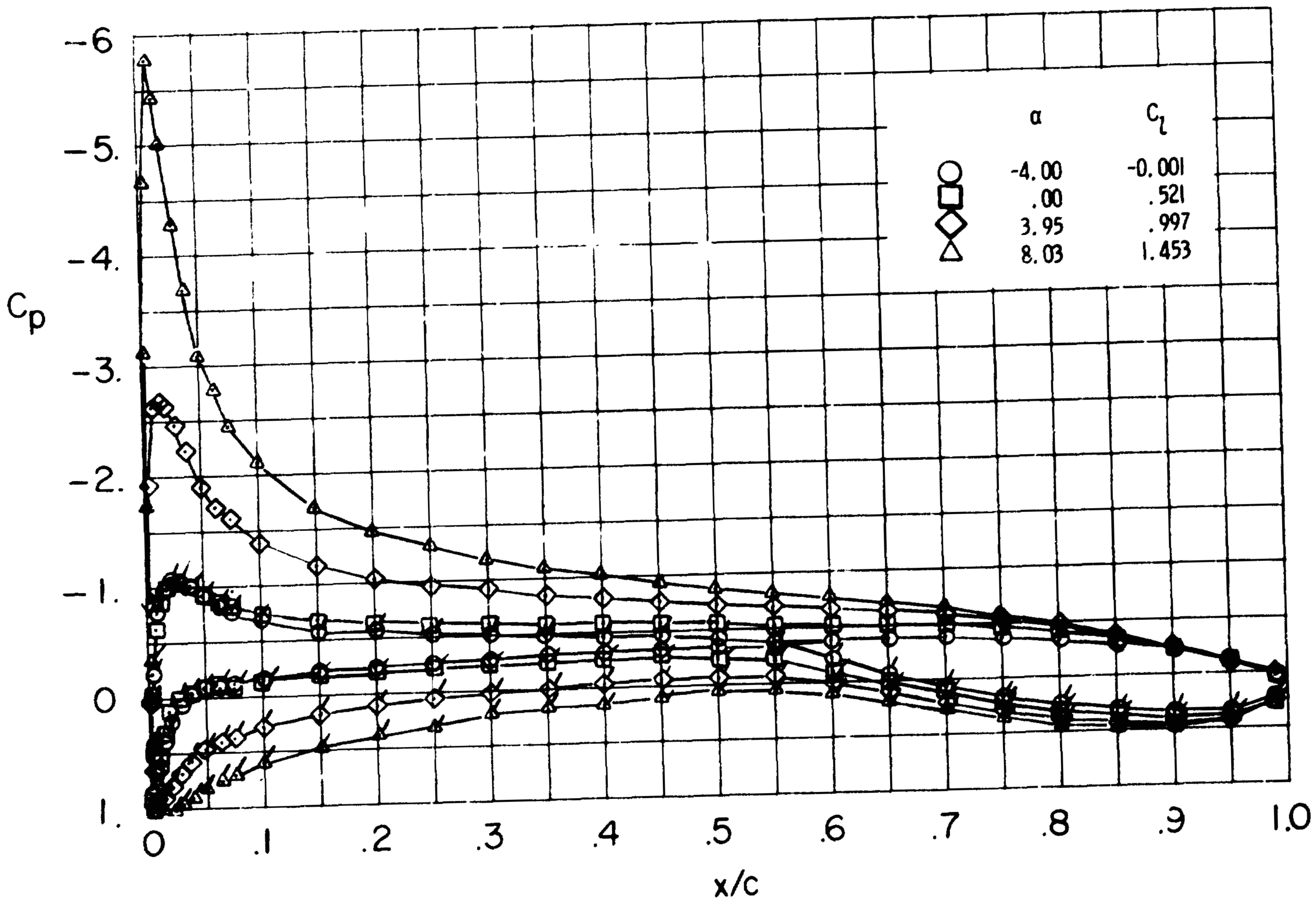

Figure 21.- Effect of angle of attack on chordwise pressure distribution; $M = 0.32$, $R = 6.0 \times 10^6$, transition fixed. (Flagged symbols indicate lower surface.)

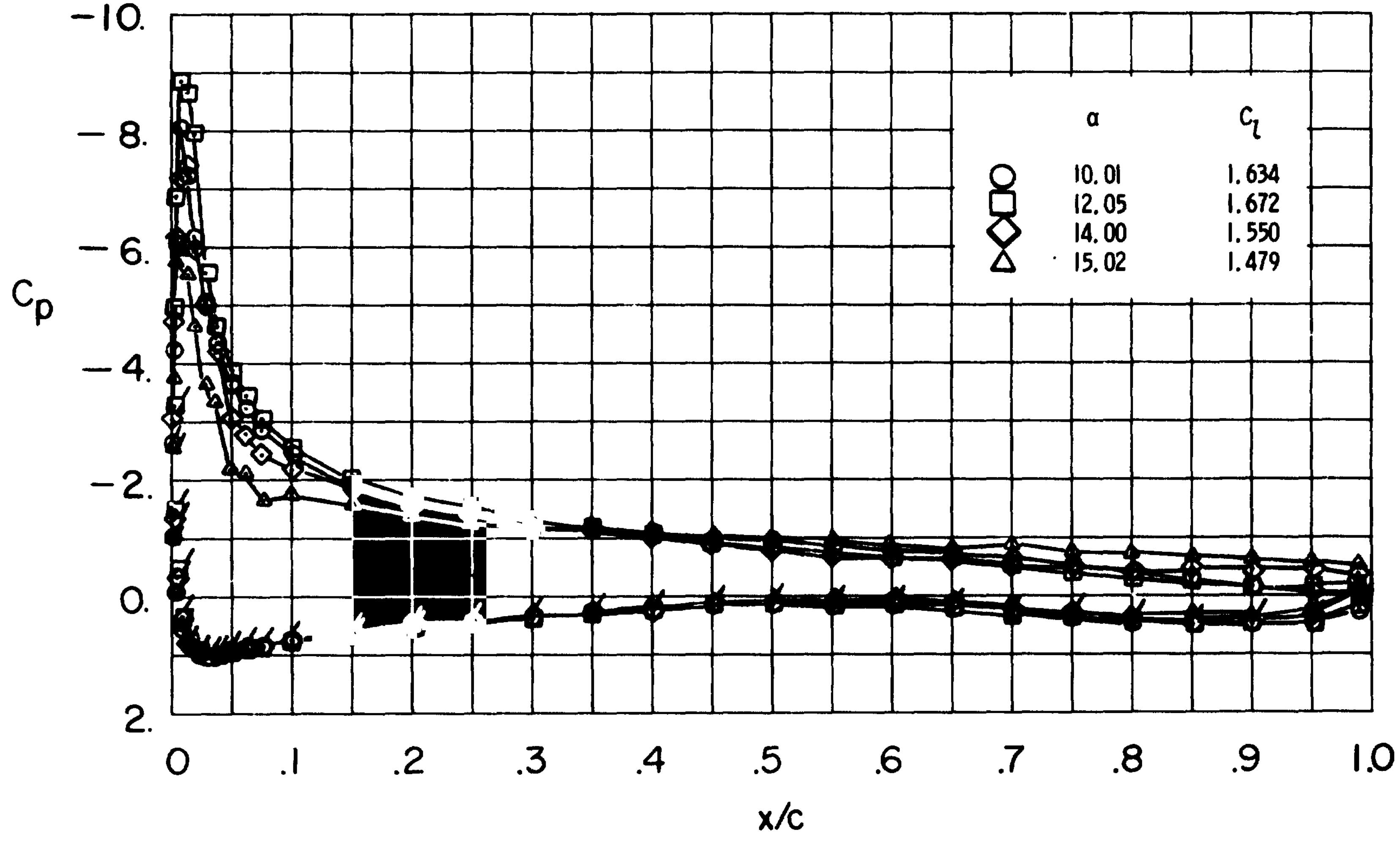

Figure 21.- Concluded.

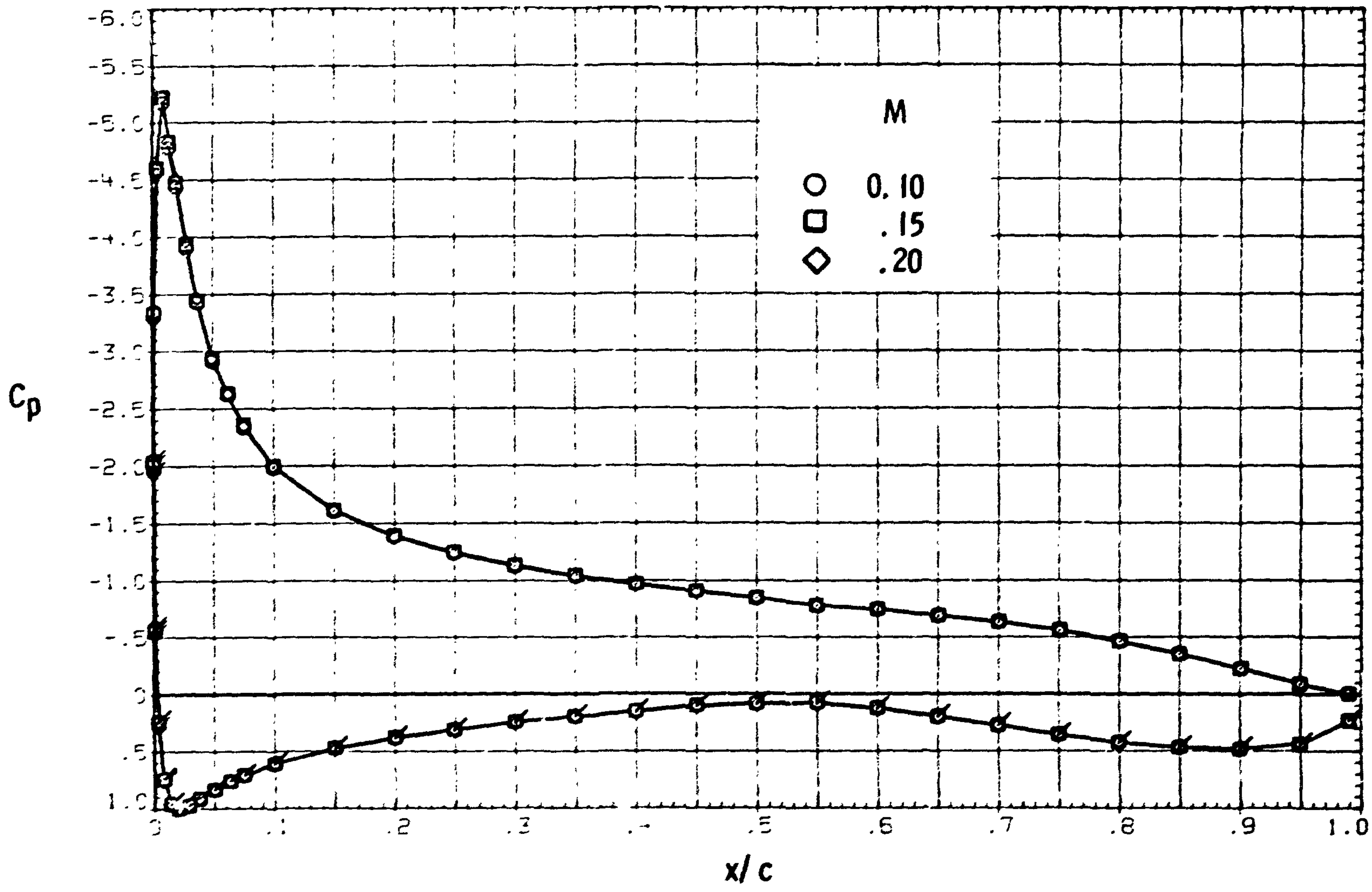

Figure 22.- Effect of Mach number on chordwise pressure distribution; R = 6.0×10^6, α = 8°, transition fixed. (Flagged symbols indicate lower surface.)

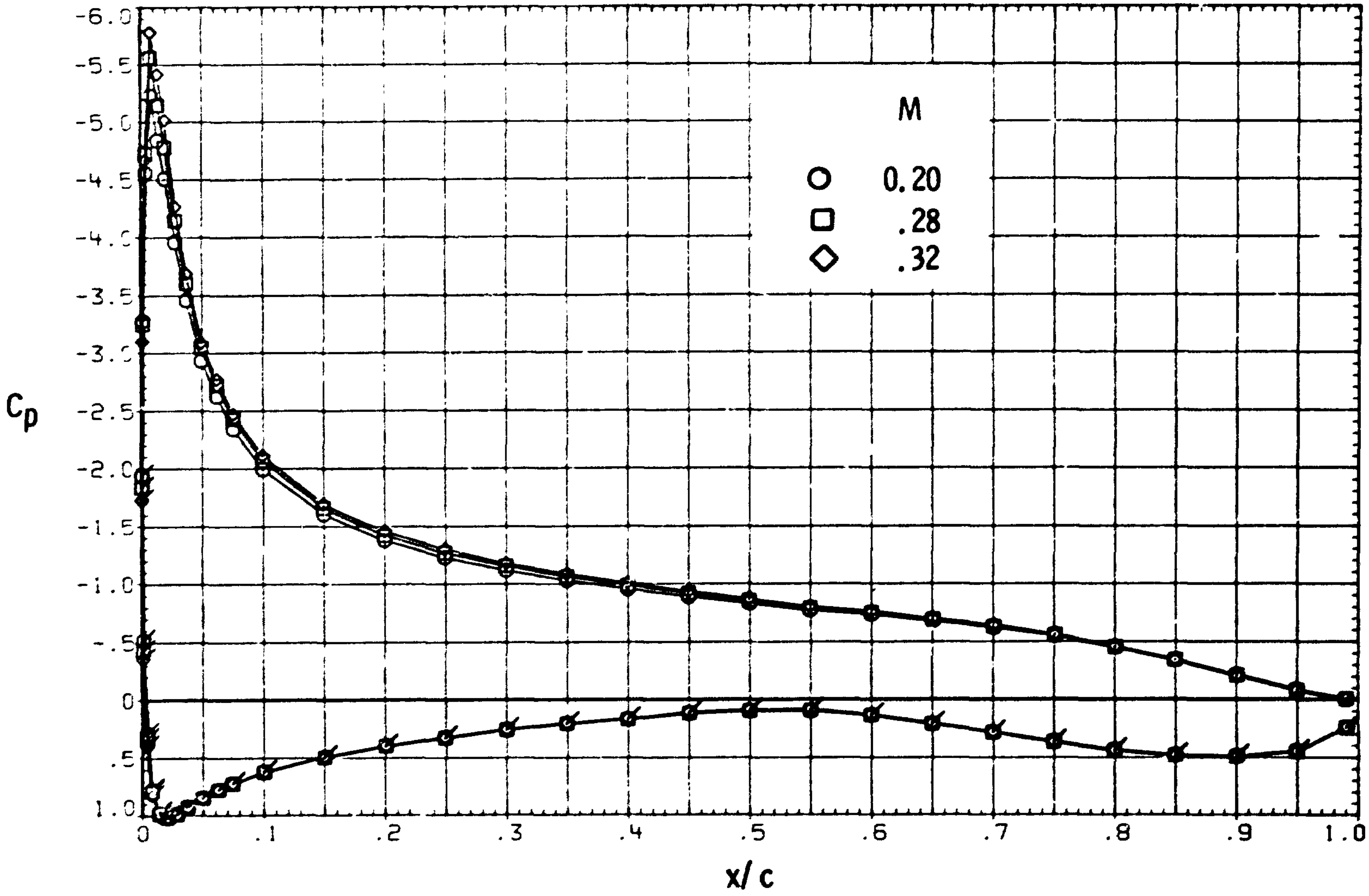

Figure 22.- Concluded.